Rheological Behavior of Dense Thermoresponsive Microgel Suspensions and Lyotropic Liquid Crystals

by

Saisavadas M V

Registration Number: 17PHPH24

A thesis submitted in partial fulfilment for the degree of

Doctor of Philosophy

in

Physics

Under the supervision of

Prof. B. V. R. Tata

&

Prof. Surajit Dhara (co-supervisor)





School of Physics, University of Hyderabad Hyderabad - 500046, India November, 2023

To The Soft matter Community

Declaration

I, Saisavadas M. V, hereby declare that this thesis entitled "Rheological Behavior of

Dense Thermo-responsive Microgel Suspensions and Lyotropic Liquid Crystals"

submitted by me under the supervision of Prof. B. V. R. Tata, Prof. Surajit Dhara (co-

supervisor), School of Physics, University of Hyderabad, Hyderabad is a bonafied

research work and also free from plagiarism. The work is original and has not been

submitted earlier as a whole or in part for the award of any degree/diploma to this

University or any other University / Institution.

Saisavadas. M. V

Reg. No. 17PHPH24

Date: 02/11/2023

Place: Hyderabad

Certificate





This is to certify that the thesis entitled "Rheological Behavior of Dense Thermo-responsive Microgel Suspensions and Lyotropic Liquid Crystals" bearing Reg. No. 17PHPH24, in fulfilment of the requirements for the award of Doctor of Philosophy in Physics is a bonafide work carried out by Saisavadas M. V under our supervision and guidance.

This thesis is free from plagiarism and has not been submitted earlier in part or in whole to this University or any other University/Institution for the award of any degree/diploma. Further, the student has the following publications before the submission of the thesis for adjudication.

- M. V. Saisavadas, S. Dhara, R. G. Joshi, and B. V. R. Tata, Colloid and Polym Sci., 301(6), 599 (2023).
- 2. M. V. Saisavadas, R. G. Joshi, M. P. Kumar, S. Dhara, and B. V. R. Tata, *AIP Conference Proceedings*, **2269**, 060001 (2020).
- 3. M.V. Saisavadas, M. P. Kumar, B.V.R. Tata and Surajit Dhara, "Shear-induced flow and dynamics of the nematic phase of Sunset Yellow lyotropic chromonic liquid crystal" (Submitted to J. Liquid crystal)

Further, the student has passed the following course towards the fulfilment of course work required for Ph.D.

SN	Course Code	Title of the Course	Credits	Pass/Fail
1	PY801	Research Methodology	4	Pass
2	PY802	Advanced Quantum Mechanics	4	Pass
3	PY803	Advanced Experimental Techniques	4	Pass
4	PY804	Advanced Condensed Matter Physics	4	Pass

Prof. B. V. R. Tata

Supervisor

School of Physics

University of Hyderabad

Hyderabad, 500046

Dr. B.V.R. TATA Professor

School of Physics, University of Hydersbad, Gachibowli, Hydersbad-500 046, INDIA

Prof. Surajit Dhara

co-supervisor

School of Physics

University of Hyderabad

Hyderabad, 500046 Dr. Surajit Dhara

Professor School of Physics University of Hyderabad Hyderabad-500 046, INDIA.

Dean

School of Physics

University of Hyderabad

Hyderabad, 500046

DE#N

School of Physics **University** of Hyderabad HYDERABAD - 500 046.

Acknowledgements

I deem it a proud privilege and pleasure in expressing my sincere gratitude to my thesis advisor, **Prof. B. V. R. Tata**, School of Physics, University of Hyderabad, for his valuable guidance, support, encouragement and independence given to me during my research. He was always passionate and enthusiastic about his research projects, was very open to new ideas and showed me how exciting research can be. He has always been extremely generous with his time, knowledge and I was inspired by his dedication to science. His careful planning coupled with a strong sense of duty, strictness and warmth of love had enabled me in the successful completion of this thesis.

I am deeply grateful to **Prof. Surajit Dhara**, Professor at the School of Physics, University of Hyderabad, my thesis co-supervisor, and a member of the Doctoral Committee, for his valuable guidance, support, and concern during my Ph.D. His insistence on excellence, discipline, and sincerity always influenced me towards new research ideas. His care, motivation, and kindness will be remembered forever.

I would like to thank Prof. Sharath Anantha Murthy, who has been there as my Doctoral Committee member, for his discussions and suggestions throughout my research work. I am also thankful to the collaborators Dr. R. G. Joshi, Scientific officer (F), Materials Science Group, Indira Gandhi Centre for Atomic Research (IGCAR), Kalpakkam, for his help in 3D-DLS measurements and Dr. M. Praveen Kumar, School of Physics, University of Hyderabad for his help in rheology measurements.

Further, I am grateful to the present Dean, School of Physics, Prof. K.C. James Raju and former Deans, Prof. Ashok Chatterjee, Prof. V. Seshu Bai and Prof. Bindu A. Bambah, for providing me with all the school level facilities.

I also thank all other faculties and the non-teaching staff of the School of Physics for their cooperation.

I am very much thankful to Mrs. P. V. Rajamani for her meticulous proofreading, which greatly improved the thesis. Also, I would like to express my sincere gratitude to Dr. G. Ravikumar, Distinguished Professor, GITAM University, Visakhapatnam, for his invaluable assistance in ensuring the clarity and correctness of the language used in this thesis.

I would like to extend my sincere gratitude to Light Scattering Studies Section, CMPD, IGCAR, Kalpakkam for their generous provision of access to the 3D light scattering setup used in this research.

I thank University of Hyderabad for the financial assistance during my Ph.D. course also I acknowledge the Science and Engineering Research Board (SERB), Core Grant Project (CRG) of the Department of Science and Technology (DST), India for funding my research work.

I would like to express my heartfelt gratitude to my fellow lab mates Ms. Saranya Narayanan and Mr. Vintha Sivaram. Their camaraderie, unwavering support, and collaborative spirit have been invaluable throughout the course of this research. I am fortunate to have had the opportunity to work alongside such talented individuals. Their friendship and encouragement have made this journey not only academically rewarding but also personally fulfilling.

I am deeply grateful to my friends Aiswrya, Andrews, Ivr, Ponnan, Haritha, Kidav, M. Kattapana, Akshaya, Nikhil, Resmi, Arun, Poly, Vishnu, Charutha, S. Nanda, Justrus, A. Shaji, Arya, A. Raman, Aneesh, Silpa, Anagha and Paul who have been a constant source of encouragement and understanding throughout the journey of completing this thesis. Their unwavering support, even during the most challenging times, has been a source of strength. I appreciate the laughter, camaraderie, and shared experiences that have enriched my life beyond the confines of academia.

I thank my college friends Hari Prasad, Aneesh, Sangeetha, Bibin John, Nishil, Sibeesh, Fahad, Vijesh Pattambi, Atheena and Abin for their friendship.

I am grateful to my teachers, Dr. K. V. Devadasan, C.V. Sandya for their inspiration and support.

I owe my gratitude to my mother Mrs. Shylaja T.V and father Mr. Saseendran M.V whose innumerable sacrifice, unconditional love and confidence has driven me this far. I thank my brothers Mr. Sarathkumar M.V and Mr. Shyamprasad M.V and sisters Arunima M.V and Anjana M.V for their affection and wishes.

Contents

	Page No.
Synopsis	х
List of Figures	хіх
List of Tables	xxv
List of Symbols	xxvi
List of Abbreviations	xxv
Chapter 1: Introduction	
1.1 Colloidal systems	1
1.1.1 Hard Sphere colloids	3
1.1.2 Charge stabilized colloidal suspensions	5
1.1.3 Stimuli-responsive microgel suspensions	7
1.1.4 Poly (N-Isopropylacrylamide) (PNIPAM) microgels	8
a) Thermo-responsive characteristics of PNIPAM microgel particles	8
b) Core-shell morphology of PNIPAM microgel particles	9
c) Phase behavior of PNIPAM microgel suspensions	11
1.1.5 Dynamics of colloidal particles	13
a) Non-interacting colloidal suspensions	14
b) Interacting colloidal suspensions	15
1.1.6 Rheological insights and industrial advancements	16
1.1.7 Yielding behavior of hard sphere colloidal glasses	18
1.1.8 Yielding behavior of attractive colloidal glasses	21
1.2 Liquid crystals	22
1.2.1 Lyotropic chromonic liquid crystals (LCLCs)	23
1.2.2 Sunset Yellow chromonics	25
1.3 Motivation	29
References	

Chapter 2: Synthesis Method and Experimental Techniques

2.1 PNIPAM microgel suspensions	. 40
2.1.1 Synthesis of core-shell PNIPAM microgel particles by batch method	.40
2.1.2 Synthesis of homogeneous core PNIPAM microgel particles by semi-batch methods.	
2.1.3 Purification of PNIPAM microgel suspensions	. 44
2.1.4 Preparation of dense PNIPAM microgel samples	. 45
2.2 Sunset yellow (SSY) liquid crystals	.46
2.2.1 Purification of SSY powder.	.46
2.2.2 Preparation of Sunset Yellow liquid crystal (SSY LC) samples	.47
2.3. Experimental methods	.48
2.3.1 Light scattering technique	.48
a) Auto correlation based dynamic light scattering (DLS)	. 48
b) Cross-correlation based 3D dynamic light scattering (3D-DLS)	. 54
c) Non-ergodic analysis	. 57
2.3.2 UV-visible - NIR spectroscopy	. 58
2.3.3 Rheology	. 60
a) Fundamentals of Rheology	
b) The Maxwell model	. 62
c) Rheometer and measuring systems	. 64
i) Cone and Plate measuring system	. 66
ii) Parallel plate measuring system	. 67
d) Rheo-Microscopy	. 68
e) Rheological measurements	. 69
i) Small Amplitude Oscillatory Shear (SAOS)	. 70
ii) Large Amplitude Oscillatory Shear (LAOS)	.72
iii) Rotational measurements	.73
2.3.4 Polarizing Optical Microscopy (POM)	.75
References	

Chapter 3: Yielding Behavior of Dense PNIPAM Microgel Colloidal Glasses	
3.1 Introduction	79
3.2 Experimental Details	82
3.2.1 3D Dynamic Light Scattering (3D-DLS) measurements	83
3.2.2 Linear Rheology and Large Amplitude Oscillatory Shear (LAOS) me	asurements . 84
3.3 Results and Discussions	87
3.3.1 Characterization of glassy state	87
3.3.2 Dynamical Strain sweep studies on dense PNIPAM microgel glasse transition	
3.3.3 LAOS behavior and Lissajous curves	95
3.3.3 Energy of yielding and dissipation	99
3.3 Summary	100
References	
Chapter 4: Shear-induced Flow Behavior of Lyotropic Chromonic Liquid Crys	stals
4.1 Introduction	104
4.2 Experimental Details	106
4.3 Results and Discussions	108
4.3.1 Flow curves	108
4.3.2 Rheo-microscopy: Defect structure	111
4.3.3 Stress oscillations	113
4.4 Summary	115
References	
Chapter 5: Summary and Future Work	
5.1 Summary and conclusions	118
5.2 Key findings of the thesis	121
5.3 Scope for the future work	123

Synopsis

Rheology is a multidisciplinary field where the flow and deformation of materials are investigated. The deformations in the case of Hookean solids (ideal elastic solids) and Newtonian liquids (ideal viscous liquids) can be explained by the classical limits of Hooke's law and Newton's law, respectively. However, there are many soft matter systems (foods, bio-fluids, colloidal suspensions, liquid crystals, etc.) whose deformation under external shear can be complex and cannot be explained by simple Hooke's law or Newton's law. The rheological properties of these soft matter systems have fundamental and practical relevance. We studied the flow and deformation of two such complex viscoelastic systems: i) aqueous suspensions of poly(N-isopropylacrylamide) (PNIPAM) microgels and ii) lyotropic liquid crystals of Sunset Yellow (SSY) formed in aqueous medium.

PNIPAM microgels are hydrogel particles that are highly responsive to external stimuli like temperature, pH, electric field, stress field, etc. Upon variation of these external stimuli, the size and the interparticle interaction U(r) among the microgel particles can be tuned. As these particles are thermo-responsive, they exhibit a decrease in size with an increase in temperature and show volume phase transition (VPT) by undergoing a sudden transition from swollen to collapsed state at $\sim 33^{\circ}$ C. PNIPAM microgel spheres in an aqueous medium can readily be synthesized by free-radical precipitation polymerization. In general, the internal structure of the PNIPAM microgel particle is heterogeneous. It consists of a highly cross-linked core (high polymer density) and a loosely cross-linked shell (20-30 nm) (low polymer density) decorated with dangling polymer chains. However, PNIPAM microgel spheres having only homogenous core without any dangling polymer chains can be synthesized by altering the synthesis conditions. Under favourable conditions, monodisperse PNIPAM

microgel spheres dispersed in water show gas-like, liquid-like, crystal-like and even glass-like structural ordering similar to that of atomic systems. Hence, they are widely considered as ideal model condensed matter systems.

Many research works were reported on various aspects of PNIPAM microgels in dilute conditions. Recently, a few works were reported on the sub-diffusive dynamics and yielding behavior of dense (volume fraction, $\phi > 0.58$) PNIPAM microgels under external shear. However, a proper explanation of the role of entanglements of dangling polymer chains between the nearest neighbor particles in the dense state during the yielding process is not properly addressed.

One of the objectives of this thesis is to elucidate the role of dangling polymer chains in the yielding behavior of dense PNIPAM suspensions in their colloidal glassy state, $\phi > 0.58$). Two-step yielding has been observed in colloidal glasses with attractive interactions but not in systems with repulsive interactions, such as hard-sphere glasses and glasses of like-charged colloids. Being a repulsive system below VPT, dense PNIPAM microgel suspensions exhibit two-step yielding when subjected to Large Amplitude Oscillatory Shear (LAOS). This observation is unique to dense PNIPAM microgel suspensions. Here, we report the unusual two-step yielding and the role of entanglements in the yielding behavior of dense PNIPAM microgel suspensions when subjected to LAOS. These studies have been carried out by performing rheological experiments as well as dynamic light scattering (DLS) measurements.

Free radical precipitation polymerization has been performed with different synthesis techniques in order to obtain PNIPAM microgel spheres with two different morphologies (i) having core—shell structure (CS-PNIPAM) with dangling polymer chains (ii) having only a homogeneous cross-linked core (HC-PNIPAM). Dynamic light scattering (DLS) technique has been employed to determine the PNIPAM microgel particle size in the dilute condition and to investigate the short time particle dynamics in the dense condition. UV-Vis

spectroscopy has been used to determine the Bragg peak and hence the number density of the crystallized CS-PNIPAM microgel suspension when kept undisturbed for 24 hours. Further, both types of dense PNIPAM microgel suspensions were subjected to rheological studies to characterize their deformation behavior. Non-linear characteristics of the samples were investigated using LAOS measurements.

PNIPAM particles are spherical in shape and the colloidal suspension of these particles under dense conditions exhibit isotropic phases that are analogous to atomic systems. Whereas, Liquid crystals (LCs) have their physical properties intermediate to that of ordered solids like crystals and isotropic liquids. When in liquid crystalline state, the molecules exhibit long-range orientational order and a few of them can also show positional order. As a result, the LC phase exhibits the symmetry that exists between liquids and crystals. There are two primary classifications of liquid crystals, namely thermotropic and lyotropic. In thermotropic LCs, mesophases form as a result of temperature, but in lyotropic LCs, mesophases form as a result of both temperature and solute concentration. There are special types of lyotropic liquid crystals called lyotropic chromonic liquid crystals (LCLCs), where mesophases are formed when compounds such as dye or drug are mixed in suitable solvent, preferably water.

There exists a good amount of literature on thermotropic LCs reporting the flow and deformation behavior under applied stress whereas, the rheology of LCLCs is relatively less studied. In order to investigate the rheological properties and correlation to microstructures, we have chosen a very common chromonic LC, Sunset Yellow (SSY). The chromonic molecules of SSY are rigid disc-shaped, having hydrophobic aromatic centers and ionic or hydroxyl groups at the periphery. In an aqueous solvent, the hydrophobic centers stack on each other via noncovalent $\pi-\pi$ interactions, forming cylindrical aggregates with a stacking periodicity of approximately 0.34 nm. The diameter of aggregates is about 1 nm.

Being a food dye, the rheological behavior of SSY chromonic LCs (SSY LC) has both industrial and fundamental significance. There are a few rheological studies on SSY LC mostly focusing on the shear rate dependent viscosity. However, shear induced orientation, microstructures and flow behavior of SSY LC are underexplored. Here, we report the rheological properties of the nematic phase of SSY liquid crystal, focusing on shear-induced microstructures and their dynamics.

Towards the studies on SSY LC, SSY dye was dissolved in water in order to obtain the nematic phase. The texture of the sample in the nematic phase was observed using a polarizing optical microscope (POM) and shear-induced microstructures and dynamics of SSY LC in the nematic phase were investigated using a rheometer equipped with the rheo-microscopy module.

The thesis is organized into five chapters. In which, chapter 1 introduces both the PNIPAM microgel suspensions and SSY liquid crystals. Chapter 2 describes sample preparations for both the PNIPAM microgel suspensions and SSY liquid crystal systems and the various experimental techniques used to probe the above mentioned systems. Chapter 3 explains the yielding behavior of dense PNIPAM microgel colloidal glasses and chapter 4 describes the rheological studies on SSY lyotropic chromonic liquid crystal. The conclusions of the above mentioned studies and the scope for future work are provided in chapter 5. The contents of each chapter are summarized as follows.

Chapter 1. Introduction

This chapter gives a brief introduction to colloidal suspensions and liquid crystals. At the beginning of the chapter, colloidal suspensions of hard sphere and stimuli-responsive microgels are discussed in terms of their stability, interparticle interactions, phase behavior, and dynamics under dense conditions. In the later stage of the chapter, various types of liquid crystals and their rheological properties, which are relevant to our studies, are introduced. The

rheology of viscoelastic materials is described. The deformation and flow behavior of hard sphere and soft sphere colloids under linear as well as non-linear shear deformation is addressed. The motivation for the present work along with the experimental studies that have been carried are presented towards the end of the chapter.

Chapter 2. Synthesis Method and Experimental Techniques

Synthesis of CS-PNIPAM and HC-PNIPAM microgel spheres through the free radical precipitation polymerization method is discussed. The procedure for the preparation of dense samples of PNIPAM microgels and liquid crystal samples of SSY are presented. All the details of the instruments, measurement schemes and methods of analysis used to investigate the dynamics, yielding and flow behavior of PNIPAM microgels and SSY LCs are presented. A simple auto correlation based DLS technique was used to determine the microgel particle size in the dilute suspensions whereas three dimensional (3D) dynamic light scattering (3D-DLS) was used to probe the dynamics in the turbid PNIPAM microgel suspension. As the dense CS-PNIPAM sample showed crystalline ordering when kept undisturbed for 24 hours, UV-vis spectroscopy was used to determine the Bragg peak and hence number density. Rheometer was employed to investigate the yielding behavior of dense PNIPAM microgel suspension. Polarizing optical microscopy (POM) was used to determine the nematic phase of SSY LC. The rheo-microscopy module was employed to investigate the flow behavior while simultaneously visualizing the optical images. Different types of measurement schemes relevant to our studies using a rheometer are presented in detail.

Chapter 3. Yielding behavior of dense PNIPAM microgel colloidal glasses

The rheological investigation of colloidal glasses offers deep insight into the glassy relaxation and aging phenomena that are common to glass forming atomic and molecular systems. In general, colloidal glasses are viscoelastic in nature and yield under the application

of external shear. The viscoelasticity of the colloidal glass is typically measured by performing the rheological experiments with the strain applied in an oscillatory fashion at constant frequency, ω and variable amplitude, γ_0 . The stress response of the material is expressed in terms of storage/elastic modulus (G') and loss/viscous modulus (G''). In a typical oscillatory shear measurement, G' and G'' are measured as a function of γ_0 . If the deformation, γ_0 is small, (typically less than 1%) the stress response of the material will be linear with G'and G'' being independent of the applied strain, γ_0 , whereas G' and G'' strongly depend on γ_0 if the deformation is large. When hard sphere colloidal glass is subjected to non-linear rheological experiments, it exhibits a near-plateau in G' and G'' at low γ_0 and undergoes yielding by exhibiting a monotonic decrease in G' and a peak in G'' beyond a critical value of γ_0 (called yield point). The peak in G'' is considered as a signature of many soft glassy materials. Yielding behavior in purely repulsive colloidal glasses of hard spheres or charged colloids has been thoroughly investigated and is understood to be caused by the breaking of cages formed by topological neighbors. This cage breaking mechanism is responsible for the single peak in G'' observed during non-linear strain sweep measurements. However, yielding of attractive glass (where interactions are made attractive by introducing the depletion attraction via the addition of external polymer) occurred in two steps which are identified by two peaks in G'' observed during non-linear strain sweep measurements. Despite interaction potential between the core shell PNIPAM microgel particles being repulsive, the suspension in its glassy state exhibits two-step yielding similar to that of attractive glass. This observation is quite unusual and a proper explanation connecting the microstructure of PNIPAM microgels and its influence on the yielding behavior under a dense state is yet to be reported. This chapter elucidates the yielding behavior of dense PNIPAM microgel colloidal glasses and the role of entanglements between the nearest neighbor particles on the yielding mechanism. This problem is investigated using non-linear rheology by means of Large Amplitude Oscillatory Shear (LAOS). Dense glassy samples of core-shell (CS) PNIPAM and homogeneous core (HC) PNIPAM were prepared with volume fractions $\phi = 0.80, 0.89$ respectively. These dense turbid samples were characterized for their glassy state using DLS and were further verified by rheology. The glass transition temperature of dense PNIPAM microgel glass is identified by determining the damping factor (ratio of G'' to G') as a function of temperature. DLS measurements on CS-PNIPAM indicate the presence of dangling polymer chains, which are absent in HC-PNIPAM particles in dense conditions and are responsible for the observed sub-diffusive behavior in the mean squared displacement at short times. Further, we did LAOS measurements to gain a better understanding of the role of dangling polymer chains and their entanglements on the yielding behavior of the glassy state, where both PNIPAM microgel glass samples were subjected to LAOS and it is observed that, in the case of CS-PNIPAM, G' exhibited a monotonic decrease and G'' showed two peaks similar to that observed in attractive glasses. Meanwhile, G' exhibited a monotonic decrease and G" showed a single peak in the case of HC-PNIPAM. It is argued that in the case of CS-PNIPAM, the two peaks arise i) because of the disentanglement of dangling polymer chains of neighboring particles and ii) due to the breaking of cages of topological neighbors. This difference in the yielding behavior also signifies the presence of entanglements in the CS-PNIPAM glass sample. Moreover, we determined the energy associated with the yielding in the glassy state of both types of microgel particles which is described at the end of the chapter.

Chapter 4. Shear-induced Flow Behavior of Lyotropic Chromonic Liquid Crystals

Lyotropic chromonic liquid crystals (LCLCs) are formed when compounds of drugs or dyes are dispersed in a solvent, mostly in water. The molecules of these compounds are disc-shaped, having a polyaromatic core and ionizable groups at the periphery. In water, these molecules form cylindrical stacks and hence exhibit different mesophases. In recent years, LCLC compounds have experienced significant attention due to their potential in various

areas such as industrial, pharmaceutical, food, etc. Many of these areas require a proper understanding of the viscoelastic behavior of these materials and hence rheological studies on LCLCs become significant. Apart from these practical applications, the rheology of LCLCs has fundamental relevance. As compared to the rheological studies on thermotropic liquid crystals, the rheology of LCLCs is not well studied. Sunset Yellow (SSY) is a very common food dye that belongs to the LCLC category which forms mesophases when dispersed in water. Apart from some shear rate dependent viscosity studies, the rheology of SSY is underexplored. We investigated the rheological behavior of the nematic phase of SSY liquid crystal, especially shear-induced microstructures and dynamics. Towards these studies, we prepared SSY LC samples (32 wt% SSY in water) with an aim to achieve the nematic phase. The nematic phase is confirmed by analyzing the polarizing optical microscopy (POM) images of the samples. The rheological measurements were carried out using a stress controlled MCR rheometer. We explored the rheological properties of SSY LC in the shear rate range of $10-100s^{-1}$. At a fixed temperature the flow curves exhibit three dynamic regimes; a near-near-plateau regime is surrounded by two Newtonian regimes. These nonmonotonic flow behavior and the stress dynamics are corroborated using in-situ rheomicroscopy. The rheo-microscopy reveals that, with increasing shear rate the defect-dispersed microstructure varies progressively and appears quite different in three regimes, with the nearnear-plateau regime having less orientation order and more disclination defects. The driving shear force in the near-plateau regime causes periodic stress oscillations which are similar to that observed in the worm-like micellar system and twist-bent nematic LCs. The stress oscillations in the case of twist-bent nematic LCs were theoretically explained to originate from the change of the pseudo-layer orientation with respect to the shear direction. For the micellar systems, it occurs due to the flow-concentration and flow-order (orientational) coupling that leads to the dynamic instability of shear bands. Considering the similarities

between micellar systems and studied chromonic systems (both are lyotropic nematics), the flow-concentration and flow-order coupling effects seem to be responsible for the mechanical instability and the resulting stress dynamics in the near near-plateau regime.

Chapter 5. Summary and Future work

This chapter presents the summary and conclusions of the studies conducted on viscoelastic systems of PNIPAM microgels and SSY liquid crystals.

LAOS studies conducted on dense PNIPAM microgel glasses conclude that the glassy state formed from dense suspensions of homogeneous core (HC) PNIPAM particles yield in a single step by exhibiting a single peak in G''. Whereas, dense suspensions of core-shell (CS) PNIPAM particles yield in two steps by exhibiting two peaks in G''. Single step yielding observed in dense HC-PNIPAM microgel glass is attributed to the breaking of topological cages formed by neighboring particles. Whereas, two-step yielding of dense CS-PNIPAM microgel glass is attributed to i) breaking of entanglements of dangling polymer chains between neighboring particles and ii) rupturing of topological cages formed by neighboring particles.

Shear induced flow measurements performed on SSY LC at the nematic phase conclude that, at a fixed temperature the system shows non-monotonic flow behavior (stress (σ)-strain rate ($\dot{\gamma}$) curves) by exhibiting three flow regimes (a near-plateau regime surrounded by two Newtonian regimes). This non-monotonic behavior is corroborated with the shear induced director orientation with respect to the flow direction.

.

List of Figures

Figure No.	Figure Caption	Page No.
Figure 1.1	Phase diagram of monodisperse colloidal suspensions of hard spheres.	4
Figure 1.2	Phase diagram of colloidal suspension of charged polystyrene particles (Adapted from Sirota <i>et al.</i> [43]. Closed circles: glass, closed square: bcc, open square: bcc-fcc coexistence, open triangle: fcc and open circle: liquid. Continuous lines are guide to the eye. The dashed line is the fcc-liquid phase boundary for a similar point charge Yukawa system.	6
Figure 1.3	(a) Temperature dependence of hydrodynamic diameter, d_h of PNIPAM microgel particle. (b) Schematic illustration of the structural transformation occurring across VPT for PNIPAM microgel.	8
Figure 1.4	(a) Radial polymer density profiles of PNIPAM microgel particle at different temperatures measured using SANS (Adapted from Stieger <i>et al.</i> [66]) and (b) Schematic diagram of core-shell morphology of PNIPAM microgel particle below VPT with core radius r_c and shell thickness ρ . Hydrodynamic radius $r_h = r_c/2$.	10
Figure 1.5	Schematic showing different layers of core-shell structured PNIPAM microgel particle modelled according to the MH pair potential. The centre to centre distance between PNIPAM microgel particles is denoted by r .	12
Figure 1.6	(a) Schematic illustration of MSD vst for HS particles in (I) gas-like state, (II) liquid-like state, (III) supercooled liquid state and (IV) crystalline/glassy state, of the suspensions. (b) Schematic representations of MSD vs t for colloidal particles in repulsive glasses (I) and attractive glasses (II). The short time values of α indicate the diffusive ($\alpha = 1$) and subdiffusive ($\alpha < 1$) behavior of MSD in repulsive and attractive glasses.	16

Figure 1.7	Schematic diagram showing the single step yielding (marked by arrow) of dense HS colloidal glass.	19
Figure 1.8	Schematic showing the typical linear viscoelastic response of a colloidal glass under frequency sweep. ω_{α} and ω_{β} stand for the alpha and beta relaxation frequencies of colloidal glass	21
Figure 1.9	Schematic diagram showing the two-step yielding (marked by arrows) of attractive colloidal glass.	21
Figure 1.10	Schematics showing the stacking of the LCLC molecules forming cylinders in the (a) N phase and (b) M phase. The director \hat{n} in each schematic is shown by arrows.	24
Figure 1.11	Molecular structure of Sunset Yellow (SSY) compound in (a) azo form and (b) hydrozone form.	26
Figure 1.12	(a) Phase Diagram of SSY adapted from A. Yamaguchi [124]. The LC phase of SSY depends on the concentration (wt%) and temperature (°C). Isotropic-nematic coexistence and nematic-columnar coexistence phases are represented by I+N and N+C respectively. (b) Schlieren texture observed in the nematic phase of SSY LC (32 wt % solution) under POM.	27
Figure 2.1	Schematic representation of the experimental set-up used for the synthesis of CS-PNIPAM microgel particles by batch method.	41
Figure 2.2	Schematic representation of the experimental set-up used for the synthesis of HC-PNIPAM microgel particles by semi-batch method.	43
Figure 2.3	Schematic diagram of sample cell for POM observations	48
Figure 2.4	Schematic diagram of DLS measurement set up	50
Figure 2.5	(a) Fluctuation in $A(t).\tau$ represents the time lag between t_1 and t_2 . (b) ACF of A(t).	50
Figure 2.6	(a) Schematic diagram of a 3D-DLS set up with cross correlation technique b) ray diagram showing scattering geometry of 3D light scattering setup. B-Beam splitter; M- Mirror; AOM- Acousto optic	55

	modulator; SC- Sample cell; APD- Avelanche photo diode; F- Fiber optic cable, L- Plano-convex lens	
Figure 2.7	Schematic diagram of UV-Visible spectrometer	59
Figure 2.8	(a) Iridescence from CS-PNIPAM microgel crystals under visible light illumination, at 21°C. (b) UV-Visible spectrum from CS-PNIPAM microgel crystals.	59
Figure 2.9	Simple shear experiment on a cuboidal object. The bottom plate is fixed while top plate is pulled by a shear force F . The geometry independent rheological parameters can be defined as, stress $(\sigma) = F/A$, strain $(\gamma) = dx/h$ and shear rate $(\dot{\gamma}) = d\gamma/dt = v/h$	61
Figure 2.10	Maxwell model that incorporates elastic effects for a viscous fluid: serial connection of a Hookean solid and a Newtonian liquid.	63
Figure 2.11	Photograph of MCR-501 rheometer (Anton Paar, Germany)	64
Figure 2.12	Schematic representation of cone-plate measuring system. The symbols indicate the following parameters: R_c - cone radius, φ - cone angle, h - gap between top and bottom plates at the edge, H - cone truncation, Ω - angular frequency	66
Figure 2.13	Schematic representation of parallel plate measuring system. The symbols indicate the following parameters: R_c - plate radius, h - gap between top and bottom plates, Ω - angular frequency.	67
Figure 2.14	Schematic diagram of <i>in-situ</i> rheo-microscopy (RM) setup. O, P and A indicates microscope objective, polarizer and analyzer respectively. The images are captured in the reflection mode.	69
Figure 2.15	(a) Phase difference, δ between strain (γ) and stress (σ) for a visco-elastic material and (b) vector representation of complex modulus (G^*) for visco-elastic material.	70
Figure 2.16	Stress vs strain during a cycle for various materials. (a) elastic material, (b) viscous material, (c) visco-	73

	elastic material under SAOS and (d) visco-elastic material under LAOS	
Figure 2.17	Schematic representation of shear rate vs shear stress plot for different fluids shows Newtonian, shear thickening and shear thinning flow behavior.	74
Figure 2.18	(a) Schematic illustrating the path of light through different components of a POM. (b) Schematic representation of uniaxial LCs between crossed polarizers.	75
Figure 3.1	Linear viscoelastic response of glass samples (a) CS-PNIPAM and (b) HC-PNIPAM in their glassy state (γ_0 = 10%). Arrows represent the approximate position of the minimum in G'' corresponding to the beta relaxation frequency, ω_{β} . (c) Schematic illustrating the typical linear viscoelastic response of colloidal glasses. ω_{α} and ω_{β} represent the alpha and beta relaxation frequencies of colloidal glass.	87
Figure 3.2	tan δ versus T for a fixed strain, γ_0 = 10% for dense glass samples of CS-PNIPAM (closed circle) and HC-PNIPAM (open circle) microgel particles. Left and right arrows indicate tan δ (Y -axis) for HC-PNIPAM and CS-PNIPAM respectively.	89
Figure 3.3	Yielding behavior of samples CS-PNIPAM and HC-PNIPAM in their glassy state. (a) Two peaks (marked with arrows) in $G''(\omega)$ indicate two-step yielding in sample CS-PNIPAM at $T=20^{\circ}$ C. (b) Single peak in $G''(\omega)$ indicated yielding in single step in HC-PNIPAM sample at $T=20^{\circ}$ C. Variation of G'' as a function of γ_0 with increasing temperature, T for samples (c) CS-PNIPAM and (d) HC-PNIPAM in their glassy state at $\omega=10$ rad/sec. Arrows indicate the evolution of peak(s) in G'' with increasing temperature.	90
Figure 3.4	The apparent cage modulus (G_{cage}) as a function of strain amplitude, γ_0 overlaid on the shear moduli (G' , G'') data of Fig. 3.3 for (a) CS-PNIPAM and (b) HC-PNIPAM. In the linear regime, G_{cage} coincides with G' whereas, it sustains for larger values of γ_0 .	91

г	T	1
Figure 3.5	(a) State (i) represents the unreformed state configuration of CS-PNIPAM microgel glass with R as reference particle having entangled neighbors 1, 2, 5 and 6 and topological neighbors 1–6. State (ii) shows that, upon application of lower yield strain, entanglements with 1, 2, 5 and 6 are broken leading to first peak in <i>G</i> ". State (iii) shows that, upon application of higher yield strain, topological neighbors of R changes due to cage breaking, which leads to second peak in <i>G</i> ". Arrow indicates the increasing direction of strain. (b) State (i) represents the unreformed state configuration of HC-PNIPAM microgel glass with R as reference particle having topological neighbors 1–6. State (ii) shows that, upon application of yield strain, topological neighbors of R changes due to cage breaking, which leads to a peak in <i>G</i> ". Arrow indicates the increasing direction of strain.	92
Figure 3.6	(a) Mean square displacement, $<\Delta r^2(t)>$ in units of average hydrodynamic diameter, d_h versus delay time, t showing particle dynamics in CS-PNIPAM (closed circle) and HC-PNIPAM (open circle) in their colloidal glassy state ($T=20$ °C). Lines represent the fit to Eq. 1.11 at the short time regime. Up and down arrows indicate the time-scale (x-axis) for microgel glasses of CS-PNIPAM and HC-PNIPAM particles respectively. Schematic (b) represents the cage of CS-PNIPAM particles with entanglements of dangling chains between nearest neighbor particles in the glassy state and schematic (c) represents the cage of HC-PNIPAM particles in its glassy state without the entanglements as there are no dangling polymer chains.	93
Figure 3.7	LB curves for the CS-PNIPAM sample (a-c) with ϕ = 0.80 and HC-PNIPAM sample (d-f) with ϕ = 0.89. (a) and (d) are in the linear regime of the samples ($\gamma_0 < 5\%$) and (b), (c), (e) and (f) are in the non-linear regime of the samples ($\gamma_0 > 5\%$) with strain amplitude increasing from left to right. Open circle and closed circle represent static yield stress as the maximum stress overshoot, and the dynamic yield stress at the	96

	point of zero instantaneous shear rate respectively. Figures (a) to (f) correspond to $T = 20^{\circ}$ C.	
Figure 3.8	Static yield stress at maximum elastic stress (closed circle) and dynamic yield stress at instantaneous zero shear rate (open circle) for (a) CS-PNIPAM and (b) HC-PNIPAM. Arrows represent the strain regime for CS-PNIPAM sample where gradual difference between static and dynamic yield stresses can be observed. Inset: static and dynamic yield stress determined in the entire deformation regime (a) for CS-PNIPAM and (b) for HC-PNIPAM. Dotted circles represent the region of interest where σ_{ys} and σ_{yd} becomes distinct and indicates yielding. The lines drawn are guide to the eye.	98
Figure 3.9	Dissipated energy calculated (a) for CS-PNIPAM and (b) for HC-PNIPAM from the LB curve using the equations 3.2 and 3.3 (E ₁) and dissipated energy calculated according to Donely <i>et al.</i> (2020) [42] (E ₂).	99
Figure 3.10	Strain amplitude, γ_0 dependence of yielding energy, E_Y for CS-PNIPAM (closed circle) and HC-PNIPAM (open circle) at $T=20^{\circ}$ C. Peaks in yielding energy (represented by arrows) of CS-PNIPAM are identified due to entanglement breaking and cage breaking. The lines drawn are guide to the eye.	100
Figure 4.1	Experimental setup for performing <i>in-situ</i> rheomicroscopy. Letters O, P and A indicate microscope objective, polarizer and analyzer, respectively. The microscope module is mounted on a xy stage (not shown).	107
Figure 4.2	(a). Flow curves (σ versus $\dot{\gamma}$) at different temperatures in the nematic phase of SSY LC (32 wt%). Different regimes are labelled as R1, R2 and R3 which are separated by the lower and upper critical shear rate ($\dot{\gamma}_{cl}$ and $\dot{\gamma}_{cu}$), respectively. (b) Shear-rate dependence of shear stress σ and shear viscosity η of the sample at T=24°C.	108
Figure 4.3	Temperature dependence of $\dot{\gamma}_{cl}$ (open circles) and $\dot{\gamma}_{cu}$ (closed circles).	109

Figure 4.4	Linear fit to (a) regime R1 and (b) regime R3 with $\sigma = K_i \dot{\gamma}$, where K_i is constant and $i = 1, 3$.	110
Figure 4.5	Regime R2 is fitted to $\sigma \sim \dot{\gamma}^{\beta}$ with $\beta \approx 0.36$ - 0.54. Solid lines are the best fits.	110
Figure 4.6	Representative rheo-microscopy images from three regimes R1, R2 and R3 at different shear rates at room temperature ($T = 24^{\circ}$ C). The shear rate value on each image is marked on the top. The flow direction is shown with a blue arrow at the left corner.	112
Figure 4.7	Variation of σ with $\dot{\gamma}$ measured using a plate-cone system (T = 24°C). Three regimes are shaded with different colours.	113
Figure 4.8	(a) Time dependent stress for the selected shear rates $\dot{\gamma} = 5 \ s^{-1}$ (R1), $33 \ s^{-1}$ (R2) and $100 \ s^{-1}$ (R3). (b) Fourier power spectrum corresponds to the stress fluctuations at $\dot{\gamma} = 33 \ s^{-1}$ in regime R2. Fundamental frequency $\omega = 2\pi f = 0.28 \ \text{rad/s}$ and a few harmonics are labelled. The angular frequency corresponding to the shear rate $\dot{\gamma} = 33 \ s^{-1}$ is $\Omega = \dot{\gamma} \tan(\varphi) = 0.28 \ \text{rad/s}$.	114

List of Tables

Table No.	Table Caption	Page No.
Table 2.1	Details of the chemical reagents used in the conventional synthesis of core-shell (CS) PNIPAM microgel particles	42
Table 2.2	Details of the chemical reagents used in the semi-batch synthesis of homogeneous core (HC) PNIPAM microgel particles	44
Table 2.3	Sample details of CS-PNIPAM and HC-PNIPAM dense microgel suspensions	46
Table 2.4	Particle analyzer Litesizer TM 500 : measurement specifications	49

Table 3.1	Sample details of CS-PNIPAM and HC-	83
	PNIPAM dense microgel suspensions	

List of Symbols

Number of colloidal particles in a suspension	N_p
Volume of colloidal suspension	V
Hard sphere diameter	d
Hydrodynamic diameter of PNIPAM colloidal particle	d_h
Volume fraction of colloidal suspension	ϕ
Number density of colloidal suspension	n_p
Hard sphere interaction potential	$U_{HS}(r)$
Screened Coulomb potential	$U_C(r)$
van der Waals attraction potential	$U_A(r)$
Strength of corona-corona interaction	U_{corona}
Strength of core-core interaction	U_{core}
Diameter of core	d_{core}
Diameter of corona	d_{corona}
Heaviside function	Θ
Distance between colloidal particles	r
Electron charge	e
Radius of charged colloidal sphere	a
Dielectric constant of the medium	ε
Inverse Debye screening length	k
Boltzmann constant	k_B
Temperature	T
Time	t
Solvent viscosity	$\eta_{\scriptscriptstyle S}$
Mean square displacement of colloidal particle	$<\Delta r^2(t)>$

Brownian time	$ au_B$
Cage rearrangement time	$ au_R$
Short time diffusion coefficient	D_s
Average diffusion coefficient	\overline{D}
Second cumulant	k_2
Third cumulant	k_3
Scattering volume	$v_{\scriptscriptstyle S}$
Number of point scattering centers in a colloidal particle	n
Scattering amplitude	$A_{\scriptscriptstyle S}$
Free diffusion coefficient	D_0
Coherence factor	$eta_{\!f}$
Effective Coherence factor	eta_{eff}
Normalized intensity auto correlation function	$g^2(q,t)$
Normalized electric filed correlation function	$g^1(q,t)$
Coherence factor due to instrument optics	eta_c
Non-ergodicity factor	Y
Coherence factor due to multiple scattering	eta_m
Coherence factor due to overlap of laser beams	eta_{12}
Normalized intensity cross correlation function	$g_{12}^{(2)}(q,t)$
Storage modulus	G'
Loss modulus	$G^{\prime\prime}$
Cage modulus	G_{cage}
Instantaneous strain	$\gamma(t)$
Amplitude of oscillatory strain	γ_0
Frequency of strain/stress oscillation	ω
Incident light wave vector	$ec{k}_i$
Scattered light wave vector	$ec{k}_{\scriptscriptstyle S}$
Scattering wave vector	$ec{q}$
Scattering angle	θ

Refractive index of solvent	μ_{s}
Wave length of incident light	λ
Position vector of the scattering center α_i in the i^{th} particle	$\vec{r}_{i,lpha_i}$
Normalized intensity auto correlation function	f(q,t)
Electric field scattered from N particles at time t	$E_s(q,t)$
The intensity of scattered light	$I_s(q,t)$
Decay constant	Γ
Illumination Intensity	I
Optical path length of the sample	L
Interparticle separation	d_{nn}
Wavelength corresponds to Bragg peak	λ_B
Mesh size	ζ
Coefficient of friction	ξ
Total strain	γ_t
Total strain rate	$\dot{\gamma_t}$
Relaxation time	λ_t
Angle of cone	φ
Radius of cone	R_c
Height of the cone from bottom plate	h
Angular speed of the rheometer tool	Ω
Torque	M_t
Imaginary number	i
Stress amplitude	σ_0
Phase shift between strain and stress	δ
Cone truncation	Н
Dynamic yield stress	σ_{yd}
Static yield stress	σ_{ys}
Dissipation energy	E_D
Yielding energy	E_Y
Total energy	E_T

Glass transition temperature	T_g
Analyzer	A
Polarizer	P
Objective	O
Cell thickness	t_c
Wavelength corresponds to m^{th} maxima or minima	λ_m
Wavelength corresponds to n^{th} maxima or minima	λ_n
Area of the cuboidal object	A_c
Height of the cuboidal object	h_c
Stress in the spring	$\sigma_{\scriptscriptstyle S}$
Stress in the dashpot	σ_d
Lower critical strain rate	Ϋ́cι
Higher critical strain rate	$\dot{\gamma}_{cu}$
Electric charge density	χ_{max}
Effective viscosity	K_i
Power law exponent	β
Shear viscosity	η
Frequency of power spectrum	f
Nematic phase	N
Columnar phase	C/M
Liquid Crystal Director	\widehat{n}

List of Abbreviations

PNIPAM Poly-N-isopropylacrylamide

PNIPAM-co-Aac Poly (N-isopropyl acrylamide-co-acrylic acid)

PMMA Poly methyl methacrylate

VPT Volume phase transition

LCST Lower critical solution temperature

SPD Size polydispersity

SDS Sodium dodecyl sulfate

KPS Potassium persulfate

BIS N, N'-Methelenebisacrylamide

fcc Face centered cubic bcc Body centered cubic

hcp Hexagonal close packed

rcp Random close packed

MSD Mean square displacement

AG Attractive Glass
RG Repulsive glass

DLS Dynamic light scattering

HS Hard sphere

MH Multi Hertzian

HC-PNIPAM Homogeneous core PNIPAM

CS-PNIPAM Core-shell PNIPAM

QELS Quasi elastic light scattering

PCS Photon correlations spectroscopy

ACF Auto correlation function

SAOS Small amplitude oscillatory shear

LAOS Large amplitude oscillatory shear

CP Cone and plate

PP Parallel plate

AOM Acousto-optic modulator

APD Avalanche photo diodes

NIR Near infrared

PMT Photo multiplier tube

FT Fourier transform

DSS Dynamic strain sweep

LB curve Lissajous- Bowditch curve

DSCG Disodium cromoglycate

SSY Sunset yellow

N_{TB} Twist bent nematic

CPyCl-NaSal Cetylpyridinium chloride-sodiumsalicylate

CTAT cetyl trimethylammonium tosylate

POM Polarized optical microscope

CCD Charge coupled device

INTRODUCTION

Everything between the length scale of sub-microscopic atomic nuclei (10⁻¹⁵m) and cosmos (10²⁶m) is measurable. Hence, the length scales can be used to distinguish the microscopic, mesoscopic, and macroscopic realms. The microscopic realm talks about atoms and molecules, whereas the macroscopic length scale ranges from our daily accessible objects to cosmological distances. The mesoscopic length scale connects the microscopic and macroscopic length scales and represents the region where microscopic behavior gradually changes into macroscopic behavior or vice versa. The systems in this mesoscopic realm are always exciting. Here, we explore the mesoscopic systems of colloidal suspensions and liquid crystals. The thesis presents experimental results on flow and deformation behavior of two soft matter systems viz; 1) PNIPAM colloidal suspensions, 2) SSY lyotropic chromonic liquid crystals.

1.1 Colloidal systems

olloidal suspensions are composite systems where microscopic particles (dispersed phase) are dispersed in a continuous phase (dispersion medium). An essential feature of the colloidal system is that the particles are in the size range from 10 nm to 1 μ m. The size limit serves to guarantee that the Brownian motion of the colloidal particles/spheres primarily arises from thermal fluctuations in the solvent, thereby influences the colloidal particle's dynamics. The study of colloidal systems relies to a vast extent on control of the physical stability of the suspension against aggregation due to the van der Waals

force of attraction. The stability can be achieved either by steric or charge stabilization. In the case of steric stabilization, a thin layer of polymer is added to the surface of the colloidal particle, whereas in the case of charge stabilization, electric charge is being created on the surface of the colloidal particles. Moreover, the sedimentation due to the gravitational effects in colloidal systems can be minimized by matching the density of continuous and suspended phases, hence enable them to mimic atomic states of matter where gravitational effects are typically negligible [1]. Colloidal suspension with less than 10% polydispersity (ratio of standard deviation to mean diameter) is considered monodisperse. Under favorable conditions, these monodisperse colloidal spheres exhibit gas-like [2], liquid-like [3-5], crystal-like [6,7] and even glass-like [8,9] phase behavior similar to that observed in atomic systems.

The typical timescale $(10^{-6}s-10^3s)$ on which processes occur in colloidal suspensions is much longer than in atomic systems which facilitates real-time observation of relevant physical processes. Moreover, the interparticle length in colloidal suspensions typically ranges from 100 nm -10 µm, which gives easy access to the experiments in real space using optical microscopy. The range of time scale and length scale enables the colloidal system to be used as a model system to study cooperative phenomena such as structural ordering and phase transition. These phenomena are also common to atomic and molecular systems but are quite difficult to observe in real space and real time. In the case of dense colloidal suspensions (with particle number density $\sim 10^{13}$ particles per cm⁻³), the typical value of elastic constants is ~ 10 dynes cm⁻², which is quite small when compared with elastic constant ($\sim 10^{12}$ dynes cm⁻²) of atomic systems (with particle number density $\sim 10^{23}$ particles per cm⁻³) [10,11]. For a colloidal crystal of 1 cm³ size, the latent heat of melting is in the order of μ Cal [12,13]. Proper scaling up of elastic constants and latent heat of melting of the colloidal crystal allows one to consider colloidal systems as macro version of atomic systems.

As colloidal systems mimic condensed matter systems, they are employed to explore many fundamental phenomena such as crystal nucleation and growth [7,14-17], glass transition [18-20], defects and dynamics in crystals [16,21,22], shear flows in glasses [23], fragility [24] and dynamical heterogeneity [18-20] in glasses, etc. In addition to the fundamental scientific importance, ordered structures of monodisperse colloidal dispersions are being researched due to their practical relevance, such as sensors [25-27], Bragg filters [28], optical switches [29,30], display devices [31], etc.

Colloidal suspensions have very low elastic constants. Hence, these systems can be deformed very easily by applying shear stress. This feature has been used in various industrial applications where colloidal suspensions are being sheared or deformed. Dense colloidal suspensions can be considered as viscoelastic solids, which have mechanical properties between ideal elastic solids and ideal viscous liquids [32]. These viscoelastic suspensions undergo yielding when subjected to large shear stress [32]. Investigation of the yielding of dense colloidal suspensions using rheological techniques is of practical importance for successfully formulating various industrial products including medicines, cosmetics, paints, inks, food items, etc.

1.1.1 Hard sphere colloids

Suspensions of hard spheres (HS) can be considered as the simplest colloidal system showing fluid and solid phases. They are considered impenetrable spheres that cannot overlap in space. HS colloids mimic the extremely strong repulsion that atoms and spherical molecules experience at very close distances. The potential, $U_{HS}(r)$ describing the interaction between HS colloids can be expressed as,

$$U_{HS}(r) = \begin{cases} 0, & r \ge d \\ \infty, & r < d \end{cases}$$
 (1.1)

where r is inter-particle distance and d is HS diameter. Sterically stabilized suspensions of poly (methyl methacrylate) (PMMA) serve as good example for HS suspensions [18,33]. The

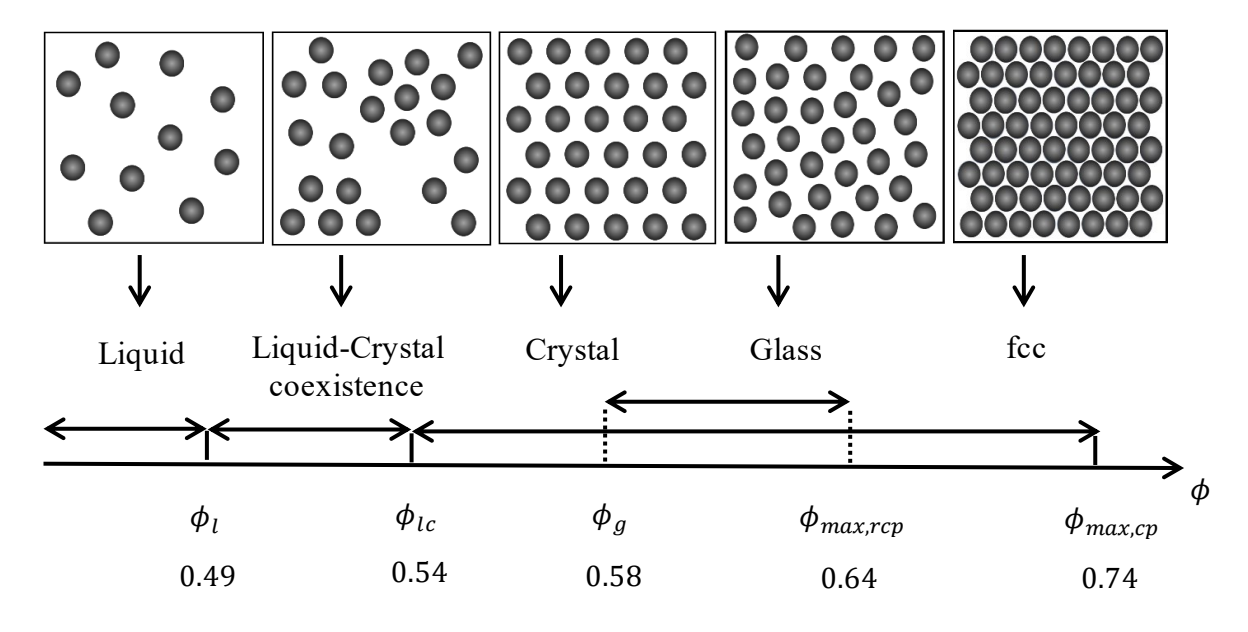


Fig. 1.1. Phase diagram of monodisperse colloidal suspensions of hard spheres.

phase behavior of HS colloidal suspensions can be tuned by using the only available control parameter, volume fraction $\phi (= n_p \pi d^3/6)$, where number density, $n_p = N_p/V$ is the number density of HS colloidal particles, with N_p as the number of colloidal particles in a solvent of volume, V). The phase behavior of monodisperse HS suspension as a function of ϕ is given schematically in Fig. 1.1 [33].

HS monodisperse suspensions exhibit a gaseous phase at very dilute conditions. Upon increasing the volume fraction beyond $\phi = 0.49$, HS suspensions show the coexistence of liquid and crystalline phases. Further increase in the volume fraction results in the complete crystallization of the suspension beyond $\phi_{lc}=0.54$, where ϕ_{lc} denotes the maximum volume fraction corresponds to liquid-crystal co-existence.

The entropically favoured crystal structure of HS colloidal suspension at $\phi = 0.74$ is face centered cubic (fcc) [34-36]. However, due to the very small difference ($10^{-3}k_BT$, k_B stands for the Boltzmann constant and T represents the temperature) in free energy between fcc and hexagonal close packed (hcp) structure, one can observe hcp structure and coexistence of fcc-

hcp under dense conditions [37,38]. Further increase of ϕ beyond ϕ_g = 0.58, the colloidal particle dynamics become slower and the suspensions freeze into a kinetically arrested disordered structure referred to as non-equilibrium glassy phase. The volume fraction corresponding to this phenomenon of glass transition is termed as glass transition volume fraction (ϕ_g = 0.58). In HS suspensions, a random close packed (rcp) glassy state will be formed at a volume fraction of ϕ = 0.64, where randomly arranged particles can touch each other, whereas the fcc and hcp structures of regularly ordered monodisperse HS can attain a maximum volume fraction, $\phi_{max,cp}$ = 0.74 (see Fig. 1.1).

The size polydispersity (SPD) of particles has a crucial role in determining the phase behavior of a colloidal suspension. The phase behavior is different for polydisperse and monodisperse colloidal suspensions [39]. Colloidal suspensions having SPD up to 10% are observed to exhibit crystalline ordering. It is observed that suspensions with higher SPD (>10%) freeze into a disordered (glassy) state [39].

1.1.2 Charge stabilized colloidal suspensions

Charge stabilized colloidal suspensions constitute a good example of a colloidal system where particles interact via electrostatic interactions which are predominantly repulsive [10,40,41]. Based on the Derjaguin–Landau–Verwvey–Overbeek (DLVO) theory, the net interaction potential between charged colloidal spheres, U(r) is the combined effect of screened coulomb repulsion, $U_C(r)$ and van der Waals attraction, $U_A(r)$.

$$U(r) = U_C(r) + U_A(r)$$
(1.2)

The screened coulomb repulsion [42] between charged colloidal spheres is given by,

$$U_C(r) = \frac{e^2}{\varepsilon} \left[\frac{Ze^{ka}}{1+ka} \right]^2 \frac{e^{-kr}}{r} \tag{1.3}$$

where e is the electron charge, Ze is the effective surface charge on the colloidal particle with Z being the number of monovalent charges. a is the radius of the sphere, ε denotes the

dielectric constant of the medium, r denotes the separation between the centres particles and k denotes the inverse Debye screening length, which can be expressed as,

$$k^2 = \frac{4\pi e^2}{\varepsilon k_B T} \left(n_p Z + C_S \right) \tag{1.4}$$

where C_s is the salt concentration, $n_p Z$ is the number of counter ions and k_B , T are Boltzmann constant and temperature respectively. The van der Walls attraction potential is given as,

$$U_A(r) = -\frac{A_H}{6} \left[\frac{2a^2}{r^2 - 4a^2} + \frac{2a^2}{r^2} + ln\left(\frac{r^2 - 4a^2}{r^2}\right) \right]$$
(1.5)

where A_H is the Hamaker constant. The charged colloidal spheres in a deionized suspensions at very low ϕ (~0.005) show crystal like ordering due to screened coulomb repulsion. Figure 1.2 shows the phase diagram of charge stabilized colloidal suspensions [43]. It can be seen from Fig. 1.2 that charge stabilized colloids at low ϕ and low C_S exhibit bcc (body centered cubic) ordering [44]. Upon increasing the ϕ beyond $\phi = 0.15$, coexistence of bcc-fcc was also observed for a range of ϕ and C_S as shown in Fig. 1.2. As C_S increases screened coulomb

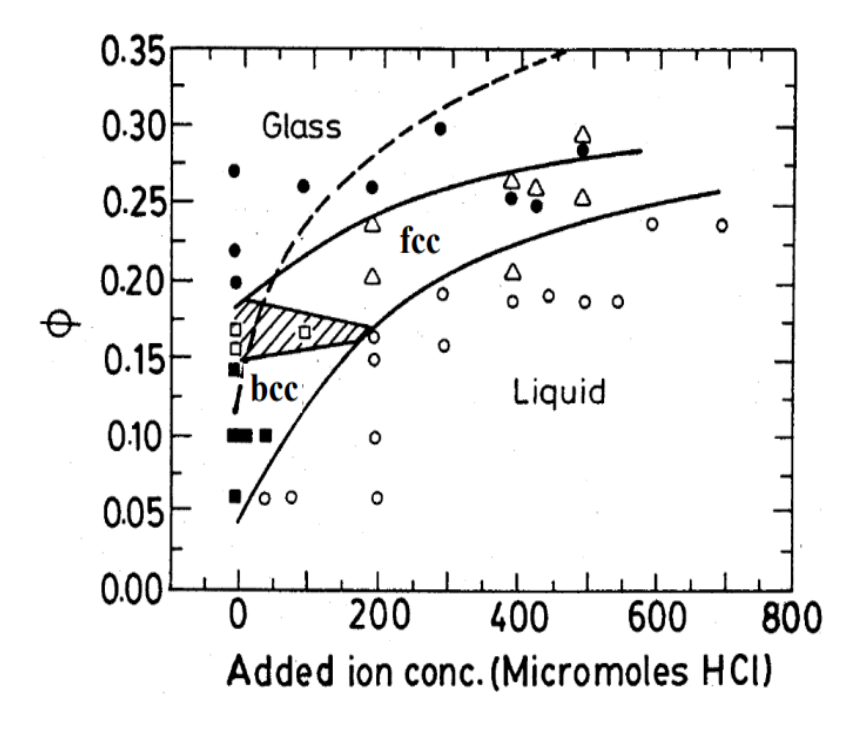


Fig. 1.2. Phase diagram of colloidal suspension of charged polystyrene particles (Adapted from Sirota *et al.* [43]. Closed circles: glass, closed square: bcc, open square: bcc-fcc coexistence, open triangle: fcc and open circle: liquid. Continuous lines are guide to the eye. The dashed line is the fcc-liquid phase boundary for a similar point charge Yukawa system.

interaction becomes weaker which results in the melting of crystalline order. At higher ϕ , suspensions freeze into a disordered glassy state. Since the particles interact via pure repulsive potential, the phase diagram of charge stabilized suspensions contains a fluid-solid phase, whereas a gas-liquid or gas-solid phase is absent.

1.1.3 Stimuli-responsive microgel suspensions

The size and polydispersity of colloidal particles of hard sphere and charge stabilized particles are fixed during the synthesis. Hence, the number density, n_n is the only parameter for tuning the phase behavior. In contrast, responsive microgel particles offer tunability in particle size in the presence of external stimuli such as temperature, pressure, pH, ionic strength, etc. The significant property of these responsive microgels is their swelling behavior in the presence of external stimuli. Microgel particles comprise a network of crosslinked polymer chains immersed in a solvent. They have a higher degree of crosslinking density inside the particle than in the periphery, as the cross-linker is consumed faster than the monomer during polymerization [45]. This leads to the inhomogeneous structure of microgel particles consisting of a dense core of crosslinked polymer chains and a fuzzy shell of dangling polymer chains as shown in Fig. 1.3(a) and Fig. 1.4(b). The change in external stimuli induces the polymer chains network to expand/contract, which causes gel particles to swell/deswell and results in an increase/decrease in particle size (Fig. 1.3). Poly-Nisopropylacrylamide (PNIPAM) is one of the most widely studied thermo-responsive microgel systems, which shows swelling/deswelling upon decreasing/increasing the temperature [46,47]. Depending upon the functionalization group incorporated during the synthesis of the PNIPAM microgel particle, it can respond to various stimuli like temperature [48], pH [49] and salinity [50,51].

1.1.4 Poly (N-isopropylacrylamide) (PNIPAM) microgels

a) Thermo-responsive characteristics of PNIPAM microgel particles

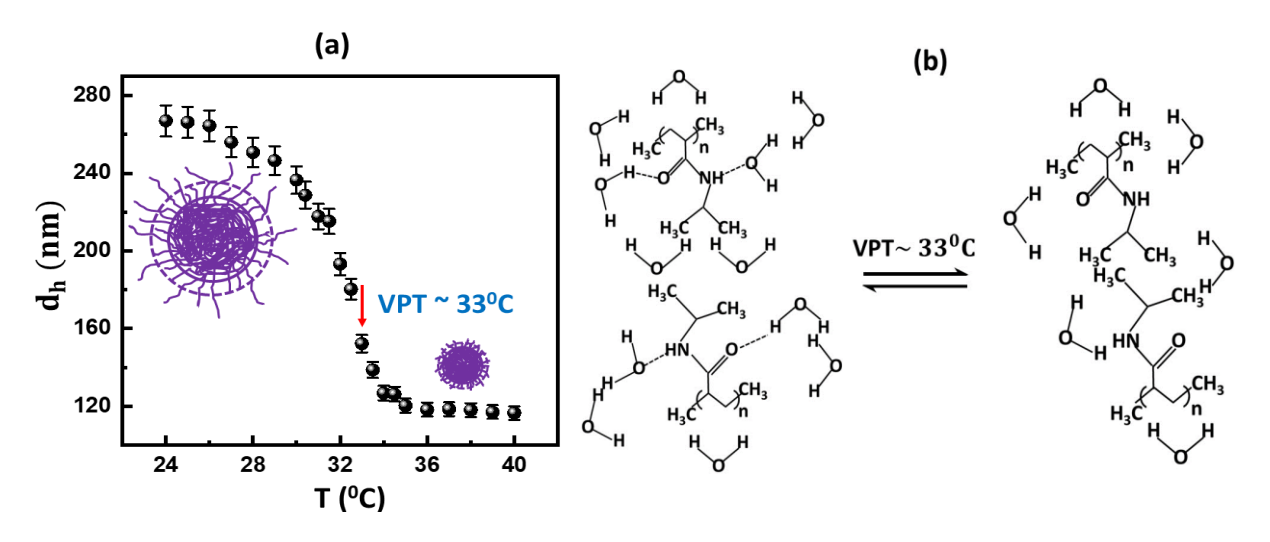


Fig. 1.3. (a) Temperature dependence of hydrodynamic diameter, d_h of PNIPAM microgel particle. (b) Schematic illustration of the structural transformation occurring across VPT for PNIPAM microgel.

Hydrogels based on poly(N-isoproylacrylamide) (PNIPAM) have received significant interest in the recent years due to their thermo-responsive behavior. PNIPAM microgel particles exhibit a remarkable reduction in their size as a function of temperature and experience a transition from a hydrated (swollen) state to a collapsed (shrunken) state at $T\sim33^{\circ}$ C, which refers to the volume phase transition (VPT) (shown in Fig. 1.3(a) [52-57]. This transition is reversible. It is attributed to the transformation of PNIPAM polymer chains from hydrophilic at temperatures below VPT to hydrophobic at temperatures above VPT [58,59]. As the schematic shown in Fig. 1.3(b), the monomer NIPAM is decorated with a hydrophilic amide group and a hydrophobic isopropyl group. Below the lower critical solution temperature (LCST, temperature at which NIPAM monomer undergoes a coil to globule transition), $\sim 33^{\circ}$ C, water molecules form hydrogen bonds with the acrylamide groups, effectively prevent the hydrophobic interaction. However, these hydrogen bonds break as the temperature rises above the LCST, and water molecules are released from the polymer chains. The hydrophobic interactions thus drive the polymer from a coil state to a globule state (inset to Fig. 1.3(a)) [60,61]. This coil-globule transition is reflected in the volume phase transition

of PNIPAM microgel particles. They undergo a volume phase transition around the same temperature where LCST occurs. PNIPAM microgel particles in their shrunken (collapsed) state consist of approximately 60% of polymer and 40% of solvent (water) [62]. In contrast, in the hydrated (swollen) state the polymer content is about 2-3% while the rest is water. Since PNIPAM microgel particles contain a significant amount of solvent in their hydrated state, the microgel suspension exhibits transparency below VPT. This transparency results from a close refractive index match between the microgel particles and the surrounding solvent, predominantly water. However, as the temperature increases above VPT, the polymer content within the particles increases ($\sim 60\%$). This high polymer density leads to poor refractive index matching between the particle and the solvent. Hence, the suspension appears turbid. Moreover, for the temperature above VPT, the microgel particle does not show a significant change in its size (Fig. 1.3(a)). Furthermore, by appropriate functionalization, PNIPAM microgels can be made responsive to pH known as poly (N-isopropyl acrylamide-co-acrylic acid) (PNIPAM-co-Aac) microgel particles [53] or various chemical moieties [54,55]. These stimuli responsive behaviors make PNIPAM microgels highly adaptable for a wide range of applications, such as sensing of different chemical elements and in solvent extraction. Additionally, the biocompatibility of PNIPAM microgels makes them suitable for controlled drug delivery applications [56].

b) Core-shell morphology of PNIPAM microgel particles

PNIPAM microgel sphere in its swollen state is highly hydrated and consists of roughly 2-3 % of the polymer [63]. The microgel particles form a network structure either by crosslinker polymer chains or by self-cross-linking of polymer chains [64,65]. These polymer chains extend throughout the volume of the microgel sphere. The microgel spheres are soft, deformable and allow solvent penetration. Typical conventional batch synthesis results in inhomogeneous PNIPAM microgel spheres with core-shell morphology (the synthesis

procedure is described in Chapter 2). Small angle neutron scattering (SANS) studies have been used to investigate the internal structure of PNIPAM microgel spheres, revealing their core-shell morphology (Fig. 1.4(a)) [63,66]. SANS studies have revealed that the PNIPAM microgel particle in its swollen state possesses a highly cross-linked polymer core surrounded by a thin fuzzy polymer shell (thickness \sim 20-30 nm). This polymer shell is decorated by dangling polymer chains as shown schematically in Fig. 1.4(b). Further, SANS measurements have revealed that during VPT, the core of microgel sphere experiences more deswelling in contrast to its shell due to the reduction in polymer network mesh size, ξ [63]. The concentration of the cross-linker (BIS) decides the size of the core and shell thickness [65]. With increased cross-linker concentration, the particle morphology is shown to transform from branching chains to a more compact particle. However, recent studies reported PNIPAM microgel spheres with uniform/homogeneous polymer density throughout the particle volume

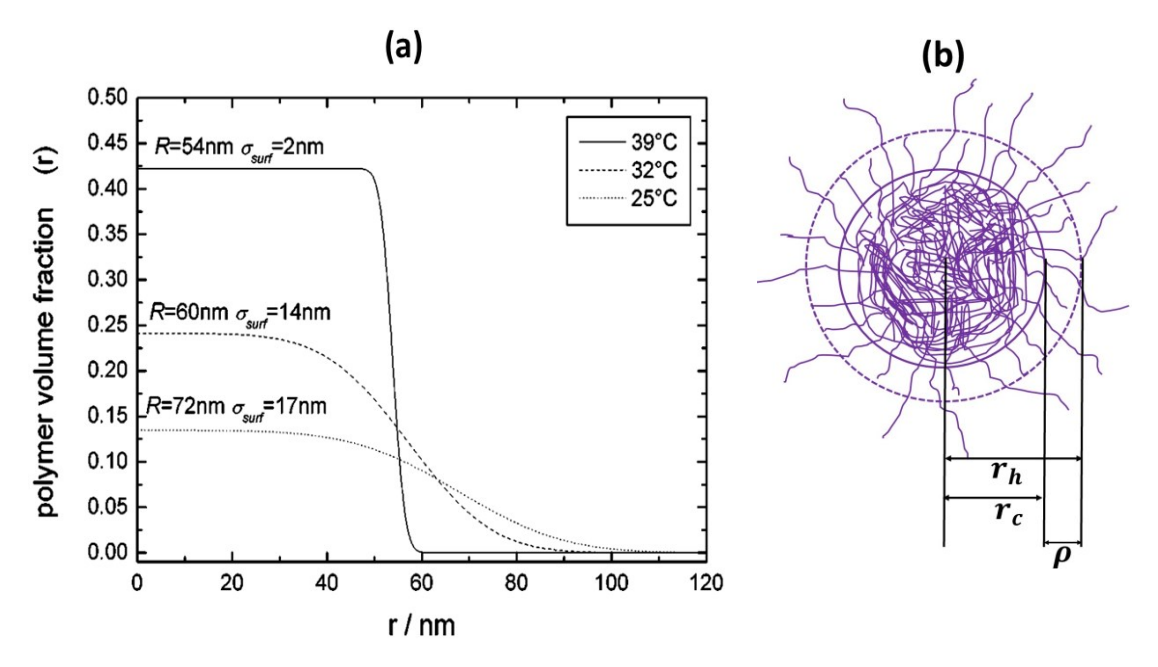


Fig. 1.4. (a) Radial polymer density distribution of PNIPAM microgel sphere at different temperatures studied using SANS (Adapted from Stieger *et al.* [66]) and **(b)** Schematic diagram of core-shell morphology of PNIPAM microgel sphere below VPT with core radius r_c , shell thickness ρ and hydrodynamic radius r_h .

[67,45].

c) Phase behavior of PNIPAM microgel suspensions

Since PNIPAM microgel particles are porous, they contain~97% water in their swollen state [63]. Hence, the refractive index of the PNIPAM microgel particle is closely matched with that of water. This refractive index matching helps to study the structural ordering and dynamics in dense microgel suspensions using light scattering experiments without the interference of multiple scattering of light. PNIPAM microgel suspensions display rich phase behavior (gas, liquid, crystal and glass-like structural ordering) under suitable conditions [52,48,68]. Since PNIPAM microgel particles are responsive to external stimuli such as T, pH or ionic strength, their hydrodynamic diameter, d_h and hence interparticle interaction, U(r) can be varied. Moreover, it has been reported that PNIPAM microgel glasses and crystals undergo melting upon increasing the temperature [52,58].

The soft characteristics of PNIPAM microgel spheres makes them compressed under osmotic pressure [69]. Hence, PNIPAM microgel particles can be over packed ($\phi > \phi_{cp}$) in a suspension [70]. The softness of the microgel particle is highly influenced by the cross-linker concentration. It has been reported that the softness of PNIPAM microgel particles and cross-linker concentrations are inversely proportional [24,52].

Although the phase behavior of the soft sphere system is being elucidated by assuming an interaction of the form $U(r) = (d/r)^n$, an exact form of the interaction potential governing their phase behavior in response to external stimuli is still unidentified. According to this model, upon increasing the degree of softness (1/n), liquid to crystal transition shifts to higher ϕ and the coexistence region between liquid and crystal narrows down compared to that of the HS system [71,72]. The freezing point in the case of PNIPAM microgel suspension was observed to be at higher value of ϕ as compared to what was predicted and experimentally determined for hard spheres ($\phi_f = 0.494$) [52]. This intriguing experimental observation

suggests that the phase behavior of PNIPAM microgel suspension at low temperatures, T can be explained by a soft repulsive potential.

Recently, Bergman *et al.* [73] have proposed a multi-Hertzian (MH) pair-potential (Eq. 1.6) by modeling the core-shell morphology of thermo-responsive PNIPAM microgel spheres. This core-shell morphology of PNIPAM microgel sphere is segmented into various layers as shown in Fig. 1.5, where d_{core} and d_{corona} are the diameters of core and corona respectively. A middle layer is defined in a way that $d_{mid} = (d_{core} + d_h)/2$. According to MH potential PNIPAM microgel particles interact with each other through a repulsive form of potential, U(r) and it consists of core-core, core-corona, and corona-corona interactions. The interactions between different layers of the spherical microgel particle are represented by the coefficients U_{cc} , U_{corona} , U_{mid} and U_{core} . The magnitudes of these quantities depend on the polymer density of the individual layers, which in turn are influenced by the temperature. Here θ refer to the Heaviside functions. Bergman *et al.* [73] tested the applicability of MH potential in the fluid area of PNIPAM microgels (up to $\phi = 0.49$) and up to the VPT temperature (33°C) of PNIPAM microgel particle.

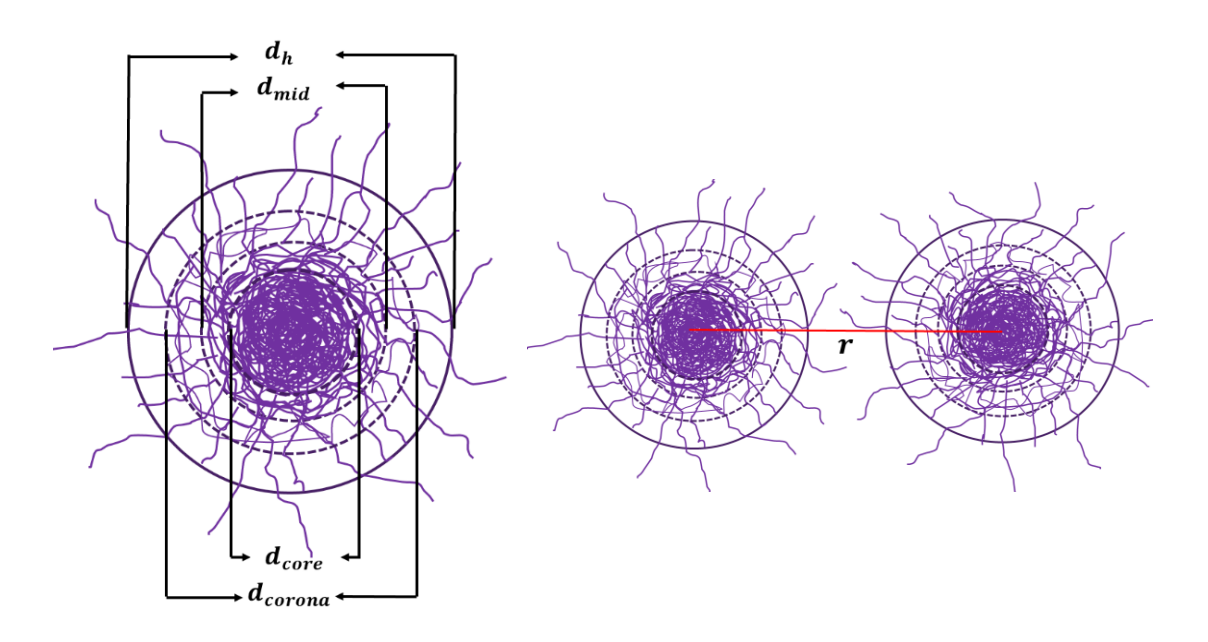


Fig. 1.5. Schematic showing different layers of core-shell structured PNIPAM microgel particle modelled according to the MH pair potential. The separation between the centres of PNIPAM microgel particles is denoted by r.

$$U(r) = U_{CC} \left(1 - \frac{r}{d_h} \right)^{\frac{5}{2}} \Theta(d_h - r) + U_{corona} \left(1 - \frac{r}{d_{corona}} \right)^{5/2} \Theta(d_{corona} - r)$$

$$+ U_{mid} \left(1 - \frac{r}{d_{mid}} \right)^{\frac{5}{2}} \Theta(d_{mid} - r) + U_{core} \left(1 - \frac{r}{d_{core}} \right)^{5/2} \Theta(d_{core} - r)$$
(1.6)

1.1.5 Dynamics of colloidal particles

Monodisperse colloidal suspensions exhibit structural ordering and phase behvior that closely resemble those observed in atomic systems. However, due to the presence of solvent, the dynamics in colloidal systems differ from that of atomic systems. Colloidal particles show Brownian dynamics when suspended in a solvent. Brownian dynamics refer to the random movement of particles suspended in a solvent resulting from collisions with the solvent molecules. The Brownian motion of colloidal particles of mass m in the solvent is mainly influenced by the frictional force $F_c(t)$ and some random force F(t) which is best described by the Langevin equation of motion [74] as follows,

$$m\frac{dV(t)}{dt} = F(t) + F_c(t) \tag{1.7}$$

The frictional force depends on velocity as $F_c(t) = -\xi V(t)$ with ξ as the coefficient of friction and V(t) as the velocity of the colloidal particle. As a result of viscous drag, the colloidal particle in the solvent over damped. When a spherical particle suspended in Newtonian fluid, ξ is provided by the Stokes equation as $\xi = 6\pi a \eta_s$, with a as the colloidal particle radius and η_s as the solvent viscosity [60]. The random force, F(t) originates from the fluctuations of solvent molecules leading to collisions that either accelerate or decelerate the motion of the colloidal particle. The velocity of colloidal particles, which show Brownian motion in the solvent, can be determined by solving Eq. 1.7. which is shown in Eq. 1.8.

$$V(t) = V(0) \exp\left(-\frac{\xi}{m}t\right) + \int_0^t d\tau \, \exp\left(-\frac{\xi}{m}(t-\tau)\right) F(\tau)$$
 (1.8)

The velocity correlation function calculated by averaging over Maxwell velocity distribution, can be expressed as,

$$\langle V(t)V(0)\rangle = \langle V(0)\rangle^2 \exp\left(-\frac{\xi}{m}t\right) = \frac{3k_BT}{m}\exp\left(-\frac{\xi}{m}t\right)$$
(1.9)

The random force and the initial velocity V(0) are uncorrelated (i.e. $\langle F(t)V(0)\rangle = 0$); therefore, upon averaging the second term in the equation, Eq. 1.8 disappears. The Brownian motion of the colloidal particle can be characterized by determining the mean square displacement (MSD) of the colloidal sphere. MSD of the particle is determined from the velocity correlation function using Eq. 1.10 [74],

$$\langle \Delta r^{2}(t) \rangle = 2 \int_{0}^{t} d\tau (t - \tau) \langle V(\tau)V(0) \rangle$$
 (1.10)

MSD can be divided into three distinct time scales viz., short time, intermediate time and long time. The time scales are determined based on Brownian time (τ_B) and cage rearrangement time (τ_R). Where $\tau_B (= m/\xi)$ is the time required to decouple the dynamics of the colloidal particle from that of the solvent and $\tau_R (= a^2/D_0, a)$: radius of the colloidal particle, D_0 : free diffusion coefficient) is the time required for the colloidal particle to traverse its own diameter. Short time scale is defined for $\tau_B \ll t \ll \tau_R$ whereas $t \gg \tau_R$ termed as long time scale. The intermediate time scale is referred when $t \approx \tau_R$ [75].

Typical dynamics of colloidal particles with different n_p is schematically shown in Fig. 1.6. The power law fitting to the MSD ($\langle \Delta r^2(t) \rangle$) using Eq. 1.11 distinguishes the dynamics into diffusive or sub-diffusive.

$$\langle \Delta r^2(t) \rangle \propto t^{\alpha}$$
 (1.11)

Where α represents the time exponent in the power law fit.

a) Non-interacting colloidal suspensions:

In a dilute colloidal suspension (gas-like), the motion of a colloidal particle is free diffusive ($\alpha = 1$) for all the time scales.

Therefore,
$$\langle \Delta r^2(t) \rangle \propto t$$
 or $\langle \Delta r^2(t) \rangle = 6D_0 t$

Where D_0 is the free diffusion coefficient which describes the diffusive motion of the colloidal particle in a non-interacting suspension (Fig. 1.6(a)-I).

b) Interacting colloidal suspensions:

In moderately dense (liquid-like ordered) suspensions, colloidal particles are observed to show slower dynamics in the short time scale with a short time diffusion coefficient $D_s < D_0$. The slower dynamics of colloidal particle in the short time scale is due to hydrodynamic interactions [76]. Further, at a longer time scale, colloidal particles experience direct interparticle interactions coupled with hydrodynamic interactions resulting in further slowing down of diffusive motion, which is characterized by a long time diffusion coefficient D_L [76]. The schematic illustration of MSD of colloidal particles in a liquid-like ordered suspension is shown in Fig. 1.6(a)-II. The change of slope of MSD plot (Fig. 1.6(a)-II) at intermediate time scale indicates the change of diffusion coefficient from D_S to D_L . Colloidal particles in the supercooled liquid state are confined within the cage formed by neighboring particles [18]. At shorter time scales, they exhibit diffusive dynamics (characterized by D_s) within the cage. At intermediate times, the particle experiences a cage from nearest neighbor particles, making its motion sub-diffusive ($\alpha < 1$). The sub-diffusive behavior of the colloidal particle can be identified as a plateau in MSD at intermediate times as shown in Fig. 1.6(a)-III. However, as these cages are dynamic in nature, at longer time scales, the colloidal particle jumps out of the cage, exhibits diffusive motion with a diffusion coefficient D_L . In crystals or glasses, long time diffusion ceases, while shorter time motion continues. Hence, D_L becomes zero and D_S remains exist (Fig. 1.6(a)-IV) [18,60].

According to Eckert *et al.* [61], attractive interactions can be induced between the particles of HS glass via depletion attraction by adding a non-adsorbing polymer. This leads to the initial melting of the glass into liquid. Further increase in the strength of attractive interaction results in a novel glassy state known as the attractive glass (AG), where particles

are bonded together via attractive interactions. The kinetic arrest of the colloidal particle in AG occurs due to attractive interaction between the particles and the confinement of particles within the nearest neighbor cage [61]. MSD's of repulsive glass (RG) and attractive glass (AG) are compared in Fig. 1.6(b). In the case of RG, MSD shows a plateau at a long time scale due to the kinetic arrest of particle motion inside the nearest neighbor cage, whereas MSD shows diffusive behavior ($\alpha = 1$), at a short time scale as depicted in Fig. 1.6(b)-I). In contrast, MSD of AG at short time shows sub-diffusive behavior [62] and attains saturation limit of RG at significantly long times, as depicted in Fig. 1.6(b)-II.

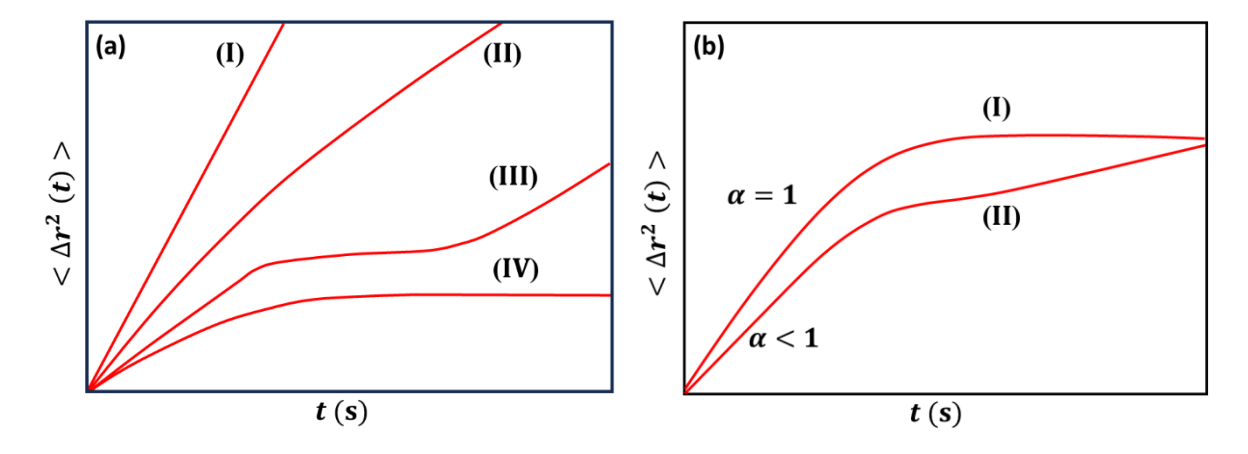


Fig. 1.6(a) Schematic illustration of MSD vs t for HS particles in (I) gas-like state, (II) liquid-like state, (III) supercooled liquid state and (IV) crystalline/glassy state, of the suspensions. (b) Schematic representations of MSD vs t for colloidal particles in repulsive glasses (I) and attractive glasses (II). The short time values of α indicate the diffusive ($\alpha = 1$) and subdiffusive ($\alpha < 1$) behavior of MSD in repulsive and attractive glasses.

1.1.6 Rheological insights and industrial advancements

Rheology is a scientific discipline that mainly deals with the flow and deformation of materials under the influence of an external force or stress [32]. It offers valuable insights into the mechanical properties and behavior of a variety of substances, from simple liquids to complex viscoelastic materials such as colloids, gels, polymers, liquid crystals, biological tissues, etc. Viscoelastic materials show unique combinations of viscous and elastic properties, and hence, they occupy a significant place in the field of soft matter. Their rheological properties, such as viscosity, elasticity are often used to characterise the behavior

of these materials under stress. Understanding and quantifying rheological properties are crucial in various industries, including petroleum, food and beverages, paints and coatings, pharmaceuticals, material science, rubber technology, and structural engineering.

Rheology plays a crucial role in the petroleum industry, specifically in the exploration, production, and refining of crude oil and its derivatives. Understanding the rheological characteristics of petroleum fluids is essential for optimizing a number of processes and operations. This includes measuring viscosity to determine the flow behavior of crude oil through pipelines, resulting in efficient transportation. Furthermore, the rheological qualities of petroleum products like lubricants and greases have a direct impact on their performance and durability. The petroleum industry can increase productivity, optimize the formulation and refining of petroleum-based materials and maintain safety standards through the study of rheology. [77,78].

Rheological studies have significant importance in the food industry. Food processing activities such as mixing, dispersing, pumping, dosing, spraying and extrusion benefit greatly from rheological studies. A comprehensive understanding of the flow and deformation behavior of food materials during these operations enables manufacturers to optimize equipment design, modify process parameters, and ensure the efficacy of food production. Monitoring the rheological properties of food products enables manufacturers to evaluate product stability, identify changes in texture or viscosity that may indicate deterioration or decomposition, and maintain quality consistency over extended periods. Therefore, rheological research in food science is closely linked to the development of food products and has implications for industrial food production, domestic cooking, and food consumption.

Rheological studies are extremely important in the paint industry [80,81] and influence paint production and performance at various phases. The rheological characteristics of paints,

such as viscosity and thixotropy, have a substantial impact on their flow behavior, leveling ability, and sag resistance during application. By carefully tuning the rheological properties, manufacturers can achieve the desired consistency and workability of paint formulations, assuring a smooth and uniform application on a variety of surfaces. Additionally, rheological measurements also help in optimizing the flow behavior of paints, ensuring proper film thickness and minimizing defects like brush marks or roller streaks. Understanding the rheology of paint and its related products helps in avoiding problems like sedimentation or phase separation, which ensure its longer life.

Apart from the above mentioned industrial applications, rheology has fundamental relevance. Here, we will investigate fundamental rheological behavior, such as the yielding and flow behavior of systems of two well-accepted smart materials i) thermo-responsive PNIPAM microgel particles and ii) Sunset Yellow (SSY) chromonics. PNIPAM microgel particles are spherical, and their colloidal suspensions exhibit isotropic behavior. Due its responsive nature, PNIPAM microgel particles are well accepted in the field of pharma and drug delivery. The SSY chromonic molecules are disk-shaped, which show anisotropic properties. Being a food dye, SSY is extensively used in the food industry. Since both the above mentioned viscoelastic systems are widely accepted in various industrial areas, studying their rheological behavior is highly important.

1.1.7 Yielding behavior of hard sphere colloidal glasses

Colloidal suspensions are viscoelastic in nature. The properties of viscoelastic materials lie between that of ideal elastic solids (follow Hooks' law of elasticity, $\sigma = G\gamma$, where σ is stress, γ is strain and G is the shear modulus) and ideal viscous liquids (follow Newton's law of viscosity, $\sigma = \eta \dot{\gamma}$, where η is the viscosity) [32]. The viscoelastic response is generally expressed in terms of storage/elastic modulus (G') and loss/viscous modulus (G''). G' describes the elastic properties, whereas G'' describes the viscous properties of the material.

If G' > G'' in a viscoelastic material, then material is predominantly elastic and shows solid-like behavior. Whereas, if G'' > G' then material is predominantly viscous and exhibits liquid-like behavior. Both G' and G'' can be measured by deforming the viscoelastic material using an oscillatory shear of the form $\gamma(t) = \gamma_0 \sin(\omega t)$. Where ω represents the oscillation frequency and γ_0 represents the amplitude of deformation.

A typical strain sweep measurement (with fixed ω and varying γ_0) performed on an HS suspension close to glass transition is shown in Fig. 1.7. Both G' and G'' exhibit a plateau for low γ_0 , which essentially indicates the linear deformation regime of the colloidal suspension. However, beyond the linear regime of the sample, G' and G'' starts varying with γ_0 . Eventually, above a critical strain (strain at which G' = G'', called yield strain) the suspension transforms from a solid-like ordering (G' > G'') to liquid-like ordering (G'' > G') by the process called yielding [83]. It is reported that in the case of HS colloidal glasses where particles are caged by nearest neighbors, yielding happens through irreversible rearrangement of colloidal particles (cage breaking) when subjected to external shear [83,84]. During yielding, G' undergoes a monotonic decrease with an increase in γ_0 , while G'' exhibits a peak. G'' shows peak at $\gamma_0 \sim 10\%$ where colloidal particles rearrange irreversibly (breaking of nearest neighbor cage), suggesting that the peak in G'' is associated with cage breaking.

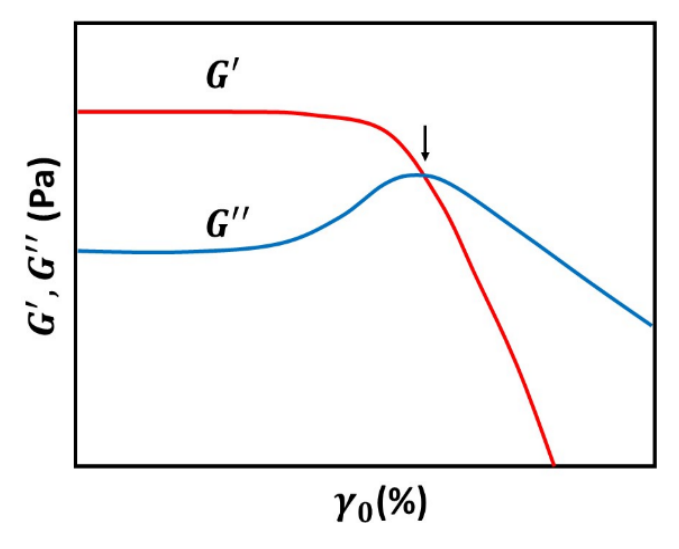


Fig. 1.7. Schematic diagram showing the single step yielding (marked by arrow) of dense HS colloidal glass.

A peak in G'' is a distinctive feature of soft glassy materials [82-85]. The rheological model of soft glass [85] states that the peak in G'' arises as the colloidal particles experience activated barriers from the nearest neighbor cages during the shear flow. Later, Miyazaki *et al.* [82] reported that the peak in G'' is a generic feature of materials with slow relaxation times and can be present even in the absence of activated barriers. Further studies have revealed that the peak in G'' arises due to a decrease in the relaxation time of the materials with an increase in shear rate [82,86]. In the case of HS glasses, this relaxation time specifically refers to alpha or slow relaxation time τ_{α} . For a given shear rate, $\dot{\gamma}$ the apparent relaxation time τ can be expressed as,

$$\frac{1}{\tau \dot{\gamma}_0} = \frac{1}{\tau_\alpha} + K \dot{\gamma}_0^{\nu} \tag{1.12}$$

Where $\dot{\gamma}_0 (= \gamma_0 \omega)$ is the shear rate, ν represents an exponent and K stands for a constant. The peak in G'' occurs at which $\dot{\gamma}_0 \sim \frac{1}{\tau}$.

The frequency sweep measurements (for a constant small γ_0) performed by varying the angular frequency, ω are generally used to determine the relaxation times in the colloidal suspensions. Small γ_0 ensures that the material is deformed linearly and within the plateau regime. The material's stress response in terms of G' and G'' under linear deformation by frequency sweep is schematically shown in Fig. 1.8. Suspension will be completely relaxed (G''>G') at small ω thereby indicating liquid-like ordering. Upon increasing ω , both G' and G'' increase and intersect each other at $\omega_{\alpha'}$, which is the alpha relaxation frequency. At this frequency, the corresponding shear rate $\dot{\gamma}_0(=\gamma_0\omega_\alpha)$ equals to the invers of alpha relaxation time $(1/\tau_\alpha)$. Above the cross-over frequency ω_α , G' dominates over G'' (i. e. G'>G'') with maintaining a constant value whereas, G'' starts to decrease leads to the appearance of a peak. G'' continuous to decrease till $\omega=\omega_\beta$ (beta or fast relaxation frequency), where it attains its minimum and again starts increasing beyond ω_β . However, at higher ω , both the

G' and G'' increase by exhibiting a power law behavior. τ_{α} and τ_{β} in the colloidal glasses can be calculated from the peak and minimum in G''. When the colloidal glass undergoes significant deformation with large γ_0 , the peak in G'' (depicted in Fig. 1.8) shifts to higher ω due to decrease in τ_{α} with increase in $\dot{\gamma}_0[82,86]$.

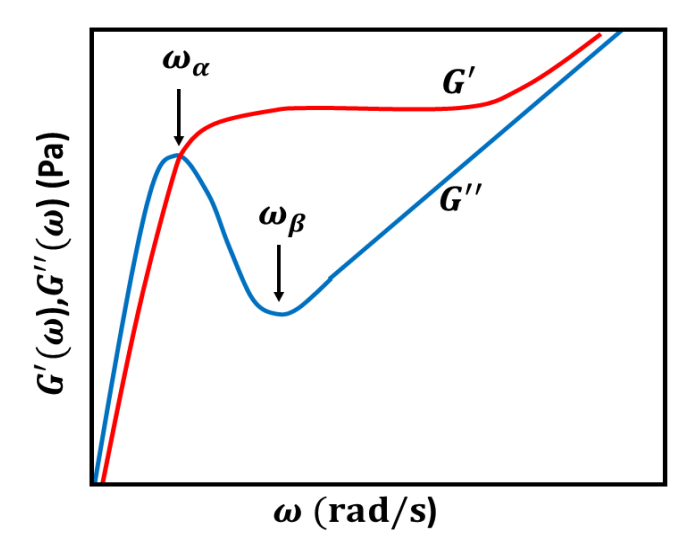


Fig. 1.8. Schematic showing the typical linear viscoelastic response of a colloidal glass under frequency sweep. ω_{α} and ω_{β} stand for the alpha and beta relaxation frequencies of colloidal glass.

1.1.8 Yielding behavior of attractive colloidal glasses

Apart from the caging of nearest neighbors, the colloidal particles of attractive glass (AG) are bonded by attractive interactions. Hence, the yielding behavior of AG differs from that of

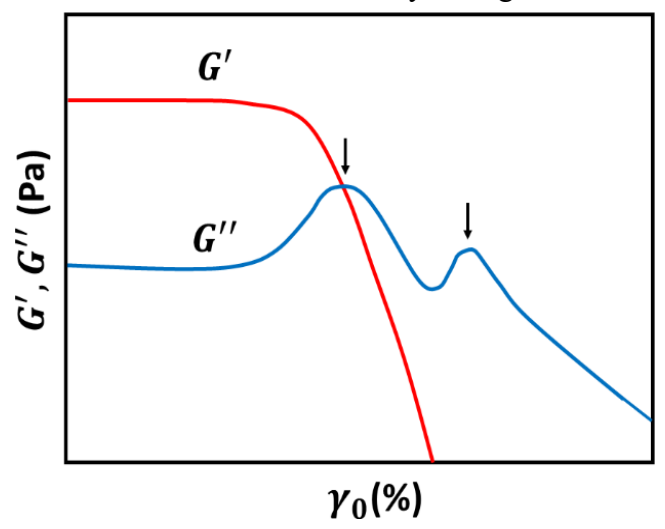


Fig. 1.9. Schematic diagram showing the two-step yielding (marked by arrows) of attractive colloidal glass.

hard sphere (HS) glass. While HS glass yields by exhibiting a single peak in G'' (Fig. 1.7), AG is observed to yield by exhibiting two peaks in G'' (Fig. 1.9) [87]. The kinetic arrest of colloidal particles in AG is reported to be due to the caging of nearest neighbors and bonding due to attractive interaction. The occurrence of two peaks in G'' in the yielding of AG is interpreted by Pham *et al.* [87]. According to Pham *et al.* the first peak at lower strain is due to the breaking of interparticle bonds, while the second peak at higher strain is attributed to the rupturing of topological cages formed by nearest neighbor particles.

1.2 Liquid crystals

Liquid crystals (LCs) are the states of matter that lie between purely disordered (isotropic) liquids and three-dimensionally ordered solid crystals. The molecules in the LC state show long range orientational order apart from 1D or 2D positional order. Liquid crystalline mesophases exhibit liquid-like characteristics, such as viscosity, surface tension, etc. At the same time, they show solid-like characteristics such as anisotropy in optical (birefringence), electrical (dielectric), and magnetic properties (diamagnetic susceptibility) [88,89]. They exhibit elastic properties and are capable of transmitting torques. Their unique thermodynamic, structural, rheological, and optical properties make them extremely useful for various technological applications, including optical elements, display devices, medicine, textile and food technology [90,91]. There are two primary classifications for liquid crystals: thermotropic liquid crystals (TLCs) and lyotropic liquid crystals (LLCs). This classification has been made according to the change in the thermodynamic variable that results in a phase change. TLCs exhibit different mesophases based on variations in temperature and pressure [92]. The basic building blocks of TLCs are generally individual molecules with distinct shape anisotropy, like rods or disks. Due to their unique features, they have been successfully implemented in display devices. LLCs are formed when lyotropic LC molecules dissolve in a solvent, typically in water. The mesophases are formed in lyotropic LCs due to change in solute concentration [93]. A key feature distinguishing lyotropic LCs from thermotropic LCs is the self-assembly of lyotropic LC molecules into supermolecular structures, which serve as the basic units for these mesophases [90,91].

1.2.1 Lyotropic Chromonic Liquid crystals (LCLCs)

In the past decade, following the initial research by Lydon, Attwood, Tiddy, and their coworkers [94-96], there has been a significant rise in interest concerning a special type of lyotropic LCs known as lyotropic chromonic liquid crystals (LCLCs). LCLCs offer a unique combination of some of the advantages of lyotropic and thermotropic LCs. The unique features of LCLCs make them distinct and offer promising applications [97-99]. Sandquist reported LCLCs for the first time in 1915 and have attained significant attention in the last three decades but are still an underexplored class of lyotropic liquid crystals [94,98,100,101]. A wide variety of materials, including drugs [94-96, 102], dyes [103-108], and DNA nucleotides like guanosine derivatives [109, 110], can form chromonic liquid crystal phases. The generic term "chromonic" derived from the antiasthmatic drug "disodium cromoglycate (DSCG)", which remains the most extensively investigated compound within this category [111,112]. The name "chromonic liquid crystals" was considered to be appropriate, as it fortunately combines connotations of color (referring to dyes) and chromosomes (referring to nucleic acids). The fundamental structural unit in LCLCs has a distinct geometry compared to the spherical or cylindrical micelles and bilayers formed by amphiphilic molecules in the traditional lyotropic LCs. LCLC molecules contain a disk-like or plank-like rigid aromatic core surrounded by hydrophilic ionic or hydrogen-bonding solubilizing groups at the periphery. When dissolved in water, chromonic molecules tend to stack on top of each other (known as H-aggregation) while leaving the solubilizing ionic groups at the interface between the aggregates and water [94, 113, 114]. A schematic view of LCLC molecular stacking is given in Fig. 1.10 [111,112,103]. So far, the aggregation mechanism has primarily been

attributed to the $\pi - \pi$ interaction between the aromatic centres, while the surrounding hydrophilic ionic or hydrogen bonding groups are responsible for solubility. This stacking

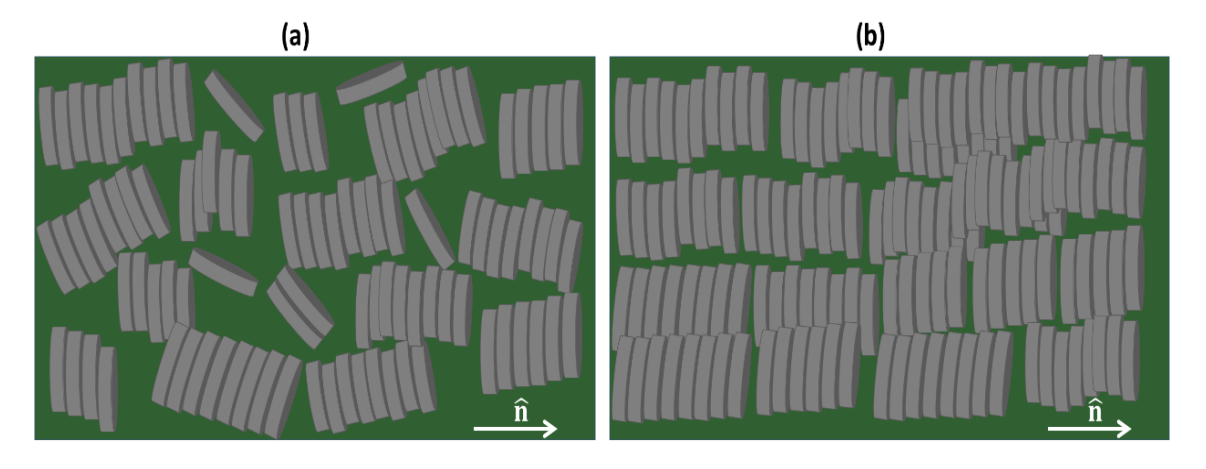


Fig. 1.10. Schematics showing the stacking of the LCLC molecules forming cylinders in the (a) N phase and (b) M phase. The director \hat{n} in each schematic is shown by arrows.

arrangement of LCLC molecules has been confirmed by x-ray diffraction studies and polarized UV-vis spectroscopic measurements on various LCLCs [103, 104, 112,115,116].

The typical stacking periodicity between the adjacent molecules in H-aggregates is determined to be \sim 0.33 - 0.34 nm as measured by x-ray diffraction [103,104,112]. However, this stacking separation does not depend on the concentration of the chromonic and the phase of solution, indicating that it is a fundamental characteristic of the chromonic aggregates. When the polar groups within the LCLC molecules are fully ionized, the electric charge density can become remarkably high, $\chi_{max}\sim$ 6e/nm (where e represents the electron's charge) in assumption that one molecule is present in the cross-section of the cylindrical stack. The process of aggregate self-assembly in LCLCs is analogous to the mechanism leading to the formation of worm-like micelles observed in surfactant molecule solutions. Unlike lyotropic surfactant systems, LCLCs do not have any definite length value and also no critical concentration of solution below which aggregates do not form. This feature distinguishes LCLCs from traditional lyotropic surfactant systems which are characterized by critical micellar concentration (CMC), the threshold concentration below which mesophases cannot

be formed. The average size and organization of aggregates in the solution significantly depend on factors like concentration, temperature, and ionic additives. As the concentration of LCLC increases, the aggregates multiply, elongate, and align parallel to each other and then form mesophases. A unit vector \hat{n} with a property $\hat{n} \equiv -\hat{n}$ can be used to represent the average orientation of these aggregates, which is generally called the director shown in Fig. 1.10. At higher concentrations, the aggregates can form orientationally ordered uniaxial nematic (N) phase (Fig. 1.10(a)) and the positionally ordered columnar (C or M) phase (Fig. 1.10(b)) [94]. The labels N and M were assigned based on early polarized optical microscopy (POM) studies on DSCG. The N phase of DSCG exhibits Schlieren texture resembling the characteristic patterns seen in thermotropic nematics, while the M phase of DSCG displays an optical texture similar to that of the hexagonal H1 soap phase [111, 112].

Among the captivating family of LCLC compounds, the aqueous solutions of chromonic materials disodium cromoglycate (DSCG) and Sunset Yellow (SSY) emerge as promising candidates. While DSCG has received considerable research attention, the potential of SSY remains relatively underexplored. As an underexplored chromonic compound, SSY has been chosen as one of the focal subjects of this thesis.

1.2.2 Sunset Yellow chromonics

The compound disodium salt of 6-hydroxy-5-[(4-sulfophenyl) azo]-2-naphthalenesulfonic acid is commonly called Sunset Yellow (SSY). SSY is a synthetic azo dye belonging to the class of azo chromophores, extensively used as a food colorant [103,117]. As a food dye, SSY is available in a much purer form than other textile dyes. Due to its extensive applications in food and beverage products, SSY has emerged as the second most studied LCLC after DSCG.

Figure 1.11 depicts the molecular structure of SSY in (i) OH form and (ii) NH form. According to Park *et al.* and Chami and Wilson, the OH azo tautomer of SSY is considered a

$$(a) \qquad (b) \qquad H \qquad H \qquad H \qquad SO_3Na \qquad SO_3Na \qquad H$$

Fig. 1.11. Molecular structure of Sunset Yellow (SSY) compound in (a) azo form and (b) hydrozone form.

planar and disk-like molecule due to the presence of the N=N double bond. In contrast, the NH hydrazone tautomer of SSY shows a flexible chain at the N-N binding site [118,119]. However, when the molecule is in water, both of these tautomers are expected to form aggregates to reduce water exposure to their hydrophobic aromatic rings. In water, the hydrophobic centers stack on top of each other via non covalent $\pi - \pi$ interactions, thus forming cylindrical aggregates with a stacking separation of ~ 0.34 nm [97,99,119,121-123]. The aggregates have a diameter of ~ 1 nm. The positive ions (Na^+) at the periphery of the molecules dissociate in water, producing charged aggregates with a maximum charge density, $\chi_{max} \sim 6e/\text{nm}$ (e denotes the electron's charge) [119,121]. In 2008, Park et al reported the existence of liquid crystalline phases such as the nematic (N) and columnar (C) phases in aqueous solutions of SSY [119]. The phase diagram of the aqueous solution of SSY adapted from A. Yamaguchi [124] is shown in Fig. 1.12(a). The schlieren texture observed in the nematic phase (32 wt % solution) under polarizing optical microscope (POM) is shown in Fig. 1.12(b)

SSY has been the subject of intensive investigations due to its diverse and wide range of applications. The pioneering work of Horowitz *et al.* in 2005 [103] reported the X-ray diffraction and optical absorption measurements on aqueous solutions of SSY, revealing that

aggregation occurs at all concentrations, with the aggregation number increasing with concentration. These studies were continued by Edwards *et al.* in 2008 [104], who reported optical microscopy, X-ray diffraction and multinuclear NMR studies on the aqueous solution

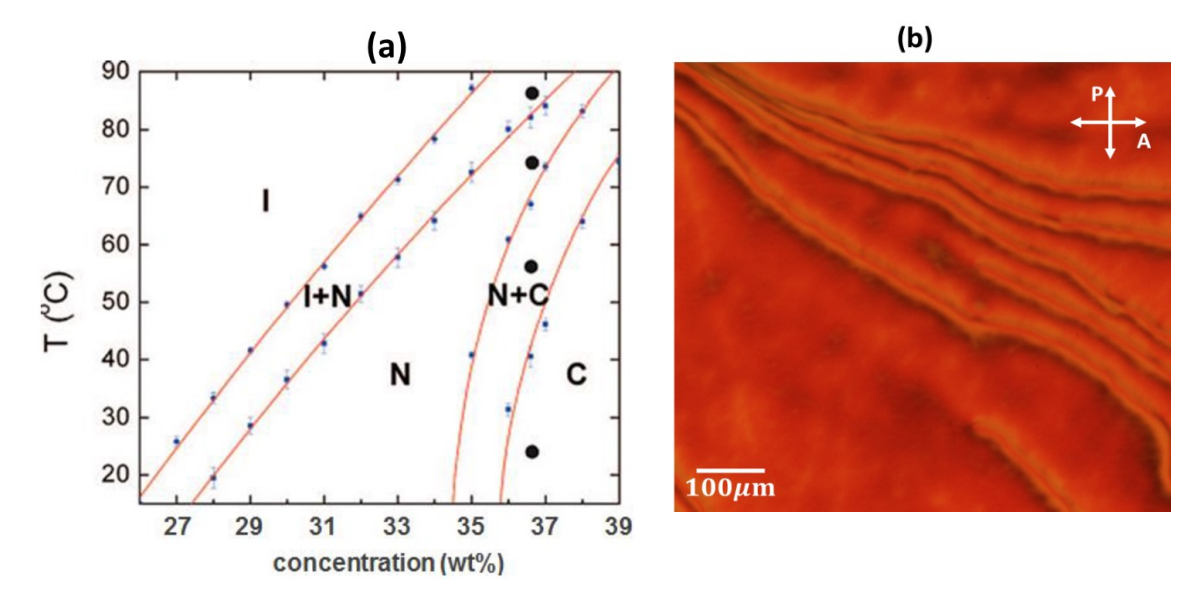


Fig. 1.12.(a) Phase Diagram of SSY adapted from A. Yamaguchi [124]. The LC phase of SSY depends on the concentration (wt%) and temperature (°C). Isotropic-nematic coexistence and nematic-columnar coexistence phases are represented by I+N and N+C respectively. **(b)** Schlieren texture observed in the nematic phase of SSY LC (32 wt % solution) under POM.

and LC phases of SSY. The optical textures observed were nearly similar to those of aqueous solution of DSCG, and the phase diagram exhibited a similar multi-peritectic form. The prominent features of the X-ray diffraction patterns of the mesophases of SSY LC and DSCG LC show similarities [97].

To gain a more profound understanding of the structure of the aggregates and LCLC phases of SSY, Joshi *et al.* conducted a study investigating the effect of changes in dye concentration, temperature and ionic additives using X-ray diffraction and POM techniques [125]. They reported that the aggregation process in SSY LCLC is non-isodesmic according to the concentration and temperature dependence of the scission energy [105]. Luoma *et al.* investigated the growth of SSY stacks in the aqueous medium using X-ray scattering and magnetic birefringence [126]. In 2007, Prasad *et al.* [127] performed comprehensive studies involving x-ray, rheological and dielectric investigations on SSY LCLC with and without the

addition of salt. The authors observed a non-monotonic variation in the steady-state viscosity at low shear rates, which was found to be qualitatively similar to the behavior observed in worm-like micellar systems. This result is surprising because the chromonic systems are typically considered to have non-micellar characteristics. In 2008, Park et al. [119] also investigated the influence of salts on SSY chromonics. Their studies revealed two distinct trends: (a) the addition of mono and divalent salts led to the stabilization of the N phase, and (b) an increase in pH resulted in the suppression of the N phase. X-ray measurements indicated that the correlation length associated with the stacking was too short to explain the orientational order based on the Onsager model. To account for this, the authors proposed more complex aggregate structures containing "stacking faults," such as junctions with a shift of neighboring molecules and three-fold junctions, based on DLS measurements, which showed that the aggregates were larger than the correlation length. The atomic simulation study of Chami and Wilson's [118] demonstrated head-to-tail stacking preference and antiparallel dipole order of SSY molecules. These stacked structures were found to be dynamic entities capable of rotational transitions (flips) between antiparallel and parallel configurations. Renshaw and Day [128] studied the hydrodynamic behavior of Sunset Yellow aggregates in isotropic solution by employing diffusion nuclear magnetic resonance (NMR) methods. Their results revealed that the aggregates comprised of tens to hundreds of monomer units at the examined concentrations. Also, the average number of molecules per aggregate was calculated to be approximately 5 larger than previously reported [128]. Jones et al. [129] studied the aggregate formation in SSY solution by employing changes in the 1H NMR chemical shifts. The authors observed that low salinity levels in SSY concentrations led to alterations in the size and shape of the aggregates, causing aggregation/disaggregation effects occurring over four orders of magnitude of added electrolyte. Park et al. [121] investigated the condensation behavior of SSY in aqueous solutions containing polyethylene glycol (PEG)

and doped with NaCl salt, using various measurements techniques including optical and fluorescence microscopy, cryo-transmission electron microscopy (cryo-TEM), spectroscopy, densitometry and synchrotron X-ray scattering. The presence of PEG induces the condensation of isotropic SSY solutions, resulting in the formation of a liquid crystalline region. Additionally, PEG causes the separation of the nematic (N) phase into coexisting N and isotropic (I) domains or the coexistence of the columnar hexagonal (C) phase and the isotropic (I) phase. This observation was qualitatively explained by the depletion (excluded volume) effects and suggests that salt-induced screening of electric charges at the surface of chromonic aggregates results in two distinct effects: (a) an increase in the scission energy and contour length of the aggregates, and (b) a decrease in the persistence length of SSY aggregates [121].

Although SSY has been extensively studied for its optical and structural properties, the realm of rheological characterization remains relatively unexplored except some basic rheological studies mostly focusing on the shear rate dependent viscosity [126]. Rheological studies on Sunset Yellow are of great significance in the food and beverage industries as they provide crucial insights into the flow behavior and mechanical properties of SSY-containing products. Understanding the rheological characteristics of SSY is essential for optimizing formulations, enhancing product stability, and controlling textural attributes. These studies enable manufacturers to tailor the viscosity, shear-thinning behavior, and gelation properties of SSY based food and beverage products. Apart from this industrial importance, the unique aggregation behavior and molecular organization of SSY in solution make it a compelling subject for fundamental rheological investigations.

1.3 Motivation

The dense glass state of PNIPAM microgel suspension shows viscoelastic behavior. In dense suspensions, the core-shell morphology of the PNIPAM microgel spheres is expected

to influence their dynamics. DLS studies by Eckert *et al.* [130] on dense liquid-like ordered PNIPAM microgel suspensions reveal that the dynamics of the microgel particles are affected by their core-shell structure. Recently, Joshi *et al.* [70] reported short time sub-diffusive behavior in the dense solid (disordered glass) state of PNIPAM microgel particles, which is claimed to be due to the entanglements of dangling polymer chains between neighboring particles. Though there exist recent rheological studies on the yielding behavior of dense PNIPAM microgel suspensions by Joshi *et al.* [70] and Jathavedan *et al.* [131], a comprehensive investigation is still absent to confirm the role of entanglements of dangling polymer chains in the dense state of PNIPAM microgel suspension. To understand the role of entanglements, we prepared dense glass samples of PNIPAM microgel particles (i) with dangling polymer chains (core-shell (CS) PNIPAM microgel particles) (ii) without dangling polymer chains (homogeneous core (HC) PNIPAM microgel particles). We study the yielding behavior of these glass samples by Large Amplitude Oscillatory (LAOS) measurements and the results are described in Chapter 3.

Lyotropic micellar systems are widely investigated for their flow behavior under shear [132-135], whereas, the flow behavior of lyotropic chromonic systems is less explored. Chromonic materials exhibit LC phases when dissolved in a solvent, particularly in water called Lyotropic Chromonic Liquid Crystals (LCLCs). Sunset Yellow is a highly demanded chromonic material, a food colorant that forms LC phases when dissolved in water. The rheological response of SSY nematics is not well studied except for some basic shear rate dependent viscosity measurements [127]. Recently, Baza *et al.* [136] studied the shear-induced structure of the nematic phase of lyotropic chromonic liquid crystal of disodium cromoglycate (DSCG) in detail. Using various experimental techniques, they correlated shear-induced microstructure and the director orientation as a function of shear rate and provided insightful information. A systematic investigation of the rheological properties,

especially the shear-induced microstructures and dynamics of the nematic phase of SSY liquid crystal, is absent. Towards this study, we prepare a nematic sample of SSY LC. The flow behavior is studied for a range of shear rates. The results are interpreted with the help of *insitu* rheo-microscopic images in Chapter 4.

Nearly monodisperse PNIPAM microgel spheres have been synthesized for carrying out rheological studies in microgel colloidal glass which constitutes an isotropic soft matter system. Additionally, to investigate the shear response in an anisotropic soft matter system, we have chosen the liquid crystal system of SSY in water and the rheological measurements were carried out in the nematic phase. The thesis is structured in the following way. The details, including the synthesis of PNIPAM microgel particles with different morphology and characterization, preparation of both isotropic microgel glass samples and anisotropic liquid crystal samples of SSY/water solutions, are discussed in Chapter 2. Chapter 3 describes the investigations on dynamics and yielding behavior of dense PNIPAM microgel glasses. The flow behavior of SSY LC is discussed in Chapter 4. Chapter 5 discusses the summary and conclusions of the investigations that are carried out using light scattering techniques and rheology, key findings of the thesis and directions for future work.

References

- 1. W. Poon, Colloids as Big Atoms, Science, **304**, 830 (2004)
- 2. J. C. Brown, P. N. Pusey, J. W. Goodwin and R. H. Ottewill, J. Phys. A:Math.Gen., 8, 664 (1975).
- 3. P. N. Pusey, Phil. Trans. R. Soc., **A293**, 429 (1979)
- 4. A. K. Sood, Hyperfine Interactions., **37**, 365 (1987)
- R. Kesavamoorthy, B. V. R. Tata, A. K. Arora and A. K. Sood, Physics Letters A.,138, 208 (1989)

- 6. T. Yoshiyama and I. S. Sogami in *Ordering and Phase Transitions in Charged Colloids*, Eds. A. K. Arora and B. V. R. Tata, **Ch. 3**, VCH Publishers, New York (1996)
- U. Gasser, E. R. Weeks, A. Schofield, P. N. Pusey, D. A. Weitz, Science., 292, 258 (2001).
- 8. P. N. Pusey and W. van Megen, Phys. Rev. Lett., **59**, 2083 (1987)
- 9. W. Härtl, H. Versmold and X. Zhang-Heider, J. Chem. Phys., 102, 6613 (1995)
- 10. B.V.R. Tata and S.S. Jena, Solid State Commun. 139, 562 (2006).
- 11. R. S. Crandall and R. Williams, Science 198, 293 (1977).
- 12. R. Williams, R.S. Crandall and P.J. Wojtowicz, Phys. Rev. Lett. 37, 348 (1976).
- 13. J. C. Zahorchak, R. Kesavamoorthy, R. D. Coalson and S. A. Asher, J. Chem. Phys. 96, 6873 (1992)
- 14. Ke-Qin Zhang and X. Y. Liu, Nature **429**, 739 (2004).
- 15. Cacciuto, S. Auer and D. Frenkel, Nature, 428, 404 (2004).
- 16. P. Schall, I. Cohen, D. A. Weitz and F. Spaepen, Nature, 389, 319 (2006).
- 17. J. K. G. Dhont, C. Smits and H. N. W. Lekkerkerker, J. Colloid Interf. Sci. 152, 386 (1992).
- 18. W. van Megen and S. M. Underwood, Phys. Rev. E, 49, 4206 (1994).
- 19. E. R. Weeks, J. C. Crocker, A. C. Levitt, A. Schofield, D. A. Weitz, Science 287,627 (2000).
- 20. B. V. R. Tata, P. S. Mohanty and M. C. Valsakumar, Phys. Rev. Lett. 88, 018302 (2002).
- 21. Peter Schall, Itai Cohen, David A. Weitz, Frans Spaepen, Science 305, 1944 (2004).
- 22. H. K. Nagamanasa, S. Gokhale, R. Ganapathy, and A. K. Sood, PNAS, **108**, 11323 (2011).
- 23. P. Schall, D. A. Weitz, F. Spaepen, Science, 318, 1895 (2007).

- 24. J. Mattsson, H. M. Wyss, A. Fernandez-Nieves, K. Miyazaki, Z. Hu, D. R. Reichman and D. A. Weitz, Nature 462, 83 (2009).
- 25. J. H. Holtz and S. A. Asher, Nature 389, 829 (1997).
- 26. C. Geary, I. Zudans, A. Goponenko, S. Asher, S. Weber, Analytical Chemistry 77, 185 (2005).
- 27. J. M. Weissman, H. B. Sunkara, A. S. Tse, and S. A. Asher, Science **274**, 959 (1996).
- 28. P. L. Flaugh, S. E. O'Donnell, and S. A. Asher, Appl. Spectrosc. 38, 847 (1984).
- 29. G. Pan, R. Kesavamoorthy, S. A. Asher, Phys. Rev. Lett. 78, 3860 (1999).
- 30. C. E. Reese, A. V. Mikhonin, M. Kamenjicki, A. Tikhonov and S. A. Asher, J.Am. Chem. Soc. 126, 1493 (2004).
- 31. S. Hyun Kim, S. Yeon Lee, S. Man Yang and Gi-Ra Yi, NPG Asia Mater. 3, 25 (2011).
- 32. C. W. Macosko, Rheology Principles Measurements and Applications, WILEYVCH, New York (1994); T. A. Mazder, Rheology Handbook, Vincentz Network GmbH & Co, K.G.
- 33. P.N. Pusey and W. van Megen, Nature 320, 340 (1986).
- 34. L. V. Woodcock, Nature, **385**, **141** (1997).
- 35. P. G. Bolhuis, D. Frenkel, Siun-Chuon Mau, D. A, Nature 388, 235 (1997).
- 36. P. N. Pusey, W. van Megen, P. Bartlett, B. J. Ackerson, J. G. Rarity, and S. M. Underwood, Phys. Rev. Lett. **63**, 2753 (1989).
- 37. I. P. Dolbnya, A. V. Petukhov, D. G. A. L. Aarts, G. J. Vroege, and H. N. W.Lekkerkerker, EPL (Europhysics Letters) 113, 962 (2005).
- 38. S. Pronk and D. Frenkel, The Journal of Chemical Physics 110, 4589 (1999).
- 39. S. I. Henderson, T. C. Mortensen, S. M. Underwood, W. van Megen, Physica A 233, 102 (1996).
- 40. E. J. W. Verwey, The Journal of Physical and Colloid Chemistry 51, 631 (1947).

- 41. B. V. Derjaguin and L. D. Landau, Zh. Eksp. Teor. Fiz 15, 663 (1945).
- 42. B. V. R. Tata, in *Statistical physics of complex fluids*, edited by Shigenao Maruyama, and Michio Tokuyama (Tohoku University, Sendai, Japan, 2007).
- 43. E. B. Sirota. H. D. Ou-Yang, S K. Sinha, P. M. Chaikin, J. D. Axe and Y. Fujii, Phys. Rev. Lett. **62**, 1524 (1989).
- 44. B. V. R. Tata, Current science **80**, 948 (2001).
- 45. R. Acciaro, T. Gilanyi, and I. Varga, Langmuir 27, 7917 (2011).
- 46. B. Sierra-Martin, J. R. Retama, M. Laurenti, A. Fernández Barbero, and E. López Cabarcos, Advances in Colloid and Interface Science **205**, 113 (2014).
- 47. Y. Guan and Y. Zhang, Soft matter 7, 6375 (2011).
- 48. H. Senff, and W. Richtering, J. Chem. Phys. 111, 1705 (1999).
- 49. A. Fernández-Nieves, A. Fernández-Barbero, B. Vincent, and F. De Las Nieves, Macromol. 33, 2114 (2000).
- 50. K. Kratz, T. Hellweg, and W. Eimer, Polymer **42**, 6631 (2001).
- 51. M. Rasmusson, A. Routh, and B. Vincent, Langmuir 20, 3536 (2004).
- 52. J. Brijitta, B. V. R. Tata and T. Kaliyappan, J. Nanosci. Nanotechnology 9, 5323 (2009).
- 53. C. D. Jones and L. Andrew Lyon, Macromolecules 33, 8301 (2000).
- 54. Li-Yi Chen, Chung-Mao Ou, Wei-Yu Chen, Chih-Ching Huang, and Huan-Tsung Chang, Appl. Mater. Interfaces 5, 4383 (2013).
- 55. Q. Luo, Y. Guan, Y. Zhang, M. Siddiq, Journal of Polymer Science: Part A: Polymer Chemistry 48, 4120 (2010).
- 56. S. V. Vinogradov, Curr Pharm Des. 12, 4703 (2006).
- 57. M. Ballauff, Y. Lu, Polymer 48, 1815 (2007).
- 58. J. Wu, B. Zhou and Z. Hu, Phys. Rev. Lett. **90**, 048304(2003).
- 59. E. C. Cho, J. Lee, and K. Cho, Macromolecules 36, 9929 (2003).

- 60. A. van Blaaderen, J. Peetermans, G. Mat-et and J. K. G. Dhont, J. Chem. Phys. 96, 4591 (1992).
- 61. T. Eckert and E. Bartsch, Phys. Rev. Lett. 89, 125701 (2002).
- 62. E. Zaccarellia and W.C. K. Poon, PNAS, (2009).
- 63. B. R. Saunders, Langmuir **20**, 3925 (2004).
- 64. J. Gao and B. J. Frisken, Langmuir 19, 5217 (2003).
- 65. I. Varga, T. Gilányi, R. Mészáros, G. Filipcsei, and M. Zrínyi, The Journal of Physical Chemistry B **105**, 9071 (2001).
- 66. M. Stieger, W. Richtering, J. S. Pedersen, and P. Lindner, The Journal of Chemical Physics **120**, 6197 (2004).
- 67. M. H. Kwok, Z. Li, T. Ngai, Langmuir 29, 9581 (2013).
- 68. T. Hellweg, C. D. Dewhurst, E. Brückner, K. Kratz, and W. Eimer, Colloid and Polymer Science **278**, 972 (2000).
- 69. A. Frenendaz-nieves, A. Fernández Barbero, B. Vincent, and F. J. de las Nives, J. Chem. Phys. 119, 10383 (2003).
- 70. R. G. Joshi, B. V. R. Tata, Colloid Polym. Sci. 295, 1671 (2017).
- 71. W. G. Hoover, S. G. Gray, and K. W. Johnson, The Journal of Chemical Physics 55, 1128 (1971).
- 72. R. Agrawal and D. A. Kofke, Molecular Physics 85, 23 (1995).
- 73. M. J. Bergman, N. Gnan, M. Obiols-Rabasa, J.M. Meijer, L. Rovigatti, E. Zaccarelli, P. Schurtenberger, Nat. Commun. 9, 5039 (2018).
- 74. R. Kimmich, *Principles of Soft-Matter Dynamics: Basic Theories, Noninvasive Methods, Mesoscopic Aspects* (Springer, Netherlands, 2012).
- 75. R. G. Joshi, B. V. R. Tata, and J. Brijitta, J. Chem. Phys. 139, 124901 (2013).
- 76. M. Medina-Noyola, Phys. Rev. Lett. **60**, 2705 (1988).

- 77. H. P. Rønningsen, Annual Transactions of the Nordic Rheology Society, 20, 11 (2012).
- 78. F. Souas, A. Safri, and A. Benmounah, Petroleum Research, 6, 116 (2021).
- 79. P. Fischer, and E. J. Windhab, Current Opinion in Colloid & Interface Science, **16**, 36 (2011).
- 80. R. Lambourne, and T. A. Strivens, *Paint and surface coatings: theory and practice* (second edition), Woodhead publishing Ltd., Cambridge (1999).
- 81. N. V. K. Dutt, and D. H. L. Prasad, Pigment & resin technology, 14, 10 (1985).
- 82. K. Miyazaki, H. M. Wyss, D. A. Weitz, and D. R. Reichman, Europhys. Lett. 75, 915 (2006).
- 83. G. Petekidis, A. Moussaïd and P. N. Pusey, Phys. Rev. E 66, 051402 (2002).
- 84. P. Sollich, Phys. Rev. E 58, 738 (1998).
- 85. P. Sollich, F. Lequeux, P. Hébraud, and M. E. Cates, Phys. Rev. Lett. 78, 2020 (1997).
- 86. H. M. Wyss, K. Miyazaki, J. Mattsson, Z. Hu, D. R. Reichman and D. A. Weitz, Phys. Rev. Lett. **98**, 238303 (2007).
- 87. K. N. Pham, G. Petekidis, D. Vlassopoulos, S. U. Egelhaaf, P. N. Pusey and W. C. K. Poon Europhys. Lett. **75**, 624 (2006)
- 88. P. G. de Gennes and J. Prost. *The physics of liquid crystals*. International series of monographs on physics, Clarendon Press, 1993.
- 89. S. Chandrasekhar. Liquid Crystals. Cambridge University Press, 1992.
- 90. S. Kumar, "Experimental Study of Physical Properties and Phase Transitions", Cambridge University Press, New York, NY (2001).
- 91. P. Oswald and P. Pieranski, "Nematic and cholesteric Liquid Crystals", CRC press, Taylor & Francis, Boca Raton, FL (2005).
- 92. H. S. Park, "Self-assembly of lyotropic chromonic liquid crystals: Effects of additives and applications", Doctoral dissertation, Kent State University, (2010)

- 93. P. J. Collings and Michael Hird, "Introduction to Liquid Crystals", Taylor & Francis, New York, NY (1997).
- 94. J. Lydon, Curr. Opin. Colloid Interface Sci. 3, 458 (1998).
- 95. T. K. Attwood, J. E. Lydon, F. Jones, F., Liq. Cryst. 1, 499 (1986).
- 96. T. K. Attwood, J. E. Lydon, C. Hall, G. J. T. Tiddy, Liq. Cryst., 7, 657 (1990).
- 97. J. Lydon, Liq. Cryst., 38, 1663 (2011).
- 98. J. Lydon, J. Mater. Chem., 20, 10071 (2010).
- 99. P. J. Collings, A. J. Dickinson and E. C. Smith, Liq. Cryst., 37, 701 (2010)
- 100. J. Lydon, Current opinion in colloid & interface science, 8, 480 (2004).
- 101. A. S. Vasilevskaya, E. V. Generalova, and A. S. Sonin, Russian Chemical Reviews 57, 1575 (1989), (Translated from Uspekhi Khimii, 58, 1575 (1989))
- 102. L. J. Yu, A. Saupe, Mol. Cryst. Liq. Cryst. 80, 129 (1982).
- 103. V. R. Horowitz, L. A. Janowitz, A. L. Modic, P. A. Heiney, P. J. Collings, Phys. Rev. E 72, 041710 (2005).
- D. J. Edwards, J. W. Jones, O. Lozman, A. P. Ormerod, M. Sintyureva, G. J. T. Tiddy,
 J. Phys. Chem. B 112, 14628 (2008).
- 105. L. Joshi, S. W. Kang, D. M. Agra-Kooijman, S. Kumar, Phys. Rev. E 80, 041703 (2009).
- 106. G. J. T. Tiddy, D. L. Mateer, A. P. Ormerod, W. J. Harrison, D. J. Edwards, Langmuir 11, 390 (1995).
- S. W. Tam-Change, W. Seo, I. K. Iverson, S. M. Casey, Angew. Chem., Int. Ed. 42, 897 (2003).
- 108. S. W. Tam-Change, J. Helbley, I. K. Iverson. Langmuir 24, 2133 (2008).
- 109. L. Spindler, I. Drevensek-Olenik, M. Copic, R. Romih, J. Cerar, J. Skerjanc, P. Mariani, Eur. Phys. J. E 7, 95 (2002).

- 110. P. Mariani, F. Spinozzi, F. Federiconi, H. Amenitsch, L. Spindler, I. Drevensek Olenik, J. Phys. Chem. B **113**, 7934 (2009).
- 111. J. S. Cox, G. D. Woodard, and W. C. McCrone, Journal of pharmaceutical sciences 60, 1458 (1971).
- 112. N. H. Hartshorne, and G. D. Woodard, Molecular Crystals and Liquid Crystals 23, 343 (1973).
- 113. D. J. Edwards, A. P. Ormerod, G. J. T. Tiddy, A. A. Jaber, A. Mahendrasingham, Aggregation and lyotropic liquid crystal formation of anionic azo dyes for textile fibres. In *Physico-Chemical Principles of Colour Chemistry*; Peters, A. T., Freeman, H. S., Eds.; Advances in color chemistry series (Springer-Verlag: New York, 1996).
- 114. S. W. Tam-Chang, L. Huang, Chem. Commun., 17, 1957 (2008).
- 115. Yu. A. Nastishin, H. Liu, T. Schneider, V. Nazarenko, R. Vasyuta, S. V. Shiyanovskii,O. D. Lavrentovich, Phys. Rev. E 72, 041711 (2005).
- 116. A.J. Dickinson, N. D. LaRacuente, C. B. Mckitterick, P. J. Collings, Mol. Cryst. Liq. Cryst., **509**, 9 (2009).
- 117. N. Zimmermann, Soft Matter 11, 1547 (2015).
- 118. F. Chami and M. R. Wilson, J. Am. Chem. Soc. 132, 7794 (2010).
- 119. H. S. Park, S. W. Kang, L. Tortora, Y. Nastishin, D. Finotello, S. Kumar, and O. D. Lavrentovich, J. Phys. Chem. B **112**, 16307 (2008).
- V. G. Nazarenko, O. P. Boiko, M. I. Anisimov, A. K. Kadashchuk, Y. A. Nastishin,
 A. B. Golovin and O. D. Lavrentovich, Appl. Phys. Lett., 97, 284 (2010).
- 121. H. S. Park, S. W. Kang, L. Tortora, S. Kumar and O. D. Lavrentovich, Langmuir, 27, 4164 (2011).
- 122. T. Suzuki and Y. Kojima, Mol. Cryst. Liq. Cryst. 648, 162 (2017).

- 123. C. Ruslim, D. Matsunaga, M. Hashimoto, T. Tamaki and K. Ichimura, Langmuir, 19, 3686 (2003).
- 124. A. Yamaguchi, "Self-assembly of lyotropic chromonic liquid crystal mixtures", *Condensed Matter Physics Commons.*, University of Colorado, Boulder (2015)
- 125. L. P. Joshi, "X-ray study of mesomorphism of bent-core and chromonic mesogens", Ph.D. thesis, Kent State University (2009).
- 126. R. J. Luoma, "X ray scattering and magnetic birefringence studies of aqueous solutions of chromonic molecular aggregates", Ph.D. thesis, Brandeis Univ. (1995).
- S. K. Prasad, G. G. Nair, G. Hegde, and V. Jayalakshmi, J. Phys. Chem. B 111,9741 (2007).
- 128. M. P. Renshaw, and I. J. Day, J. Phys. Chem. B 114, 10032 (2010).
- 129. J. W. Jones, L. Lue, A. P. Ormerod, and G. J. T. Tiddy, Liquid Crystals 37, 711 (2010).
- 130. T. Eckert and W. Richtering, J.Chem. Phys. 129, 124902 (2008).
- 131. K. K. Jathavedan, F. Kanheerampockil, S. Bhat, J Appl. Polym. Sci. 137, 48625 (2020).
- 132. R. Bandyopadhyay, G. Basappa and A. K. Sood, Phys. Rev. Lett., 84(9), 2022 (2000).
- 133. A. K. Sood and R. Ganapathy, Pramana, 67, 33 (2006).
- 134. R. Ganapathy and A. K. Sood, Langmuir, 22, 11016 (2006).
- 135. R. Ganapathy and A. K. Sood, Phys. Rev. Lett. **96**, 108301(2006).
- 136. H. Baza, T. Turiv, B. X. Li, R. Li, B. M. Yavitt, M. Fukuto and O. D. Lavrentovich, Soft Matter, 16, 8565 (2020).

SYNTHESIS METHOD AND EXPERIMENTAL TECHNIQUES

This chapter discusses the synthesis and characterization of two types of soft matter systems i) dense PNIPAM microgel suspensions and ii) SSY liquid crystals for their rheological phase behaviour under external stress. The theory and practical of experimental techniques used for characterizing the phase behaviour of dense PNIPAM microgel suspension and lyotropic SSY liquid crystal is described. Aqueous suspensions of PNIPAM microgels were synthesized by free radical precipitation polymerization with two different morphologies (i) core-shell structure with dangling polymer chains (ii) homogeneous core with uniform polymer density. Detailed method of synthesis and dense PNIPAM microgel sample preparations are described. Further, the preparation of SSY liquid crystal sample and its phase confirmation is discussed in detail. The rest of the chapter presents various experimental methods used to probe the dynamics and rheological behavior of the above mentioned soft matter systems. Details of dynamic light scattering (DLS), three dimensional (3D) dynamic light scattering (3D-DLS), polarizing optical microscopy (POM), UV visible spectroscopy and rheology are presented.

2.1 PNIPAM microgel suspensions

2.1.1 Synthesis of core-shell PNIPAM microgel particles by batch method

he batch synthesis of PNIPAM microgels is based on the one pot method developed by Wu *et al.* [1] and adopted by several researchers [2,3] in order to

synthesise core-shell PNIPAM (CS-PNIPAM) microgel particles. We have used the batch method to synthesize nearly monodisperse core-shell PNIPAM microgel particles. The synthesis method is depicted in Fig. 2.1. The monomer solution was prepared by dissolving N-isopropylacrylamide (NIPAM) monomer and N, N'-methylene-bis-acrylamide (BIS) cross linking agent in 250 mL of ultra-pure Milli-Q water (conductivity $\sim 0.8\,\mu\text{S/cm}$). Sodium dodecyl sulfate (SDS) was then dissolved in this monomer solution as a surfactant to control the particle size. SDS generates spherical micelles in aqueous solution above the critical micelle concentration (CMC), which contain monomer units and act as monomer droplets. By changing the concentration of surfactant, the size of the microgel spheres can be adjusted [4]. The concentration of SDS influences the size of the micelle generated, thus the size of the microgel particle [4]. The monomer solution was then filtered to remove any aggregates and dust using a 0.2 μ m syringe filter and transferred into a 250 mL three necked glass reactor. The solution was then heated to 70°C under vigorous stirring and application of gentle Ar gas flow to prevent the inflow of oxygen. To initiate the polymerization, 5 mL of potassium

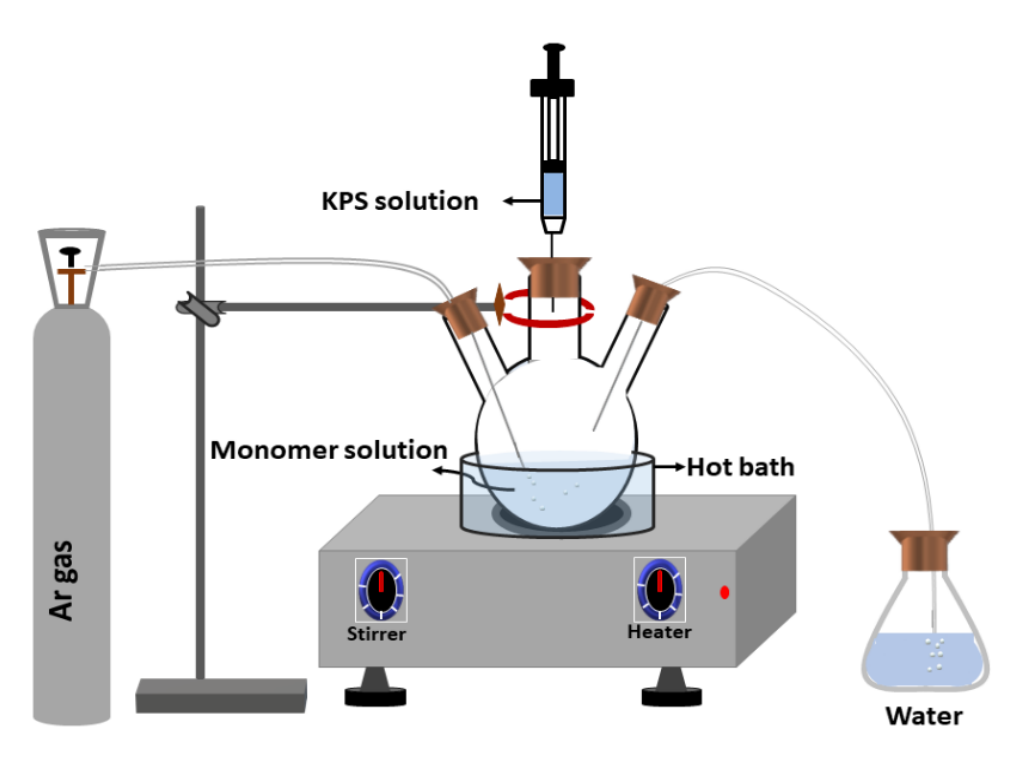


Fig. 2.1. Schematic representation of the experimental set-up used for the synthesis of CS-PNIPAM microgel particles by batch method

persulphate (KPS) was injected in to the monomer solution. At 70°C, KPS dissociates to produce free radicals, which initiate the polymerization reaction. Within a few minutes after injecting the initiator, the reaction mixture turns translucent, indicating the production of precursor particles. Precursor particles are produced when the expanding chain attains a threshold length. These precursor particles grow by adding to each other. During polymerization, the cross-linker BIS connects the polymer chains, resulting in a network structure of microgel particles. The polymerization is allowed to continue for 6 hours while maintaining all the reaction conditions. After 6 hours, the turbid colloidal suspension of PNIPAM microgel was brought to room temperature to stop the polymerization. The concentration of chemical reagents used for the synthesis of PNIPAM microgel particles with core-shell structure are summarized in Table 2.1.

Label	NIPAM (mM)	BIS (mM)	SDS (mM)	KPS (mM)
CS-PNIPAM	139	1.96	1.05	2.22

Table 2.1. Details of the chemical reagents used in the conventional synthesis of core-shell (CS) PNIPAM microgel particles

2.1.2 Synthesis of homogeneous core PNIPAM microgel particles by semibatch method

We have synthesised PNIPAM microgel spheres with a homogeneous core (HC-PNIPAM) in aqueous medium using a semi-batch method [5]. This approach is proposed by Accario *et al.* [6] further used by Kwok *et al.* [5] and Jathavedan *et al.* [7]. A schematic view of the experimental setup is depicted in Fig. 2.2. This synthesis comprises of two stages. In the first stage, the NIPAM monomer was dissolved in 55 ml Milli-Q water to prepare the monomer solution. This monomer solution was then transferred into the three necked glass

reactor through a $0.2 \mu m$ syringe filter. Meanwhile, the feed solution was prepared in a separate two necked round bottom flask by dissolving NIPAM monomer and BIS cross linker in 6mL Milli-Q water which was then degassed for half an hour. The monomer solution was then placed on an oil bath whose temperature is set at 70° C. Ar gas purging is maintained in the solution with intense stirring (1000 rpm). Polymerization was initiated soon after the addition of 1 mL KPS solution which was prepared in Milli-Q water into the monomer solution. The second stage was initiated four minutes after the initiation of the polymerization by feeding the 6 mL of monomer solution (homogeneous mixture of NIPAM monomer and BIS cross linker) at a rate of $100 \,\mu$ L/min using a micro pipette. After completing the feeding process, the polymerization was terminated and the resultant turbid PNIPAM microgel suspension was quickly brought down to room temperature by immersing the three necked flask containing the suspension in an ice bath. The experimental verification of uniform polymer density in the

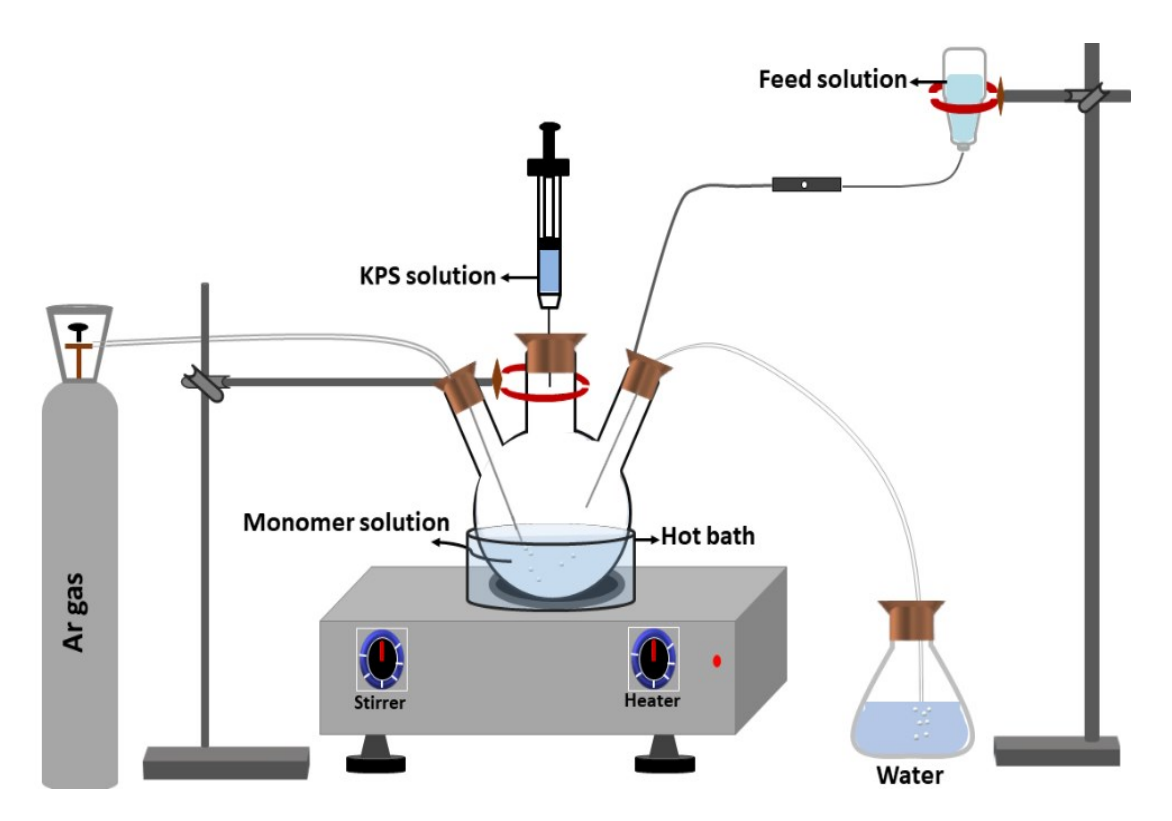


Fig. 2.2. Schematic representation of the experimental set-up used for the synthesis of HC-PNIPAM microgel particles by semi-batch method

PNIPAM microgel spheres synthesized by the semi-batch method was reported by Accario *et al.* from the optical properties of PNIPAM microgel latex [6] and Jathavedan *et al.* from cryo-TEM experiments [7]. Since previous studies have revealed the homogenous core structure of PNIPAM microgel particles, we did not verify the homogeneous polymer distribution in the HC-PNIPAM particles reported here. As we followed the identical procedure reported by Accario *et al.* and Jathavedan *et al.*, we assume that the PNIPAM particles are homogeneous in nature. Later we show in chapter 3 that they behave differently from the CS-PNIPAM sphere. The concentration used for the synthesis of homogeneous core PNIPAM microgel particles are summarized in Table 2.2.

Label	NIPAM (Mm)		BIS (mM)		KPS (mM)	
HC-PNIPAM	Reactor	Feed	Reactor	Feed	Reactor	Feed
	144.61	441.85		34.6	3.7	

Table 2.2. Details of the chemical reagents used in the semi-batch synthesis of homogeneous core (HC) PNIPAM microgel particles.

2.1.3 Purification PNIPAM microgel suspensions

The purification of PNIPAM microgel suspensions to remove unreacted monomers, we have carried out dialysis of synthesized suspension using cellulose tubing's (Sigma Aldrich) with a molecular weight cut off 14,000 g/mol against Millipore water (conductivity 0.8 μ S/cm) for 2 weeks until the conductivity of dialyzed water goes below 1μ S/cm. The purified PNIPAM microgel suspensions are left in contact with mixed bed of ion exchange resins (AmberLite® MB20, Sigma Aldrich) for further removal of ionic impurities.

2.1.4 Preparation of dense PNIPAM microgel samples

Dynamic light scattering (DLS) measurements on dilute samples of core-shell and homogeneous core PNIPAM microgel suspensions were performed using a particle size analyzer (M/s Anton Paar GmbH, Germany) equipped with a laser source of operating at a wavelength of 658 nm to characterise the purified microgel suspensions for their size and size polydispersity. The DLS data were analyzed with KalliopeTM software. Table 2.3 displays the measured average hydrodynamic diameter, d_h , the size polydispersity (SPD) and volume fraction, ϕ . The theory of DLS technique and analysis of intensity- intensity auto correlation function measured using DLS is described later in this chapter.

Dense samples of core-shell and homogeneous core PNIPAM microgel suspensions (labeled as CS-PNIPAM and HC-PNIPAM respectively) were prepared by concentrating the as prepared suspensions by centrifugation at 6500 rpm. When these dense samples were diluted with known amount of Milli-Q water and kept undisturbed in glass vials for 24 hours, the CS-PNIPAM sample exhibited iridescence under white light illumination (see Fig. 2.8(a)), indicating crystallisation, whereas the HC-PNIPAM sample did not show iridescence, indicating absence of crystallisation. The volume fraction (ϕ) for CSPNIPAM crystalline sample was calculated to be ~ 0.8 using the Bragg peak position determined from UV-Vis spectroscopy [2] which is described in section 2.3.4. The volume fraction of dense HC-PNIPAM turbid sample was independently measured as reported in ref [8,9]. The polymer content (in g cm^{-3}) in the aqueous suspension was determined by the drying method [9]. A known amount of the PNIPAM microgel suspension is first dried at a temperature higher than 50°C and then weighted to determine the mass of polymer. Following the work reported in ref [9], we considered that a particle is composed of 71 wt % of polymer and the rest is water at 50°C. From the hydrodynamic particle diameter, d_h measured by DLS at 50°C, the number of particles was estimated as

$$N_p = \frac{6m_{polymer}}{\pi d_{h(50^0)}^3} \left(\frac{1}{\rho_{polymer}} + \frac{0.29}{0.71\rho_{water}} \right)$$
 (2.1)

Further volume fraction is determined using the equation

$$\phi = N_p \pi d_h^3 / 6V_s \tag{2.2}$$

Where V_s is the volume of PNIPAM suspension taken for drying. For dense HC-PNIPAM sample, ϕ calculated to be 0.89.

Sample	CS-PNIPAM	HC-PNIPAM
Hydrodynamic diameter, $d_h (T = 20^{\circ}C)$	270 nm	1480 nm
SPD	11%	13%
Volume fraction, φ	0.80	0.89

Table 2.3. Sample details of CS-PNIPAM and HC-PNIPAM dense microgel suspensions

2.2 Sunset yellow (SSY) liquid crystals

2.2.1 Purification of Sunset Yellow (SSY) powder

The compound disodium salt of 6-hydroxy-5-[(4-sulfophenyl) naphthalenesulfonic acid commonly known as Sunset Yellow (SSY) was purchased from Sigma Aldrich with 90% purity. The chemical structure of the compound is shown in Fig. 1.11 (chapter1, section 1.2.2). SSY was further purified by recrystallization from water and ethanol[10-12]. Purification was carried out by preparing a 20 wt% solution of SSY powder, Milli-Q water and ethanol (1:20 water to ethanol volume ratio is maintained). All the reagents were mixed at a higher temperature ($T \sim 70^{\circ}$ C) using a magnetic stirrer to ensure a homogeneous solution. The mixture was then allowed to precipitate for one hour at room temperature before being filtered through Whatman filter paper. Recrystallization and filtering were repeated 3-4 times and finally the precipitates were dried for 48 hours in a vacuum oven set at a temperature of 110°C.

2.2.2 Preparation of Sunset Yellow liquid crystal (SSY LC) samples

SSY is known to exhibit liquid crystal phases with nematic ordering in the concentration regime ~ 28 to 34 wt% at room temperature (see Fig. 1.12 (chapter 1, section 1.2.2). To achieve a liquid crystalline state, the requisite amount of SSY was dissolved in known amount of Milli-Q water. The sample container was promptly sealed and the solution was sonicated until it appeared homogenous. All the measurements reported in this thesis corresponds to 32 wt% aqueous solution of Sunset Yellow (hereafter called SSY LC), which displays nematic phase [13]. A schematic view of the molecular arrangement in the nematic phase is displayed in Fig. 1.10 (chapter 1, section 1.2.1). The time difference between the sample preparation and any measurements was minimised to avoid concentration change due to evaporation of water.

The sample cells for polarizing optical microscopy (POM) were prepared using glass substrates (1mm thickness). The glass substrates are thoroughly sonicated using detergent solution, acetone and distilled water. Further, these glass substrates are dried by keeping them inside a vacuum oven set at 110° C for one hour. The dried glass substrates were attached by a mixture of UV curable epoxy glue and silica beads of 5 μ m diameter. The thickness of the cell was calculated using an interferometric approach with an Ocean optics spectrometer (HR 4000 CG-UV-NIR) [14]. The corresponding spectrum was analysed using Spectra-suite software. The spectrum comprised of alternating maxima and minima, and the cell thickness (t_c) is calculated with the formula, $t_c = \frac{\lambda_m \lambda_n}{\lambda_n - \lambda_m} \times \frac{n-m}{2}$, where λ_m and λ_n represents the wavelength corresponds to m^{th} and n^{th} maxima or minima respectively. After measuring the cell thickness, a drop of SSYLC sample was sandwiched between the glass substrates (see Fig. 2.3) and then all four sides of the cell were sealed with epoxy glue to prevent water evaporation from the sample. The sample's texture was observed using a polarizing optical

microscope (Olympus BX51) at room temperature (T=24 0 C). A typical texture of the nematic phase of SSYLC is shown in Fig. 1.12(b) (chapter 1, section 1.2.2). Phase transition temperatures were measured using a Metler (FP 90) controller with a heater.

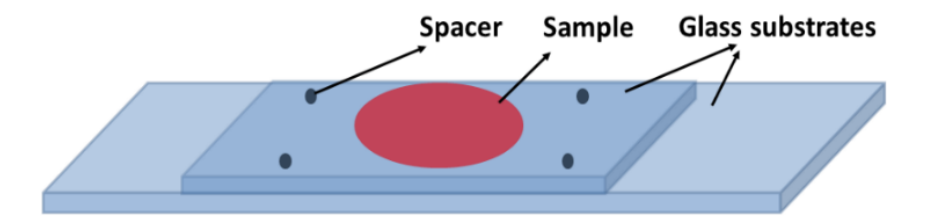


Fig. 2.3. Schematic diagram of sample cell for POM observations

2.3 Experimental methods

2.3.1 Light scattering technique

In colloidal suspensions, the length scale of interest ranges from ~ 100 nm to several microns and the time scale ranges from $\sim 10^{-6} {\rm sec}$ to $\sim 10^3 {\rm sec}$, hence, dynamic light scattering becomes the appropriate technique to investigate their dynamics [15-17]. Basic principles of operation, instrumental details and analysis methods of DLS techniques used for the characterization and investigation of dynamics in transparent, turbid and non-ergodic colloidal suspensions are discussed below.

a) Auto correlation based dynamic light scattering (DLS)

Dynamic Light Scattering (DLS), also known as quasi-elastic light scattering (QELS) or photon correlation spectroscopy (PCS), is a non-invasive technique for determining the size and size polydispersity of polymers and other colloidal particles in the submicron range dispersed in a solvent. Colloidal particles in suspension undergo Brownian motion as a consequence of non-compensated momentum transfer from solvent molecules upon collision [16]. As a result, the intensity of the light scattered by these colloidal particles fluctuates in time around an average value. The correlation between intensity fluctuations contain information about the relaxation of density or concentration fluctuations in the systems, hence

the dynamics of the colloidal particles. Density or concentration gradient decay through the diffusion process. Diffusion of colloidal particles depends on the size of particle *i.e.*, smaller particles diffuse rapidly and larger particles diffuse slowly, and also on the viscosity of solvent through Stokes-Einstein relation as,

$$d_h = \frac{k_B T}{3\pi \eta_S D_0} \tag{2.3}$$

Here D_0 is referred to as the free diffusion coefficient as measured in DLS by measuring on dilute (non interacting) samples. k_B denote the Boltzmann constant, T is the temperature (in Kelvin) and η_S is the viscosity of the solvent.

We measured the size and size polydispersity of the colloidal samples using a particle size analyzer based on DLS technique (M/s Anton Paar GmbH, Germany, model: LitesizerTM 500). Figure 2.4 displays schematic diagram of a simple DLS measurement setup. Measurement specifications for LitesizerTM 500 are displayed in Table 2.4.

Technology	Dynamic light scattering (DLS)		
Light source	Semiconductor laser of operating wavelength 658 nm		
Detection angles	15°, 90°, 175°		
Particle size (diameter) range	0.3 nm - 10 μm		
Minimum sample concentration	0.1 mg/mL (lysozyme)		
Temperature range	0 - 90°C		
Minimum volume of sample	20 μL		
Accuracy of measurements	Better than +/-2% on NIST traceable standards		
Analysis software	Kalliope™		

Table 2.4. Particle analyzer Litesizer TM 500: Measurement specifications.

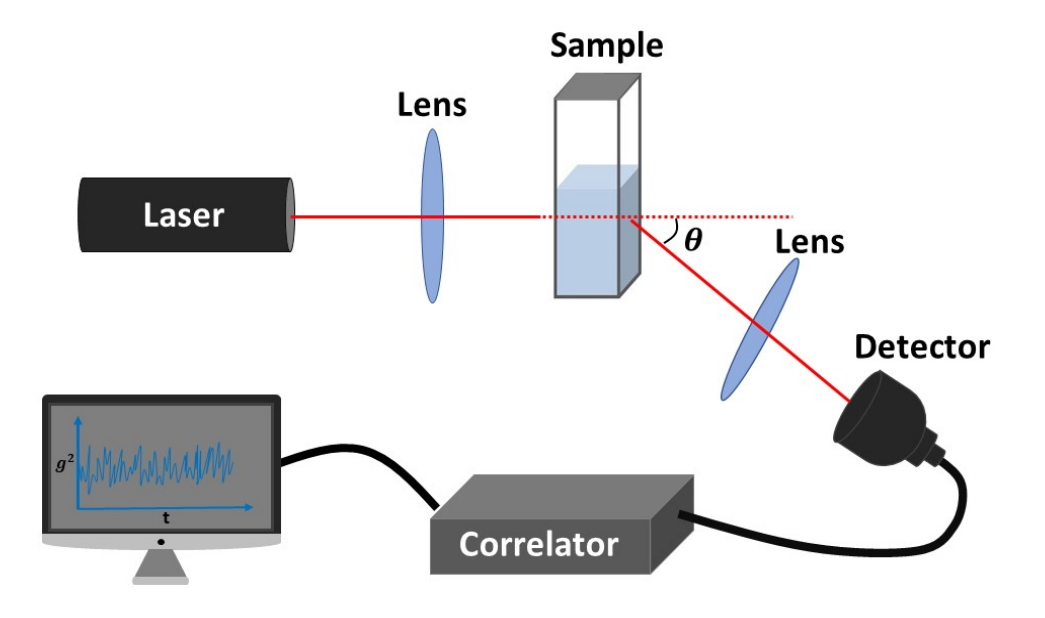


Fig. 2.4. Schematic diagram of a DLS measurement set up

In general, any physical property, A(t) which fluctuates over time shows two different values at times t_1 and t_2 if time lag τ is large (Fig. 2.5 (a)). Here $t_2 = t_1 + \tau$. However, $A(t) = A(t+\tau)$ for small values of τ . The deviation of A(t) and $A(t+\tau)$ increases as the value of τ increases. This means that, for small values of τ , t and t and t are correlated and this correlation disappears as the value of t becomes large as compared with the time period of the fluctuations. The measure of this correlation is expressed by auto correlation function (ACF) of the physical property, t which decays from the maximum correlated value (t and t and t are correlated value (t and t are correlated value (t and t and t are correlated value (t and t are correlated value (t

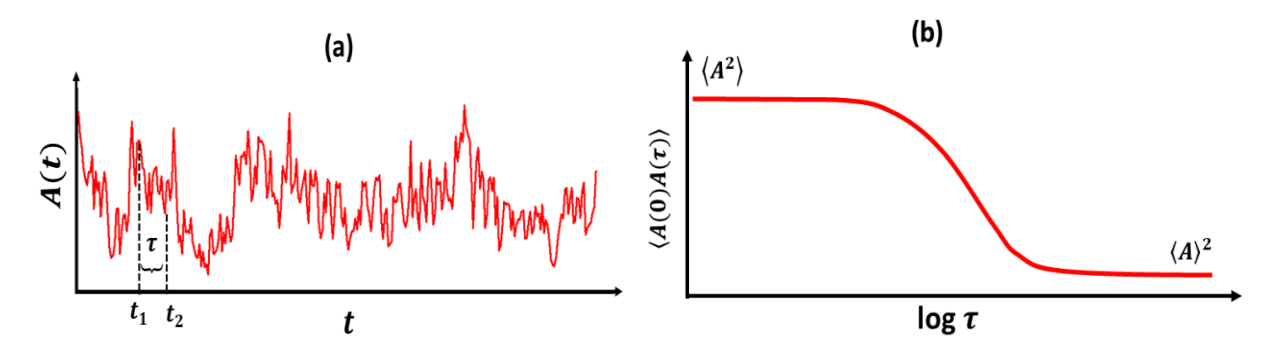


Fig. 2.5 (a) Fluctuation in $A(t).\tau$ represents the time lag between t_1 and t_2 . (b) ACF of A(t).

Auto correlation function (ACF) of A(t) can be defined as below [16,17],

$$\langle A(0)A(\tau)\rangle = \lim_{T \to \infty} \frac{1}{T} \int_0^T A(t)A(t+\tau)dt \tag{2.4}$$

where it is assume that the time average doesn't depend on the starting time. The mean value of the physical property, A(t) is given by,

$$\langle A \rangle = \lim_{T \to \infty} \frac{1}{T} \int_0^T A(t) dt \tag{2.5}$$

The discrete form of Eq. 2.5 is given by,

$$\langle A(0)A(\tau)\rangle = \lim_{n \to \infty} \frac{1}{n} \sum_{j=1}^{n} A_j A_{j+m}$$
 (2.6)

And the time average of A is given by,

$$\langle A \rangle = \lim_{n \to \infty} \frac{1}{n} \sum_{j=1}^{N_p} A_j \tag{2.7}$$

here A_j represents the value of the property at the j^{th} interval and, $T = N_p \Delta t$, $t = j \Delta t$, and $\tau = m \Delta t$. The autocorrelation function decays from a maximum value of $\langle A^2 \rangle$ to a minimum value of $\langle A \rangle^2$, and it is usually a single exponential decay. This can be expressed as,

$$\langle A(0)A(\tau)\rangle = \langle A\rangle^2 + \{\langle A^2\rangle - \langle A\rangle^2\} \exp\left(\frac{-\tau}{\tau_c}\right)$$
 (2.8)

where τ_c indicates the relaxation time of the property otherwise known as characteristic decay time.

In the case of light scattering studies on colloidal suspensions, a laser beam is allowed to focus on a small area of the colloidal suspension, and the light scattered by the suspension is collected by a detector (Fig 2.4). Light gets scattered from each scattering point, and the instantaneous scattered field is the superposition of all the scattered light.

Let us consider N_p monodisperse colloidal particles suspended in a scattering volume v_s and each of which comprises n scattering centers. If A_s is the scattering amplitude, then scattered electric field at a scattering angle θ at any instant of time t from N_p colloidal particles in the scattering volume v_s [15-17] is given by,

$$E_s(\vec{q},t) = \sum_{i=1}^{N_p} \sum_{\alpha_i=1}^n A_s \exp[i\vec{q}.\vec{r}_{i,\alpha_i}(t)]$$
 (2.9)

Where $\vec{r}_{i,\alpha_i}(t)$ denotes the position vector of the scattering center α_i in the i^{th} particle at any instant of time t.

The scattered intensity $I_s(\vec{q},t)$ and scattered electric field $E_s(\vec{q},t)$ are connected by the relation

$$I_{S}(\vec{q},t) = |E_{S}(\vec{q},t)|^{2}$$
 (2.10)

Where \vec{q} is the scattering wave vector whose magnitude is given by,

$$q = \frac{4\pi\mu_{\rm S}}{\lambda}\sin\left(\frac{\theta}{2}\right) \tag{2.11}$$

Here μ_s denotes the solvent refractive index and λ represents the wavelength of incident laser light source.

In a DLS measurement, the time dependence on the scattered light at a specific scattering angle is evaluated by computing intensity-intensity autocorrelation function of the scattered light. This is often accomplished with a digital correlator. The normalized intensity autocorrelation function of scattered intensity can be defined as,

$$g^{(2)}(q,t) = \frac{\langle I_S(q,t)I_S(q,0)\rangle}{\langle I_S(q,0)\rangle^2}$$
 (2.12)

For a system of N_p particles, the normalised electric field correlation function can be written as,

$$g^{(1)}(q,t) = f(q,t) = \frac{\langle E^*_{S}(\vec{q},0)E_{S}(\vec{q},t)\rangle}{\langle E_{S}(\vec{q},0)\rangle^2}$$
(2.13)

For a large number of scatterers, $E_s(q,t)$ is a Gaussian random variable, then intensity auto correlation function may be expressed as [15-17] based on below assumptions,

- i) Particle dynamics in the suspension are stochastically independent.
- ii) The amplitude of the scattered electric field follows a Gaussian distribution.

the auto correlation functions of normalized intensity $g^{(2)}(q,t)$ and normalized electric field $g^{(1)}(q,t)$ can be connected through Siegert's relation as follows

$$g^{(2)}(q,t) = 1 + \beta |g^{(1)}(q,t)|^2$$
(2.14)

Here β_f is coherence factor which is ideally equal to 1. Moreover, β_f depends on the size of the aperture positioned in front of the detector. Any variation in the size of the aperture results in a reduction in the value of β_f .

In a dilute non interacting monodisperse system (gas-like disordered system), a colloidal sphere undergoes free diffusion caused by Brownian motion with D_0 representing the free diffusion coefficient. Then f(q, t) can be expressed as,

$$f(q,t) = \exp(-q^2 < \Delta r^2(t) > /6) = \exp(-D_0 q^2 t) = \exp(-\Gamma t)$$
(2.15)

Where $\Gamma = D_0 q^2$ is the decay constant. The mean square displacement or MSD related to D_0 as, $\langle \Delta r^2(t) \rangle = 6D_0 t$. The free diffusion coefficient D_0 is used to calculate the hydrodynamic diameter, d_h of a spherical particle through the Stokes-Einstein relation (Eq. 2.3)

For a size polydisperse suspension, Γ has a distribution $G(\Gamma)$. In this case f(q, t) can be written as [18],

$$f(q,t) = \int_0^\infty G(\Gamma) \exp(-\Gamma t) d\Gamma$$
 (2.16)

Laplace inversion of f(q, t) gives $G(\Gamma)$ which can be further used to determine the particle size distribution. Complex computations are required to determine the functional form of the distribution. The cumulant approach is the most appropriate way for analyzing the correlation function of polydisperse systems to obtain the fundamental information about average particle size and size polydispersity of the suspension. The cumulant analysis is usually performed by expanding $\ln (f(q, t))$ up to the third order:

$$\ln(f(q,t)) = -\bar{\Gamma}t + \frac{k_2}{2!}t^2 - \frac{k_3}{3!}t^3 + \cdots, \tag{2.17}$$

Here $\bar{\Gamma}$ is the first cumulant which is connected to the average diffusion coefficient, \bar{D} as $\bar{D}=\bar{\Gamma}q^2$ and the average diameter of colloidal particles is derived from \bar{D} using Stokes-Einstein equation. Whereas, second cumulant, k_2 determines the size polydispersity (SPD), where SPD defined as the ratio of standard deviation in diameter to that of average diameter. SPD can be calculated using second cumulant, using the equation $SPD=\frac{\sqrt{k_2}}{\bar{\Gamma}}$.

MSD data as a function of time can be fitted to a power law (as given in Eq. 1.11) as expressed as, $<\Delta r^2(t)> \propto t^{\alpha}$. Particle dynamics is considered to be diffusive if $\alpha=1$. Similarly, particle dynamics is referred to be sub-diffusive if $\alpha<1$ and super diffusive if $\alpha>1$ [19].

As explained in Chapter 1, in the case of dense suspension of interacting particles, D_S describes the motion of colloidal particles over short times ($\tau_B \ll t \ll \tau_R$) and D_L describes the motion over long times ($t \gg t_R$). DLS measurements of diffusion coefficients are dependent on q. Thus, MSDs for the short and long times can be defined as $<\Delta r^2(q,t)>=6D_S(q,t)$ and $<\Delta r^2(q,t)>=6D_L(q,t)$ respectively. D_0,D_S , and D_L measured using DLS technique, which characterise the self-diffusion of single particle in a suspension are described in detail in chapter 1.

b) Cross-correlation based 3D dynamic light scattering (3D- DLS)

The simple Dynamic Light Scattering technique explained in the preceding section is based on the principle of single scattering of light, in which photon scattered by a particle reach the detector without being scattered by additional particles. However, multiple scattering of light [20] causes a major problem in investigating the dynamics of the particle in highly concentrated turbid suspensions where particle density or refractive index contrast is reasonably high [21]. In such a scenario, dynamic light scattering techniques based on the cross-correlation method, often referred to as 3D-DLS can be effectively used [22,23]. The

3D-DLS allows to measure singly scattered light in the presence of multiply scattered light and thus be utilized efficiently to describe the dynamics in turbid colloidal media.

In the present study, light scattering measurements on turbid colloidal samples have been performed using a 3D-DLS setup (LS Instruments AG, Fribourg, Switzerland). Figure 2.6 (a) shows a schematic diagram of a 3D-DLS setup which is equipped with a He-Ne laser source operating at a wavelength, $\lambda = 632 \ nm$. A single beam from the laser source is split into two by a beam splitter (B). These beams are focused at the sample cell (SC) using a plano-convex lens (L1). The sample cell is kept in a vat filled with decalin which serves as an index matching liquid. The sample temperature can be varied with in a range of 10° C to 60° C while maintaining a stability of 0.1° C by circulating heat exchanger fluid around the vat. Due to the overlapping of two laser beams at the centre of the sample cell, the intercept of the intensity cross-correlation function will decrease from its ideal value 1. Acousto-optic modulators (AOMs) can be used to increase the intercept of the intensity cross-correlation function. AOM periodically allows one of the two beams by diffracting the other beam out of the sample cell hence overlapping of the two beams is avoided. Beams that are diffracted from the sample cell are then focused by a plano-convex lens (L2) placed at the detector's end. These diffracted

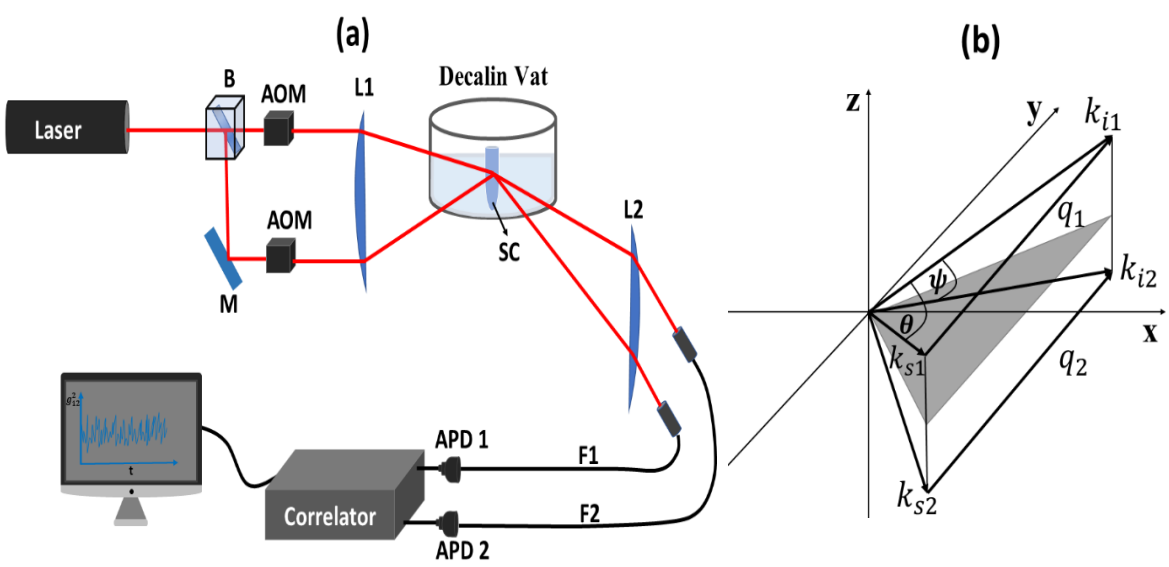


Fig. 2.6. a) Schematic diagram of a 3D-DLS set up with cross correlation technique **b)** ray diagram showing scattering geometry of 3D light scattering setup. B- Beam splitter; M- Mirror; AOM- Acousto optic modulator; SC- Sample cell; APD-Avelanche photo diode; F- Fiber optic cable, L- Plano-convex lens

beams are then carried by two single mode fibres (F1 and F2) and fed into avalanche photodiodes (APD1 and APD2) which are capable of detecting even low-intensity light. Both the sample cell and detectors are movable. The detector goniometer rotates from 5° to 150° which corresponds to a q range of 0.12×10^5 cm⁻¹ to 2.54×10^5 cm⁻¹. Finally, the APDs feed the scattered light intensity onto a cross-correlator, where it is processed and the results are displayed on the monitor. The setup is aligned as per the procedure reported in ref. [24].

In a 3D light scattering method, two light scattering measurements are carried out simultaneously using two laser beams with wave vectors \vec{k}_{i1} and \vec{k}_{i2} and they intersect at an angle ψ at the centre of the vat (Fig. 2.6 (b). The scattered light from corresponding beams is detected at wave vectors \vec{k}_{s1} and \vec{k}_{s2} using two detectors, at two different planes. To make it possible, two detectors are fixed on the goniometer so that both detectors detect the same scattering wave vector with respect to the single scattered light, $|\vec{q}| = |\vec{k}_{i1}| - |\vec{k}_{s1}| = |\vec{k}_{i2}| - |\vec{k}_{s2}|$. The scattered light intensities $I_1(q,t')$ and $(I_2(q,t'+\tau)$ measured by two detectors is then correlated to determine the normalized intensity cross-correlation function, $g_{12}^{(2)}(q,\tau)$ which is denoted by the equation:

$$g_{12}^{(2)}(q,\tau) = \frac{I_1(q,t')(I_2(q,t'+\tau))}{\langle I_1(q) \rangle \langle I_2(q) \rangle}$$
(2.18)

Each detector detects light that has been scattered singly or multiple times. Light scattered multiple times will arrive at the detector with different \vec{q} . The intensity of light scattered at the same \vec{q} is temporally correlated, whereas the intensity of light scattered at different \vec{q} is temporally uncorrelated. As a result, when the intensities from two detectors are cross-correlated, multiple scattered components of light provide a constant background while single scattered component of light contributes to the correlation. Siegert's relation is used to determine f(q,t) from $g_{12}^{(2)}(q,\tau)$.

$$g_{12}^{(2)}(q,\tau) = 1 + \left| \beta_{eff} f(q,t) \right|^2 \tag{2.19}$$

Where β_{eff} is the effective coherence factor given as $\beta_{eff} = \beta_m \beta_c \beta_{12}$ with β_m , β_c and β_{12} are the coherence factors attributed to multiple scattering, instrument alignment and commonality to two laser beams. For a turbid colloidal suspension, the time-averaged intensity owing to singly scattered light alone can be obtained as $I(q) = \sqrt{I_1^M I_2^M \beta^{conc}/\beta^{dilute}}$ with I_1^M and I_2^M are the intensities detected at two detectors respectively [22].

c) Non-ergodic analysis

Dense colloidal suspensions are known to be non-ergodic, *i.e.*, the time averaged intensity and ensemble averaged intensity of the scattered light (at a given q) differ from each other. In the case of non-ergodic colloidal suspensions, it is observed that the time-averaged $g^{(2)}(q,t)$ shows different values when measured at different locations of the sample. To obtain the true ensemble-averaged $g^{(2)}(q,t)$ one could average the time-averaged $g^{(2)}(q,t)$ from different sample locations. However, this method is time-consuming. Pusey and Van Magen [25] have proposed a technique for determining f(q,t) for non-ergodic samples by utilizing time-averaged $g^{(2)}(q,t)$ measurements obtained at a single site within the sample. As per which,

$$f(q,t) = \frac{Y-1}{Y} + \frac{\sqrt{g^{(2)}(q,t) - \sigma_I^2}}{Y}$$
 (2.20)

with Y and σ_I^2 stands for the non-ergodicity factor and mean squared fluctuation of the scattered light intensity respectively. These quantities are given as follows,

$$Y = \frac{\langle I(q) \rangle_E}{\langle I(q) \rangle_T} ; \qquad \sigma_I^2 = \frac{\langle I^2(q) \rangle - \langle I(q) \rangle^2}{\langle I(q) \rangle^2} = g^{(2)}(q,0) - 1$$
 (2.21)

Here, $\langle I(q) \rangle_T$ and $\langle I(q) \rangle_E$ denotes the time averaged and ensemble averaged intensities of scattered light. $\langle I(q) \rangle_T$ is determined by time averaged measurements at a single site in sample. In contrast, $\langle I(q) \rangle_E$ is determined by recording the scattered light

intensities from various locations with in the sample which is achieved through the rotation or translation of the sample while performing the measurements.

For dense turbid colloidal suspensions, field-field correlation function, f(q,t) can be obtained by cross-correlation methos[3, 26] which is given by

$$f(q,t) = 1 + \frac{1}{\gamma} \left\{ \left[\frac{g_{12}^{(2)}(q,t) - g_{12}^{(2)}(q,0)}{\beta^{dilute}} + 1 \right]^{1/2} - 1 \right\}$$
 (2.22)

Here, non-ergodicity factor Y for dense turbid colloidal suspensions were obtained according to the non-ergodic analysis described in ref.[25, 27].

$$Y = \sqrt{\frac{\langle I_1(q) \rangle_{E \langle I_2(q) \rangle_E}}{\langle I_1(q) \rangle_{T \langle I_2(q) \rangle_T}}}$$
(2.23)

The sub-scripts E, T represent the ensemble averaged and time averaged scattered light intensities respectively. Similarly, the digits 1 and 2 denotes the detector 1 and detector 2.

2.3.2 UV- visible - NIR spectroscopy

An Agilent Technologies Cary 5000 UV-Vis-NIR spectrometer was used to investigate the structural ordering in dense microgel crystals by recording the Bragg diffraction from these colloidal crystals. The schematic of a UV-Visible-NIR spectrophotometer is shown in Fig. 2.7. In a UV-visible-NIR spectrophotometer, the incident wavelength is varied from UV to the visible range and then to the near infrared (NIR) while maintaining a constant angle of measurement.

The UV-Visible-NIR spectrophotometer used consists of double beam arrangement, where a deuterium lamp and a tungsten halogen lamp are employed to achieve the UV region and visible region respectively. Hence, the spectrometer works in a wavelength range of 3300 nm to 200 nm. Our UV-visible-NIR spectrophotometer is able to provide a minimum resolution of 1 nm. Using a double monochromator, the composite light has been dispersed into different components of wavelength. The incident light is split into two beams, termed as

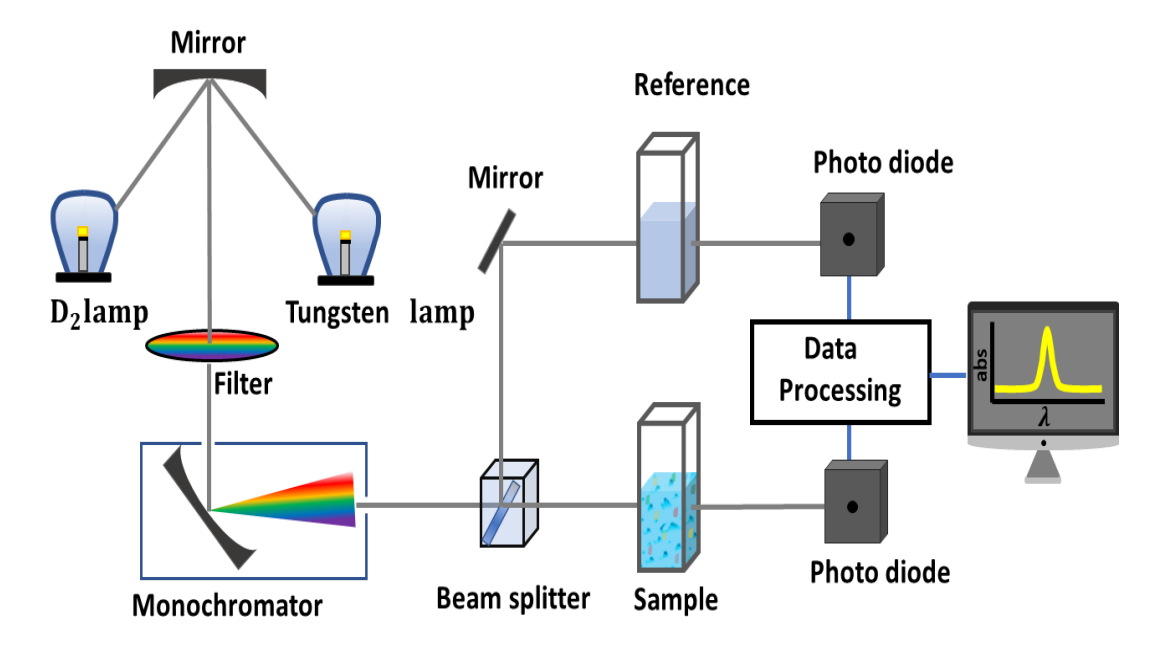


Fig. 2.7. Schematic diagram of UV-Visible-NIR spectrometer

sample beam and reference beam, using a chopper mirror. The beams passing through the reference cell and sample cell are detected using two PMTs employed in the spectrometer, where reference beam is used to cancel out any effect either from the sample cell or from the solvent.

The dense suspension of CS-PNIPAM microgel suspension was observed to be crystallized when kept undisturbed for 24 hours Fig. 2.8(a). All UV- visible spectra of PNIPAM microgel crystals reported in this thesis were recorded in the normal incidence mode, with samples taken in 1 mm path length quartz cells.

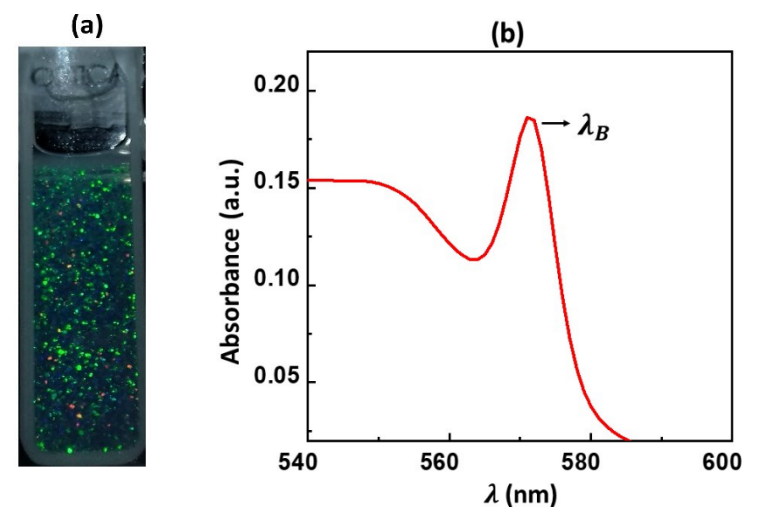


Fig. 2.8. (a) Iridescence from CS-PNIPAM microgel crystals under visible light illumination, at 21°C. (b) UV-Visible spectrum from CS-PNIPAM microgel crystals.

Peaks in the absorbance spectra of PNIPAM microgel crystals Fig. 2.8(b) are caused by Bragg diffraction of λ that satisfy the Bragg condition,

$$n\lambda = 2d_{hkl}\mu_m sin\theta_q. \tag{2.24}$$

Here d_{hkl} is the interplanar spacing between the crystal planes having miller indices (hkl) and n represents the order of diffraction. For the normal incidence the glancing angle, θ_g is set at 90° hence Eq. 2.24 becomes,

$$n\lambda_{hkl} = 2d_{hkl}\mu_m \tag{2.25}$$

and subsequent peaks emerge for λ values satisfying the below condition,

$$\lambda_{h_2k_2l_2} = \frac{\sqrt{h_1^2 + k_1^2 + l_1^2}}{\sqrt{h_2^2 + k_2^2 + l_2^2}} \lambda_{h_1k_1l_1} \tag{2.26}$$

The absorption spectrum of the fcc structure shows prominent peak that corresponds to the (111) plane, whereas that of the hcp structure shows a prominent peak corresponds to the (002) plane. The crystallization of PNIPAM microgel suspension into a fcc structure is reported elsewhere [23]. The first Bragg peak position, λ_B corresponds to the (111) plane of the fcc structure can be used to determine the particle number density, n_p and interparticle separation d_{nn} as expressed below,

$$n_p = \frac{4}{3\sqrt{3}} \left(\frac{2\mu_s}{\lambda_B}\right)^3; \ d_{nn} = \sqrt{\frac{3}{2}} \left(\frac{\lambda_B}{2\mu_s}\right)$$
 (2.27)

The results obtained by performing UV-Visible measurements on dense PNIPAM microgel crystals are reported in Chapter 3.

2.3.3 Rheology

a) Fundamentals of Rheology

Rheology deals with the flow and deformation of a material when subjected to an external shear force. It is an important tool for probing the structure-property relationships in viscoelastic materials, especially in pastes, polymers and other complex materials [28,29]. It

is based on two essential quantities: first, a body's deformation (and connected to it the deformation rate). Second, the tension on the body that is required to cause this deformation. The most fundamental purpose of rheology is to measure and describe the relationship between deformation and stress using constitutive models. Moreover, rheology can be used as an analytical tool to explore the microscopic properties of a material if suitable models that link the microstructure and macroscopic flow behavior are available.

Stress and deformation can be defined by employing the simple shear experiment in its most basic, scalar version, as shown in Fig. 2.9. Consider a cuboidal object having height h and area A fixed on one side; a force F acting in the x-direction on the other side creates a shear stress equal to the force normalised by the area A; hence, the stress has pressure units. If the object is in fluid phase, then the top side will move in the x-direction with a velocity, v = dx/dt Normalizing length dx by height h yields the unitless quantity of deformation, y known as strain.

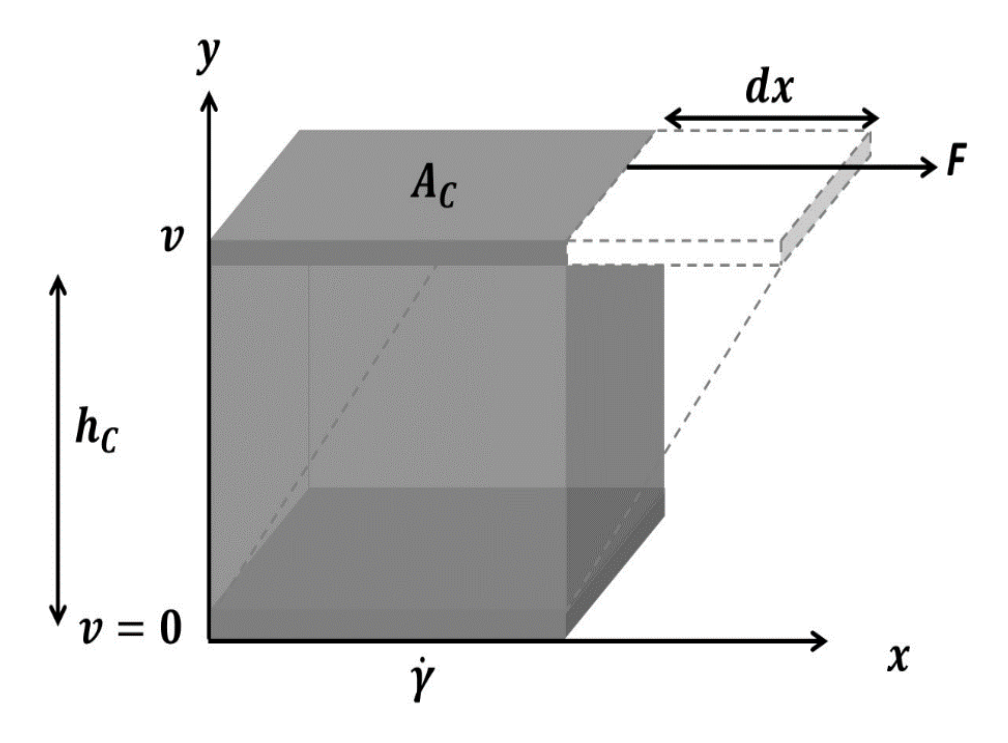


Fig. 2.9. Simple shear experiment on a cuboidal object. The bottom plate is fixed while top plate is pulled by a shear force F. The geometry independent rheological parameters can be defined as, stress $(\sigma) = F/A$, strain $(\gamma) = dx/h$ and shear rate $(\dot{\gamma}) = d\gamma/dt = v/h$

$$\sigma = \frac{F}{A} \tag{2.28}$$

$$\gamma = \frac{dx}{h} \tag{2.29}$$

$$\dot{\gamma} = \frac{d\gamma}{dt} = \frac{v}{h} \tag{2.30}$$

There are two idealised archetypes of material behavior that link σ and γ , (i) ideal elastic solid, where σ directly proportional to γ that is defined by Hooke. The proportionality constant G, known as the shear modulus (Eq. 2.31) and measured in units of Pa. Equation 2.31 is basically identical to the formula for a one-dimensional spring, in which force F is proportional to the elongation of the spring, dx.

$$\sigma = G\gamma \tag{2.31}$$

(ii) In the case of an ideal liquid, σ is not a function of γ but the function of shear rate, $\dot{\gamma}$ which is the time derivative of γ . According to Newton's law, the ideal liquid resists shear σ , such that σ is linear in the shear rate $\dot{\gamma}$. The viscosity, η (Eq. 2.32) expressed in Pascal seconds, Pas, quantifies this resistance.

$$\sigma = \eta \dot{\gamma} \tag{2.32}$$

b) The Maxwell model

Complex fluids in general, show an intricate combination of elastic and viscous properties over a broad concentration and/or molecular weight range, making them behave neither like Hookean solids nor like Newtonian liquids. Maxwell introduced a serial combination of a Newtonian liquid and a Hookean solid as the simplest method for incorporating elastic effects into a fluid. The Maxwell model is illustrated schematically in Fig. 2.10., where the spring obeys Hooke's law and dashpot obeys Newton's law.

The differential equation for the Maxwell model can be constructed by considering that stress in the spring (σ_s) as well as in the dashpot (σ_d) are equal, and the total strain (γ_t) equals

to the sum of the individual strains (γ_s and γ_d for spring and dashpot respectively). In addition, the total shear rate ($\dot{\gamma}_t$) equals the sum of the individual shear rates ($\dot{\gamma}_s$ and $\dot{\gamma}_d$).

$$\sigma_{\rm S} = \sigma_{\rm d} \tag{2.33}$$

$$\gamma_t = \gamma_s + \gamma_d \tag{2.34}$$

$$\dot{\gamma}_t = \dot{\gamma}_s + \dot{\gamma}_d \tag{2.35}$$

By applying Hooke's law and Newton's law, $\dot{\gamma}_s$ can be replaced by $\dot{\sigma}/G$ and $\dot{\gamma}_d$ can be replaced by σ/η . Plugging these expressions into Eq. 2.36, first order differential equation, Eq. 2.37 will be obtained. Equation 2.38 can be written from Eq. 2.37 where relaxation time $\lambda_t = \eta/G$ has been incorporated.

$$\dot{\gamma}_t = \dot{\sigma}/G + \sigma/\eta \tag{2.36}$$

$$\dot{\sigma} = G\dot{\gamma}_t - \sigma/\lambda_t \tag{2.37}$$

For a measurement at t = 0 with a constant $\dot{\gamma}$,

$$\sigma + \lambda_t \frac{\partial \sigma}{\partial t} = \eta \dot{\gamma} \tag{2.38}$$

Higher λ_t values indicate elastic response whereas lower λ_t values indicate viscous response. Here η represents the zero-shear viscosity.

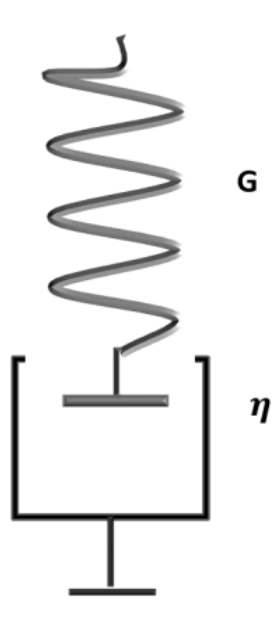


Fig. 2.10. Maxwell model that incorporates elastic effects for a viscous fluid: serial connection of a Hookean solid and a Newtonian liquid.

c) Rheometer and measuring systems

The rheological properties of a material are investigated using a rheometer that applies shear strain, γ and measures material response in terms of shear stress, σ or strain rate, $\dot{\gamma}$ and vice versa. The rheometer comprises of a measuring cell which is kept immovable and a movable measuring tool which is either rotated or oscillated during the time of measurements. Recently available rheometers are capable of operating in both strain-controlled as well as in stress-controlled mode. Rheometer set to operate in the strain-controlled mode measures the material response in the form of stress, whereas, if the rheometer is set in the stress-controlled mode, then the material response will be measured in terms of strain. We performed all the rheological measurements in strain-controlled mode.

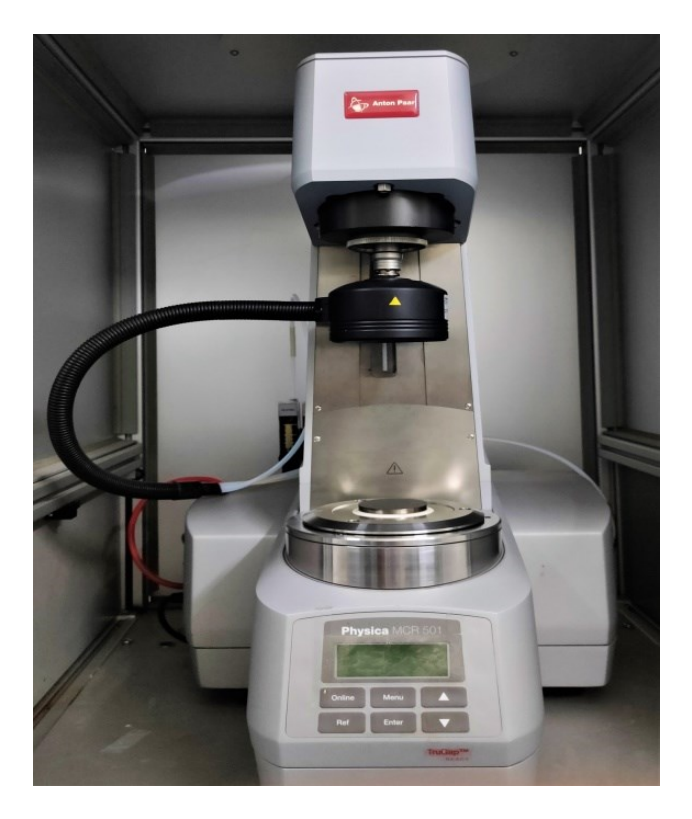


Fig. 2.11. Photograph of MCR-501 rheometer (Anton Paar, Germany)

We have performed all sets of rheological measurements using an MCR-501 rheometer (Anton Paar, Germany) (Fig. 2.11). It is equipped with an electrically commutated (EC) synchronised motor which operates on air bearings to produce the finest movements. A high-

resolution optical encoder attached to the rheometer controls the angular deflection and precisely measures very small angular displacements down to 0.1μ rad.

The current MCR rheometer is able to measure torque with in a range of $0.1 \,\mu\text{Nm} - 230$ mNm with a resolution of $0.001 \,\mu\text{Nm}$, and it also supports a frequency range between 10^{-5} to 10^2Hz . A normal force sensor is an important component of the MCR rheometer which is connected to the air bearings. Depending on the sample behavior in the steady state and dynamic state, the normal force sensor measures the normal force in both the upward (positive) and downward (negative) directions.

Rheological measurements are controlled and analyzed using Rheoplus software. The two plates of the measuring geometry (measuring cell and measuring tool) are separated by a minimum gap which is governed by the TruGap technology of the rheoplus software. For constant temperature measurements, a peltier based temperature controller along with a hood is connected to the rheometer. This peltier temperature controller ensures measurements with an accuracy of 0.02°C. For the proper functioning of the air bearings, an oil-free compressor is connected to the rheometer. The compressor maintains a required amount of pressure in the rheometer (5-8 bars). Additionally, an external chiller is also attached to the rheometer to circulate water throughout the system in order to maintain the room temperature (25°C). There are different types of measuring cells and measurement tools, such as parallel plates, cone and plate, cup and bob, double gap, etc. However, appropriate geometry needs to be selected based on the sample viscosity. In our rheological measurements, we used cone and plate measuring geometry to perform oscillatory measurements on dense suspensions of PNIPAM samples, whereas transparent parallel plates were used to perform steady state rotational measurements on SSY liquid crystal samples. A brief discussion of these measuring systems is given below.

i) Cone and Plate measuring system

A cone and plate (CP) measuring system consists of two major components. A bob having a conical surface (upper plate) and a fixed plate with a flat surface (bottom plate). Figure 2.12 depicts a schematic illustration of a cone and plate measuring geometry. The cone radius, R_c and cone angle φ of the conical surface are the major factors affecting the accuracy of the measurements.

The upper plate usually comes in two distinct radii, 12.5mm and 25mm. In the case of low viscous fluids, measurements with 25mm geometry are more accurate than 12.5mm geometry. This is due to the larger shear area provided by the 25mm geometry, which improves the sensitivity to low torque or shear stress values.

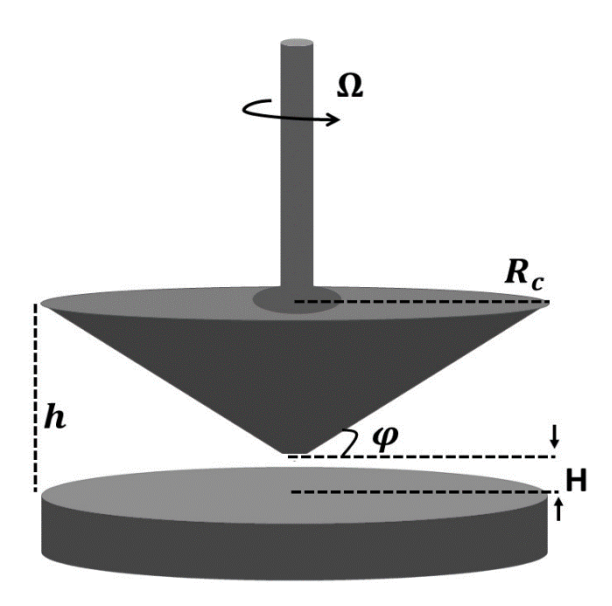


Fig. 2.12. Schematic representation of cone-plate measuring system. The symbols indicate the following parameters: R_c -cone radius, φ -cone angle, h - gap between top and bottom plates at the edge, H -cone truncation, Ω - angular frequency

A significant aspect of the CP measuring system is that, the shear rate is independent of the radius of the geometry. Therefore, the shear rate is uniform across the entire gap of the measuring system. This makes the CP system more reliable than parallel plate and cylindrical measuring systems. When placing the sample on the bottom plate, the measurement position (gap between the truncated cone tip and the lower plate) is always fixed in CP measuring

devices. In the current studies on the dense suspension of PNIPAM samples, we used a cone and plate measuring system with the following feature,

cone angle $\varphi = 0.5^{\circ}$; cone radius $R_c = 25$ mm and cone truncation H = 0.051 mm

ii) Parallel plate measuring system

In the case of parallel plate geometry, both the upper and bottom plates are flat. The upper plate is movable, whereas the bottom plate is fixed. The geometry of the plate is determined by the radius, R_c of the plate. Figure 2.13 shows a schematic of the parallel plate measuring system. In a parallel plate measurement method, the gap between parallel plates "h" must be less than the plate radius R_c , i.e. $h \ll R_c$. Unlike in the case of CP measuring system, the shear rate varies throughout the entire gap of the measuring system; hence, shear rate values are inhomogeneous. A fixed gap is not maintained between two parallel plates. Hence, it can be utilized for the measurement of dispersed fluids containing larger particles. In the case of low viscous fluids or larger particle samples, 25mm radius geometry is suggested for the accurate rheological measurements. Generally, it is suggested that, the gap between the parallel plates should be at least 5 times larger than the particle size.

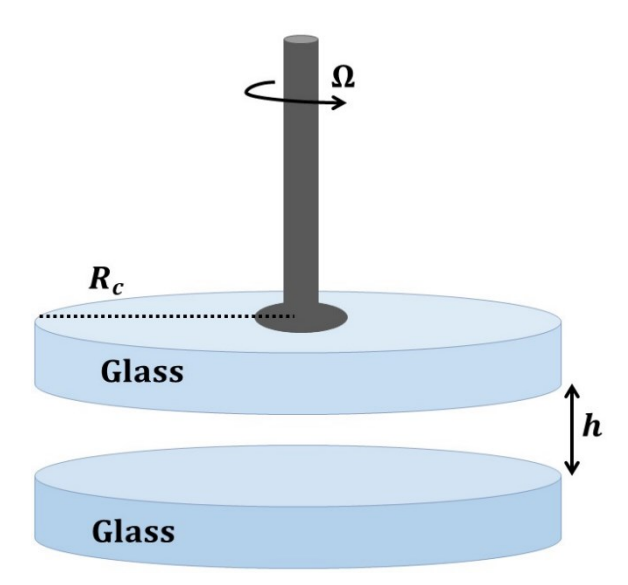


Fig. 2.13. Schematic representation of parallel plate measuring system. The symbols indicate the following parameters: R_c - plate radius, h - gap between top and bottom plates, Ω - angular frequency

We have used a parallel plate measuring system of transparent glasses in the rheo-microscopy experiments on SSY LC samples. Rheo-microscopy allows visual observation of the internal structure of the sample while shearing. A detailed overview of rheo-microscopy is discussed in the following section. For measurements with parallel plates, we have chosen the following features,

Plate radius = 21.5mm and the gap maintained between the plates, h is 0.075mm.

d) Rheo-Microscopy

Rheological measurements, in general, offer data on macroscopic mechanical properties. The mechanical characteristics, on the other hand, can be easily understood by analyzing the microstructures, which can be viewed using a rheo-microscopy technique. The combined investigation of microstructures and mechanical properties always provides a better and comprehensive understanding of the sample [30]. Rheo-microscopy is also very effective for studying complex fluids such as surfactant solutions, polymer solutions, colloidal suspensions, polymer blends and so on. In the present study, we used a rheo-microscopy setup built by Anton Paar, which can be directly connected to the rheometer. The rheo-microscope apparatus includes a CCD camera, a microscopy tube and a long working distance objective [30]. A schematic representation of the rheo-microscopy set up is depicted in Fig. 2.14.

For our measurements, we used a Nikon 20x objective with a numerical aperture (NA) of 0.4. In addition, a parallel plate measuring system having plate radius of 21.5 mm which is made of glass is attached to the rheometer, that ensures the bottom plate (6 mm thickness) to have a good mechanical stability. A polarized light is sent through the objective from the bottom plate onto the sample. An analyzer is installed in the microscope tube before the CCD camera. For focusing, the microscope tube is movable in the y and z directions. A peltier hood is employed to keep the temperature constant across the sample. The maximum temperature that can be sustained in this configuration is around 70°C.

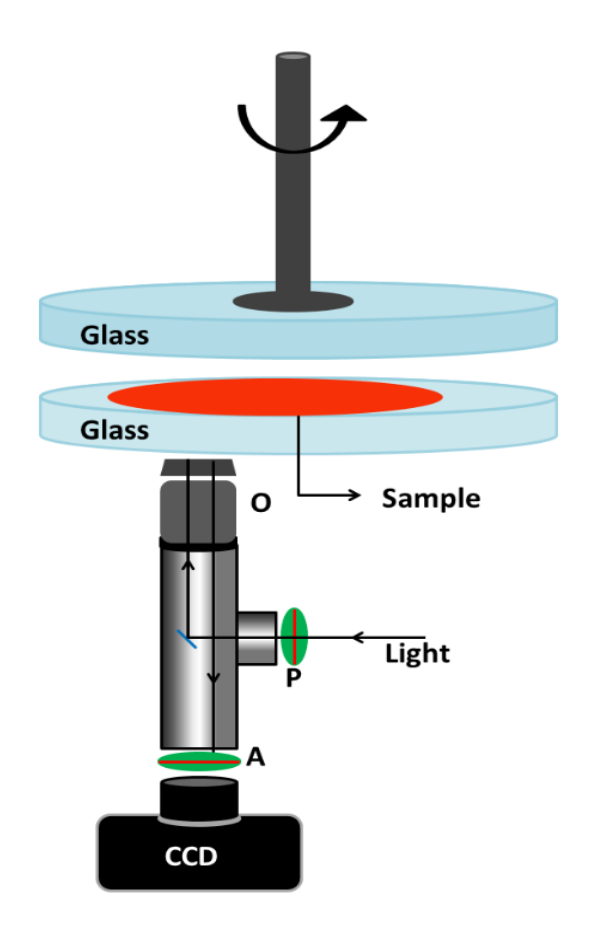


Fig. 2.14. Schematic diagram of *in-situ* rheo-microscopy (RM) setup. O, P and A indicates microscope objective, polarizer and analyzer respectively. The images are captured in the reflection mode.

e) Rheological measurements

In the present studies, the MCR 501 rheometer is set to the strain-controlled mode which can be operated either in oscillation or in rotational manner. Oscillatory shear is commonly employed to characterise viscoelastic materials [29,31]. In this technique, both stress and strain vary cyclically with time and sinusoidal variation is the most typically used (Fig 2.15 (a)). In an oscillatory measurement, an oscillatory strain is applied to the visco-elastic sample and material properties such as storage (elastic) modulus G' and the loss (viscous) modulus G'' are measured [32]. These visco-elastic parameters are usually expressed in complex domain as $G^* = G' + iG''$, where G' is the real part and G'' is the imaginary part of the complex modulus G^* (Fig. 2.15 (b)). As the relative contributions of the viscous and elastic

responses of materials can be quantified, this is the preferred method for characterising viscoelasticity.

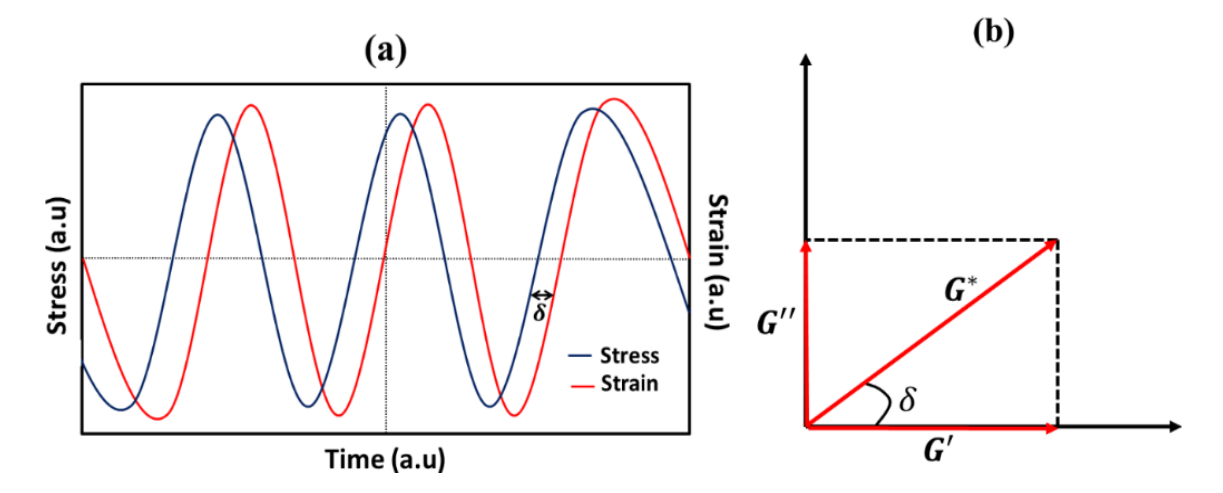


Fig. 2.15. (a) Phase difference, δ between strain (γ) and stress (σ) for a visco-elastic material and (b) vector representation of complex modulus (G^*) for visco-elastic material

Depending upon the amplitude of shear, oscillatory measurements are categorized as i) Small Amplitude Oscillatory Shear measurements (SAOS) and ii) Large Amplitude Oscillatory Shear measurements (LAOS). On the other hand, in rotational experiments shear viscosity is measured with respect to the applied shear rate. The detailed descriptions of these measurements are given below.

i) Small Amplitude Oscillatory Shear (SAOS)

In a dynamic oscillatory shear rheology, a visco-elastic material is allowed to flow by applying a sinusoidal strain of the form $\gamma(t) = \gamma_0 \sin(\omega t)$. Where γ_0 and ω represent the strain amplitude and oscillation frequency respectively. When γ_0 is sufficiently small such that it lies in the linear viscoelastic regime of the material, the stress response of the material is also sinusoidal with the same ω . The stress response of the material is given by:

$$\sigma(t,\omega) = \sigma_0 \sin(\omega t + \delta) \tag{2.39}$$

Where σ_0 represents the stress amplitude and δ represents the phase angle between the stress response and the applied strain. Eq. (2.39) can be divided into two parts that correspond to the in-phase and out-of-phase of the input strain, as shown below.

$$\sigma(t,\omega) = \sigma_0 \cos(\delta) \sin(\omega t) + \sigma_0 \sin(\delta) \cos(\omega t) \tag{2.40}$$

$$\sigma(t,\omega) = \sigma'\sin(\omega t) + \sigma''\cos(\omega t) \tag{2.41}$$

Where σ' represent the in-phase and σ'' represent the out-of-phase components of the stress response.

The linear visco-elastic behavior of a material is characterized by its elastic modulus, $G'(=\sigma'/\gamma_0)$ and viscous modulus, $G''(=\sigma''/\gamma_0)$. Where G' is the in-phase component of the stress response which talks about the elastic property of the material, whereas G'' is the out- of- phase component of the stress response which describes the viscous property of the material. Eq. (2.41) can be expressed as [33]

$$\sigma(t,\omega) = \gamma_0 [G'(\omega)\sin(\omega t) + G''(\omega)\cos(\omega t)] \tag{2.42}$$

In a typical small amplitude oscillatory shear (SAOS) measurement, both these shear moduli (G', G'') remain constant up to a particular limiting value of γ_0 . Below this limit, the measurement is referred to as the linear rheology.

Two common tests performed on linear viscoelastic materials are the strain sweep/amplitude sweep measurement and the frequency sweep measurement. During a strain sweep measurement, the amplitude of the sinusoidal strain is increased and the response in terms of G' and G'' is measured, while the frequency, ω remains constant. If G' > G'', the material is mostly elastic, and if G'' > G', it is predominantly viscous. In highly concentrated suspensions of colloids, the transition from elastic to viscous properties during deformation is attributed to the onset of gelation or structural arrest caused by topological constraints. In a frequency sweep measurement, ω is increased while γ_0 remains constant. Frequency sweep measurements are performed to determine the relaxation times of the material under domain conditions.

ii) Large Amplitude Oscillatory Shear (LAOS)

Although linear visco-elasticity or SAOS test is helpful for determining the relation between the microstructure and the rheological properties of soft matter or complex fluids, it is essential to remember that linear visco-elasticity is only applicable when the total deformation is quite small [34]. However, in most of the cases, the deformation is large and rapid (hence in the non-linear region) therefore linear visco-elastic characterization or SAOS test is insufficient to completely study the sample response when undergoing nonlinear situations. Furthermore, the linear visco-elastic tests (SAOS experiment) employ small strain amplitude and hence this test has a poor resolution in differentiating complex fluids with identical micro structures or molecular structures (e.g., linear or branched polymer topology). Complex fluids exhibiting similar linear rheological behavior may show different non-linear rheological behavior. This indicates that even if rheological experiments are only being employed for material characterization, the linear visco-elastic properties may often be inadequate. Non-linear visco-elastic characterization is expected to provide significantly more insight in differentiating these structural differences. Therefore, it is necessary to investigate the non-linear visco-elastic responses of complex fluids in depth for several reasons.

For large strain amplitude, γ_0 , sample shows non-linear rheological response in the sense that the amplitude of stress, σ_0 not linear to γ_0 . At this moment the non-linear stress response of the sample becomes non-sinusoidal and it contains higher harmonics of the shear moduli G'_n and G''_n , where subscript n stands for n^{th} harmonic. Hence, linear viscoelastic moduli (G', G'') are not adequate to quantify non-linear stress response under LAOS conditions. The stress response for a sinusoidal strain input, $\gamma(t) = \gamma_0 \sin(\omega t)$ with sufficiently large γ_0 can be expressed as,

$$\sigma(t,\omega,\gamma_0) = \gamma_0 \sum_{n=1,3,5\dots} [G'_n(\omega,\gamma_0)\sin(n\omega t) + G''_n(\omega,\gamma_0)\cos(n\omega t)]$$
 (2.43)

As the stress response is symmetric with respect to shear strain or shear rate, *i.e.* the sample response is same in both shear directions, only odd-harmonics are considered in the representation [35]. To describe the non-linear response under LAOS, Lissajous-Bowditch (LB) curves are extensively used. The cyclic variation of stress and strain can be observed by plotting them against each other in the form of LB curves (Fig. 2.16). The LB curves for perfect elastic materials (perfect Hookean solids) are straight lines, since stress and strain are in phase (stress maximum when strain maximum). In contrast, the LB curves for perfect viscous materials (perfect Newtonian fluids) are circles because the stress and strain are out of phase ($\delta = \pi/2$). In the linear regime, for a visco-elastic material, the stress strain LB curve takes the form of an ellipse with a phase lag $0 < \delta < \pi/2$, whereas under LAOS, the LB curve becomes a distorted elliptical loop (Fig. 2.16).

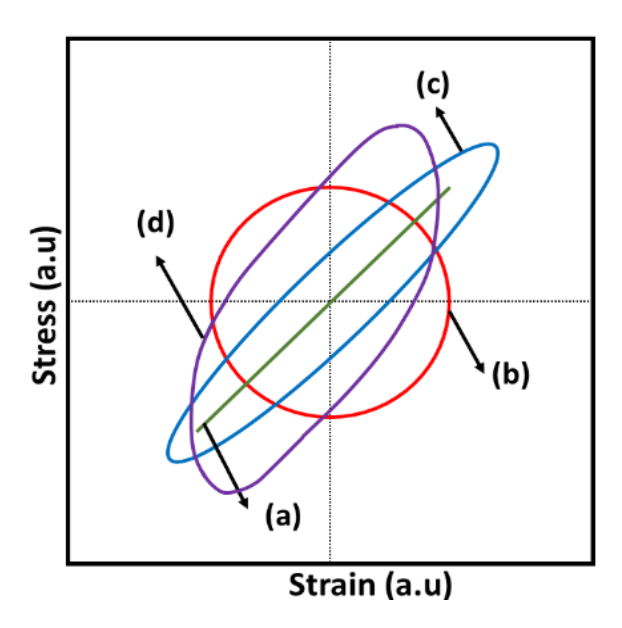


Fig. 2.16. Stress vs strain during a cycle for various materials. (a) elastic material, (b) viscous material, (c) visco-elastic material under SAOS and (d) visco-elastic material under LAOS

iii) Rotational measurements

In addition to the oscillation mode, the rheometer can be operated in rotational mode in order to investigate flow properties such as shear viscosity of the material. Shear viscosity, η is generally defined as the ratio between shear stress, σ and shear rate, $\dot{\gamma}$. It is expressed as,

$$\eta = \frac{\sigma}{\dot{\nu}} \tag{2.44}$$

In general, materials exhibit three different types of steady state flow behavior with respect to shear rate. These are known as Newtonian, shear thickening and shear thinning flow behavior. Newtonian flow behavior occurs when the viscosity remains constant with respect to the shear rate. Variation of viscosity in response to shear rate results in non-Newtonian flow behavior (either shear thickening or shear thinning). Shear-thickening flow occurs when viscosity increases with increasing shear rate, while shear-thinning flow occurs when viscosity falls with increasing shear rate [28,29]. These three basic types of fluid flow behavior are depicted in Fig. 2.17.

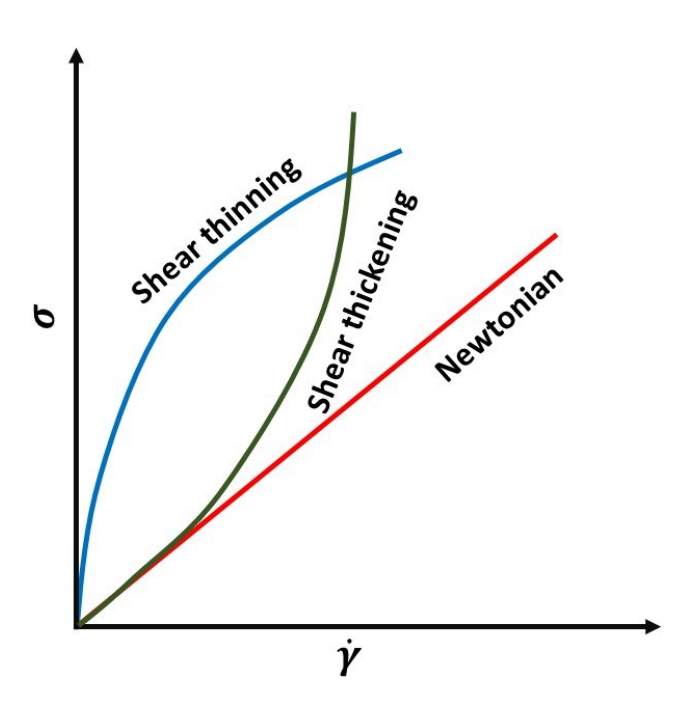


Fig. 2.17. Schematic representation of shear rate vs shear stress plot for different fluids shows Newtonian, shear thickening and shear thinning flow behavior

In a rotational measurement, the upper plate rotates over the sample while the lower plate remains stationary. In the case of cone-plate (CP) geometry (Fig. 2.12), the cone (upper plate) rotates at a rate proportional to the shear rate, $\dot{\gamma}$. The cone angle is kept small ($\varphi = 0.5^{\circ}$) to ensure uniform shear rate [32]. The height between the bottom plate and the cone tip is h. When sample is subjected to shear with an angular speed, Ω , then shear rate (experienced by

suspension) is given by the equation, $\dot{\gamma} = \Omega/\tan(\alpha)$. For small φ , $\dot{\gamma} = \Omega/\varphi$. Therefore, the shear rate depends only on the rotational speed and is constant throughout the sample. The corresponding shear stress, σ can be expressed as $\sigma = 3M_t/(2\pi R_c^3)$ where M_t represents the applied torque for producing the given stress.

2.3.4 Polarizing Optical Microscope (POM)

A polarizing optical microscope (POM) serves as a useful tool for viewing and photographing birefringent materials such as liquid crystals. A POM typically consists of two linear polarizers: one is referred to as the polarizer, and the other as the analyzer. These polarizers are oriented with their polarization axes perpendicular to each other. Further, a rotating sample stage and a microscope objective is aligned along the optical path between these linear polarizers. The light exiting the objective is observed using the eyepiece. A charge-coupled device (CCD) camera can be placed at eyepiece to capture the images. Figure 2.18(a) depicts a schematic representation of the light's propagation through various components of the microscope.

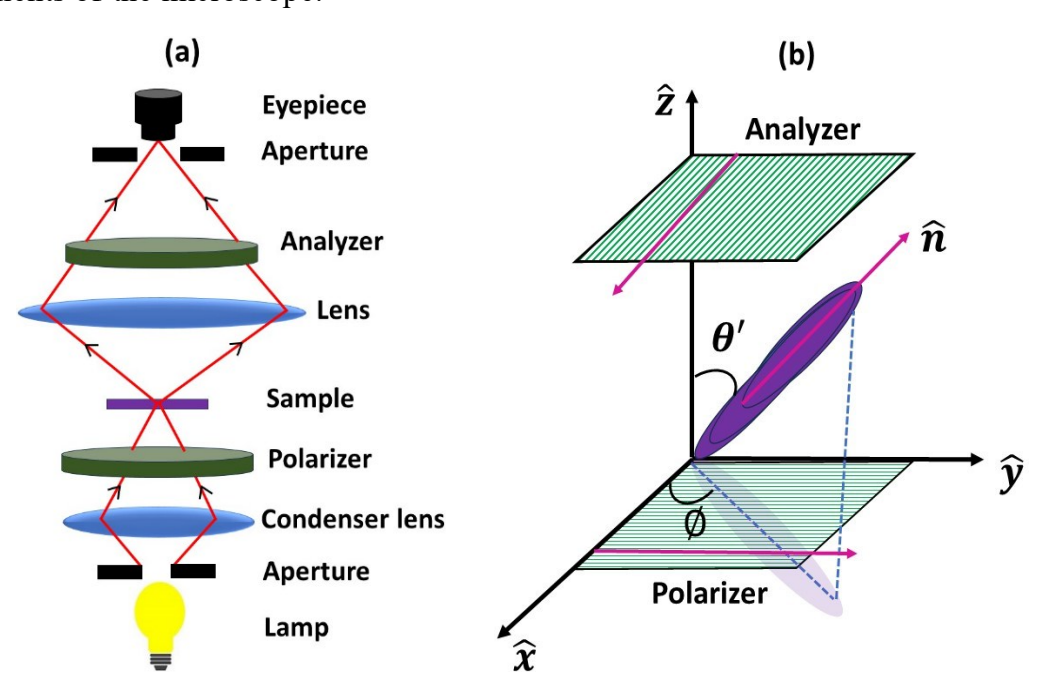


Fig. 2.18. (a) Schematic illustrating the path of light through different components of a POM. (b) Schematic representation of uniaxial LCs between crossed polarizers

In our study, we use Olympus BX51 POM for observing the textures exhibited by liquid crystal (LC) phases. A Köhler illumination unit consists of a xenon lamp is employed for uniformly illuminating the sample. Furthermore, the microscope is equipped with several attachments such as an intensity controller, condenser, color filters, Bertrandlens, and rotating noise piece (Fig. 2.18(b)).

The illumination intensity *I* when a LC sample is viewed under a cross polarizers is given by [36,37],

$$I = I_0 sin^2(2\emptyset) sin^2(\Xi/2)$$
(2.45)

where I_0 denotes the light intensity after passing through the polarizer and \emptyset denotes the angle between director projection on the sample plane (x-y plane) with the analyser axis as seen in Fig.2.7. The phase difference between the extraordinary ray (n_e) and ordinary ray (n_o) is given by \mathcal{Z} .

$$\Xi = \frac{2\pi}{\lambda} \Delta n_{eff} t_c \tag{2.46}$$

Here t_c represents the distance that light travels through a liquid crystal medium (cell thickness) λ denotes the wavelength of the light and Δn_{eff} denotes the effective birefringence. Depending on the value of \mathcal{E} and t_c , LCs exhibit coloured textures and defects.

References

- 1. J. Wu, B. Zhou, and Z. Hu, Phys. Rev. Lett. 90, 048304 (2003).
- J. Brijitta, B. V. R. Tata and T. Kaliyappan, Journal of Nanoscience and Nanotechnology, 9, 5323 (2009).
- 3. R. G. Joshi and B. V. R. Tata, Colloid Polym. Sci., 295, 1671 (2017).
- 4. X. Wu, R. H. Pelton, A. E. Hamielec, D. R. Woods, and W. Mcphee, Colloid Polym. Sci., 272, 467 (1994).
- 5. M. H. Kwok, Z. Li, and T. Ngai, Langmuir, 29, 9581 (2013).

- 6. R. Acciaro, T. Gilanyi, and I. Varga, Langmuir, 27, 7917 (2011).
- 7. K. Kaithakkal Jathavedan, F. Kanheerampockil, and S. Bhat, J. Appl. Polym. Sci., 137, (2020).
- 8. A. K. Arora and R. Kesavamoorthy, Solid state communications, 54, 1047 (1985).
- 9. M. Destribats, M. Eyharts, V. Lapeyre, E. Sellier, I. Varga, V.Ravaine and V. Schmitt, Langmuir, **30**, 1768 (2014).
- 10. L. P. Joshi, Ph.D. thesis, Kent State University, (2009).
- D. J. Edwards, J. W. Jones, O. Lozman, A. P. Ormerod, M. Sintyureva and G. J. T. Tiddy, J. Phys. Chem. B, 112, 14628 (1994).
- 12. H. S. Park, S. W. Kang, L. Tortora, Y. Nastishin, D. Finotello, S. Kumar, and O. D. Lavrentovieh, J. Phys. Chem. B, 112, 16307 (2008).
- 13. A. Yamaguchi, Ph. D thesis, University of Colorado at Boulder, (2015).
- 14. K. H. Yang, J. Appl Phys., 64, 4780 (1988).
- 15. R. Pecora, Dynamic Light Scattering, Plenum Press (1985).
- 16. B. J. Berne and R. Pecora, "dynamic light scattering", A Wieley-Interscience Publication, USA (1976).
- 17. B.V.R. Tata, "Statistical Physics of complex Fluids", edt. S. Maruyama and M. Tokuyama, Tohoku university press, Sendai, Japan (2007).
- 18. B. J. Frisken, Applied Optics, 40, 4087 (2001).
- R. Kimmich, Principles of Soft-Matter Dynamics: Basic Theories, Noninvasive Methods,
 Mesoscopic Aspects (Springer Netherlands, (2012).
- 20. R. Finsy, Advances in Colloid and Interface Science, Elsevier Science B. V., 52, 79 (1994).
- 21. F Gruner and W Lehmann, J. Phys. A: Math. Gen., 13, 2155 (1980).
- 22. C. Urban and P. Schurtenberger, J. Colloid and Interface Science 207, 150 (1998).
- 23. P.N. Pusey, Current Opinion in Colloid & Interface Science, 4, 177 (1999).

- 24. R. G. Joshi, Ph. D thesis, Homi Bhabha National Institute, Mumbai, (2015).
- 25. P.N. Pusey and W. Van Megan, Physica A, 157, 705 (1989).
- 26. D. Karthickeyan, R. G. Joshi and B. V. R. Tata, J. Chem. Phys. 146, 224503 (2017).
- 27. H. Furukawa and S. Hirotsu, j. Phys. Soc. Jpn., 71 (2002).
- 28. R. G. Larson, The Structure and Rheology of Complex Fluids, Oxford University press (1999).
- 29. T. G. Mezger, The rheology handbook. For users of rotational and oscillatory rheometers.

 2nd revised edition, Vincentz Network GmbH & Co. KG, Hannover (2006)
- 30. J. Läuger, P. Heyer, Rheo-Microscopy: Simultaneous structural and rheological information, Annual Transactions of the Nordic Rheology Society, **20**, 179 (2012).
- 31. R. B. Bird and O. Hassager, Dynamics of polymeric liquids. Wiley (1987).
- 32. C. W. Macosko, Rheology Principles Measurements and Applications, Wiley-VCH, New York (1994).
- 33. B. Vishal and P. Ghosh, Korea-Australia Rheology Journal, 30, 147 (2018).
- 34. K. Hyun, M. Wilhelm, C.O. Klein, K. S. Cho, J. G. Nam, K. H. Ahn, S. J. Lee, R. H. Ewoldt and G. H. McKinley, Progress in Polymer Science, 36, 1697 (2011).
- 35. R. H. Ewoldt, G. H. McKinley and A. E. Hosoi, arXiv preprint arXiv:0710.5509 (2007).
- 36. I. Dierking. Textures of Liquid Crystals. Wiley-VCH, Weinheim (2003).
- 37. L. S. Hirst. Fundamentals of Soft Matter Science. 1st ed., CRC Press (Taylor and Francis), London (2012).

YIELDING BEHAVIOR OF DENSE PNIPAM MICROGEL COLLOIDAL GLASSES

In this chapter, we discuss the dynamics and yielding behavior of dense PNIPAM microgel colloidal glasses which were investigated under dynamic light scattering (DLS) and large amplitude oscillatory shear (LAOS) respectively. The role of dangling polymer hairs on the yielding behavior of dense microgel glasses were investigated and energy associated with yielding has been determined. Two types of PNIPAM microgel spherical particles: (i) having core—shell structure with dangling polymer chains and (ii) having only a homogeneous cross-linked core were used for the study.

3.1 Introduction

lassy state is a disordered solid state attained when liquid is quenched or compressed within a time scale smaller than the intrinsic structural relaxation time of the liquid [1,2]. In atomic systems, where structural relaxation times are quite short (10⁻¹² sec), therefore, extremely fast quenching rates are required to obtain glassy state which is practically quite difficult. Whereas, the relaxation time scales of colloidal systems typically ranges from 10⁻⁶ sec to 10³ msec, hence their dynamics can be probed in the real time using dynamic light scattering technique [3]. The investigation of colloidal glasses provides a comprehensive understanding of behaviour of glassy relaxation and aging, which are common to atomic and molecular glass forming systems. Even though there are fundamental distinctions between these two types of glass-forming systems, studying the process of glass

formation in model colloidal systems can shed light on the physics of atomic and molecular glasses [4-6].

The realm of colloidal glass formed by hard spheres stands as a prominent subject of rigorous examination, employing techniques light scattering and rheology. The glassy state in HS suspensions is observed throughout the volume fraction range between ϕ_g = 0.58 and the random close packing limit at ϕ_{rcp} = 0.64 [7-9]. Introducing small amount of non-adsorbing polymer to these HS induces a short-range depletion attraction between the colloidal spheres, ultimately resulting in a kinetically arrested state recognized as the attractive glass. For the glassy state, the dynamics at longer time slows down drastically [10,11]. Slowing down of the particle dynamics at long times in hard sphere suspensions as the system approaches the glass transition, is attributed to the trapping of particles within cages formed by their near neighbor particles, leading to the kinetically arrested state [10]. Even before the liquid transforms into glass, the particles begin to experience the effect of the cage when it is in a supercooled liquid state. The particle motion in the supercooled liquid is diffusive both at short times as well as long times and is characterized by long and short time diffusion coefficients D_L and D_S respectively. However, dynamics becomes sub-diffusive during intermediate times due to the cage effect. Eventually, at long times, dynamics become diffusive as the particles escape from their cages. Typical behavior of the particle's mean square displacement (MSD) is depicted in Fig. 1.6 (chapter1, section 1.1.5). The structural relaxation in the super-cooled liquid occurs in two steps. The first step, known as fast or beta relaxation, happens at short times (due to the intra-cage dynamics of the particles) whereas, second step, known as slow or alpha relaxation, occurs at long times (when particles escape their cages). As the system approaches the glass transition (ie. with increase in ϕ), the cages of nearby particles become increasingly rigid, leading to an increase in the alpha relaxation time. This suppresses the long time diffusion of particles. While long time dynamics (alpha relaxation) of hard sphere colloidal

particles in the glassy state is arrested, short time dynamics (beta relaxation) persists with diffusive particle motion [10].

In contrast to HS suspensions, PNIPAM microgel suspensions can be densely packed beyond the typical close packed volume fraction of 0.64 due to their compressible [12]. In these dense conditions, it has been observed that PNIPAM microgel suspensions having size polydispersity (SPD) of 10% freeze into a kinetically arrested glassy state. Joshi et al. reported sub-diffusive dynamics at short times from the DLS measurements [13] and two-step yielding in rheological measurements [14,15] on dense suspensions of PNIPAM microgels. Furthermore, Jathavedan et al. also investigated the yielding behavior of dense suspensions of PNIPAM microgels having core-shell morphology and reported two-step yielding [16]. It is worth noting that the occurrence of two-step yielding is typically associated with colloidal glasses featuring attractive interactions. However, it has not been observed in repulsive colloidal systems such as HS glasses and glasses of like-charged colloids. PNIPAM microgel soft particles exhibit repulsive interactions (MH potential) below VPT [17]. Although there exist repulsive interactions, dense PNIPAM suspensions display two-step yielding bevaviour. This intriguing observation is specific to these soft deformable systems, and the underlying yielding mechanism incompletely comprehended. The primary focus of this chapter is to provide a comprehensive understanding of the influence of dangling polymer chains in the yielding mechanism of PNIPAM suspensions in their glassy state under dense conditions. The yielding behavior or the non-linear rheological behavior of dense PNIPAM microgel colloidal glasses has been investigated by performing large amplitude oscillatory shear (LAOS) measurements.

This chapter delves into the results of both linear and non-linear rheological investigations conducted on concentrated suspensions of two types of PNIPAM microgel spheres, viz., core–shell type having dangling polymer chains, referred to as CS-PNIPAM

spheres, and the other type being spheres having a homogeneous core and without dangling polymer chains, identified as HC-PNIPAM particles. Additionally, we have performed large amplitude oscillatory shear (LAOS) measurements on concentrated suspensions comprising of both HC and CS type PNIPAM microgel spheres. CS-PNIPAM microgel glass exhibits two-step yielding process (characterized by two peaks in the viscous modulus (G'')) similar to what was observed in attractive glasses. Whereas, HC-PNIPAM microgel glass exhibits one step yielding (characterized by single peak in the viscous modulus (G'')) similar to that was exhibited by repulsive colloidal glasses. Additionally, we studied the effect of temperature on the yielding behavior of CS-PNIPAM and HC-PNIPAM microgel glasses. It was observed that, upon increasing the temperature both the CS-PNIPAM and HC-PNIPAM microgel glasses were transformed into the liquid state which is identified as the disappearance of their respective peak(s) in G'' at the higher temperature.

Furthermore, the LAOS responses have been depicted in the form of Lissajous-Bowditch (LB) curves, wherein oscillating stress is graphed against the corresponding strain. LB curves serve as a valuable tool for visualizing and interpreting viscoelastic non-linearities in a broader context. We adopted the scheme proposed by Rogers *et al.* [18] to analyze the time-dependent stress—strain data. This approach allowed us to gain deeper insight into the processes such as elastic straining, yielding, flow, and dissipation. The rheological studies presented here offer unambiguous evidence for the presence of entanglements between dangling polymer chains between nearest neighbor microgel particles in the glassy state of dense suspensions of CS-PNIPAM particles.

3.2 Experimental Details

With an aim to elucidate the role of dangling polymer chains on the yielding characteristics of dense/ highly concentrated microgel suspensions in their glassy state, we

have synthesized two types (one with core-shell type with dangling chains and other one with homogeneous core) PNIPAM microgels using free radical precipitation polymerization method [19] in aqueous medium. The synthesis procedure is provided in chapter 2. The measured average hydrodynamic diameter d_h and the size polydispersity (SPD) of core-shell and homogeneous core microgel particles using DLS technique described in Chapter 2 are given in Table3.1. Dense PNIPAM microgel glasses were prepared by concentrating the purified microgel suspensions of core-shell and homogeneous core particles as described in chapter 2. They are labelled as CS-PNIPAM and HC-PNIPAM respectively. The volume fractions of CS-PNIPAM and HC-PNIPAM were determined to be 0.80 and 0.89 (chapter: 2, section: 2.1.4) respectively and they were used for the current studies.

Sample	CS-PNIPAM	HC-PNIPAM
Hydrodynamic diameter, d_h (at $T = 20^{\circ}$ C)	270 nm	1480 nm
SPD	11%	13%
Volume fraction, ϕ	0.80	0.89

Table 3.1. Sample details of CS-PNIPAM and HC-PNIPAM dense microgel suspensions

3.1.1. 3D Dynamic Light Scattering (3D-DLS) measurements

Dense suspensions of HC-PNIPAM and CS-PNIPAM microgel particles at $T=20^{\circ}\text{C}$ appear turbid; therefore, we utilized a 3D-DLS instrument (M/s LS Instruments AG, Fribourg, Switzerland) which employs cross-correlation technique using two light detectors to determine single-particle dynamics in concentrated suspensions of CS-PNIPAM and HC-PNIPAM in their glassy state. Experimental procedures are reported in our previously published paper [14, 20]. The 3D-DLS instrument is equipped with 633 nm He-Ne laser and two avalanche photo diodes (APD) as detectors and a multi-tau correlator, which can measure particle dynamics spanning over 11 orders of magnitude in time starting from 12 ns. The

intensity-intensity cross-correlation function $g_{12}^2(q,t)$ measured using 3D-DLS is given by Eq. 2.18. Here q denotes the scattering wave vector. Since colloidal glasses are non-ergodic systems, we obtain the field-field correlation function, f(q,t) from measured $g_{12}^{(2)}(q,t)$ by performing the non-ergodic analysis as described in chapter 2, section (2.3.1) [14,20-22]. The f(q,t), thus measured, was then used to calculate the mean square displacement (MSD) $<\Delta r^2(t)>$ of the particle using the relation [23] given in Eq. (1.11). The MSD as a function of time is calculated using Eq. (2.15) and analyzed for characterizing the particle dynamics by fitting MSD versus t to the power law given by the Eq. (1.11). The nature of particle dynamics in the colloidal glassy state of CS-PNIPAM and HC-PNIPAM microgel particles is measured by performing 3D-DLS measurements, and the results are reported in the later section of this chapter.

3.1.2. Linear Rheology and Large Amplitude Oscillatory Shear (LAOS) measurements

Rheological experiments have been performed using an MCR 501 rheometer (M/s Anton Paar GmbH, Germany). A cone and plate geometry having a diameter of 50 mm, cone angle of 0.5° and cone and plate gap of $51~\mu$ m, has been used for all the measurements. After mounting the sample, the exposed area around cone and plate was sealed with silicone oil (viscosity~99cp) to prevent the evaporation of water during the measurements. Prior to each measurement, the sample temperature was raised to 35° C (*i.e.* above VPT) to eliminate the shear history. Subsequently, the sample was then cooled back to the desired measurement temperature ($20 \pm 0.1^{\circ}$ C). Upon cooling, a waiting time of 15 minutes was implemented before each measurement in order to achieve complete recovery of viscoelasticity of the samples. We performed both linear and non-linear rheological tests on these dense suspensions of CS-PNIPAM and HC-PNIPAM samples and the results are presented here. In a linear rheological experiment, the sample is subjected to a variable oscillation frequency

denoted as ω while maintaining a constant small value of amplitude of oscillatory strain denoted as γ_0 (=1%). The resulting oscillatory stress amplitude, σ_0 is quantified in terms of storage modulus, G' and viscous modulus, G''. Similarly, in a non-linear rheological experiment, variable amplitude of oscillatory strain, γ_0 is applied to the sample while maintaining the oscillation frequency, ω constant, and the resulting oscillatory stress amplitude, σ_0 is quantified. The stress, $\sigma(t)$ and strain, $\gamma(t)$ are connected by the relation $\sigma^*(t) = G^*\gamma^*(t)$ (* represents complex quantities). Here G^* represents the complex shear modulus which is defined as $G^* = G' + iG''$. The damping factor is defined as $\tan \delta(\omega) = \frac{G''(\omega)}{G'(\omega)}$ and it can be used for characterizing the viscoelastic behavior as a function of driving parameter. The non-linear rheological measurements on hard sphere colloidal glasses exhibit a plateau in G' and G'' for low γ_0 . However, beyond a critical value of γ_0 (called yield point), hard-sphere glasses exhibit yielding by showing monotonic decrease in G' and a peak in G''. The peak in G'' is a signature of many soft glassy materials [24,25,26].

Non-linear rheology is a convenient method to understand the yielding behavior of viscoelastic samples especially the glass samples [15]. Non-linear rheological measurements are performed by means of Large Amplitude Oscillatory Shear, LAOS [27]. LAOS produces a non-sinusoidal stress response against the explicit sinusoidal driving force. In the non-linear regime, differential equations linking the stress and strain could still be linear, but the coefficients could be amplitude-dependent [28,29]. Graphical representations such as Lissajous-Bowditch (LB) curves have been employed to describe the non-linear response which shows non-elliptic loop of stress curve. A popular method for analyzing LAOS data is the Fourier-transform method, which utilizes the relative intensities of higher harmonics of dynamic moduli and can serve as a measure of non-linearity [30,31]. Even though the Fourier transform (FT) rheology gives quantitative information of non-linear responses, it is not easy to convert the information from FT to mechanical terminology. This limitation of FT rheology

is resolved in the new analysis scheme introduced by Rogers *et al*. [18], where the deformation cycle is interpreted in terms of straining, yielding, flow, and structural rejuvenation. This decomposition offers insight into the physics of yielding and flow, and allows determination of significant parameters such as the local cage modulus, static and dynamic yield stresses [18,32]. The initial elastic straining during intracycle shearing is characterized by the local cage modulus (G_{cage}), which can be defined as the instantaneous slope of the elastic Lissajous-Bowditch curve at zero stress, σ .

$$G_{cage} = \frac{d\sigma}{d\gamma}\Big|_{\sigma=0} \tag{3.1}$$

The cage modulus (G_{cage}) together with the shear moduli (G', G'') as a function of strain amplitude, γ_0 is shown in Fig. 3.4. (section 3.3.2).

The process of yielding is associated with the LAOS parameters, static and dynamic yield stress. Static yield stress, σ_{ys} has been determined at the maximum stress overshoot, and dynamic yield stress, σ_{yd} at the point of zero instantaneous shear rate. The system will be more dissipative after yielding. The dissipated energy, E_D per unit volume during one complete oscillatory strain can be expressed as

$$E_D = \oint \sigma \ d\gamma \tag{3.2}$$

K. van der Vaart *et al.* [32] constitute a direct relation between dissipation energy and LAOS parameters as,

$$E_D = \pi \sigma_0 \, \gamma_0 - \sigma_0 \, (\sigma_{yd} / G_{cage}) \tag{3.3}$$

With an aim to calculate the energy associated with yielding, we have taken $\pi \sigma_0 \gamma_0$ as the total mechanical energy supplied to the system, E_T and σ_0 (σ_{yd}/G_{cage}) as the yielding energy, E_Y . The energy relation can be therefore written as follows,

$$E_T = E_Y + E_D \tag{3.4}$$

The yielding energy, E_Y for dense samples of CS-PNIPAM and HC-PNIPAM suspensions is compared in light of entanglement of dangling polymer chains between the nearest neighbor particles, in the later section of this chapter.

3.3. Results and Discussions

3.3.1. Characterization of glassy state

The dense samples of volume fractions listed in Table 1 did not show iridescence even when kept undisturbed for several days at temperature $T = 20 \pm 0.5$ °C, implying they are disordered state which could be glass-like or liquid-like. In order to know these dense disordered suspensions are solid like or not, we have measured elastic modulus, G' and viscous modulus, G'' by performing linear rheological measurements over a wide frequency range spanning over $\omega = 1 \text{ rad/s to } 70 \text{ rad/s}$, while keeping the amplitude of oscillation, γ_0 at 10% and the temperature at 20°C. Frequency dependence of G' and G'' for dense samples of CS-PNIPAM and HC-PNIPAM are shown in Fig. 3.1. Notice from Fig. 3.1(a) and Fig. 3.1(b) that G' is distinctly higher as compared to G'' and is independent of ω implying that at T =

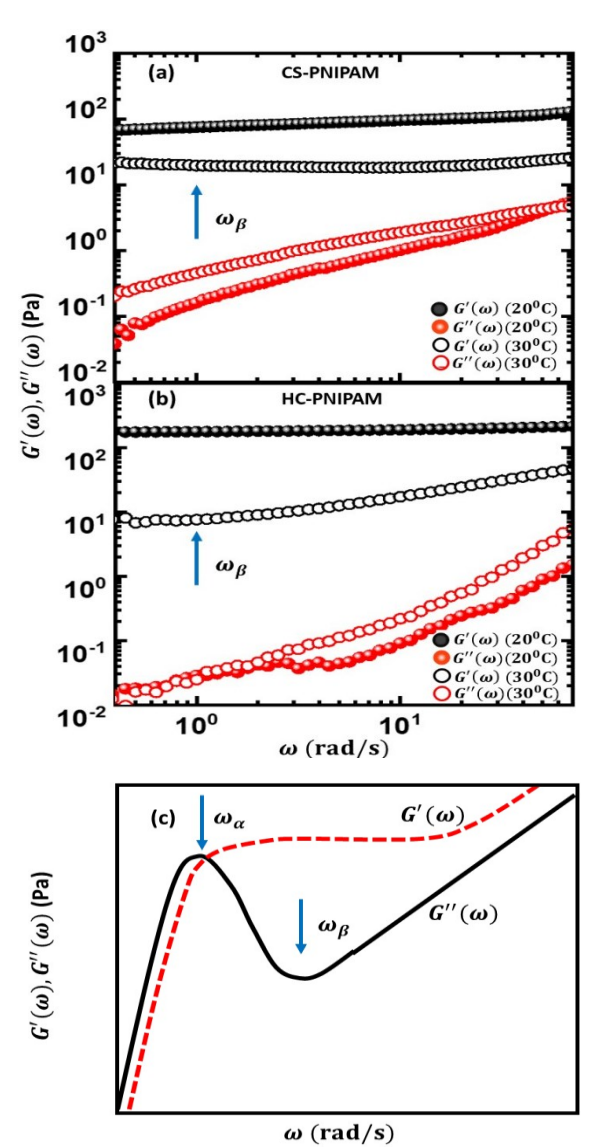


Fig. 3.1 Linear viscoelastic response of glass samples (a) CS-PNIPAM and (b) HC-PNIPAM in their glassy state ($\gamma_0 = 10\%$). Arrows represent the approximate position of the minimum in G'' corresponding to the beta relaxation frequency, ω_{β} . (c) Schematic illustrating the typical linear viscoelastic response of colloidal glasses. ω_{α} and ω_{β} represent the alpha and beta relaxation frequencies of colloidal glass.

20°C both samples are solid-like and are structurally disordered (no iridescence), hence are

identified to be in their glassy-state [14]. Typical linear rheological response of a repulsive colloidal glass over a wide range of ω is now well known [24,25,33] and is shown schematically in Fig. 3.1(c). Notice that G' increases at low ω , exhibits plateau at intermediate ω and increases once again at high ω . On the other hand, G" exhibits a peak at frequency, ω_{α} followed by a minimum at frequency ω_{β} (shown in Fig. 3.1(c)). Here, ω_{α} and ω_{β} corresponds to slow (also known as alpha) and fast (also known as beta) relaxation time scales respectively of the colloidal glass [24,34]. α -relaxation arises due to the escape of the particle from the cage of neighboring particles [34] and β -relaxation occurs due to the rattling of the particle within the cage formed by nearest neighbors [4,35]. G' crosses at the peak of G'' and below this crossing, sample exhibits liquid-like behavior as G'' > G'. Beyond the cross over point (i.e. beyond the peak of G'') sample turns solid-like with elastic modulus G' being more than the loss modulus G''. Joshi et al.'s [14] DLS measurements have shown that time scales of alpha relaxation in dense PNIPAM microgel glasses are of the order of 100s, hence ω_{α} is expected to be very small and falls outside the experimental measurement window of ω (Fig. 3.1) Thus, the frequency regime over which G' and G'' are probed in our experiments (Fig. 3.1(a) and Fig. 3.1(b)) includes minimum in G'' occurring around 1 rad/s which is marked with vertical arrow in Fig. 3.1. It can be seen from Fig. 3.1(a) and Fig. 3.1(b) that for both glassy samples, G' exhibits plateau at low ω and G'' exhibits minimum (indicated by arrow in Fig. 3.1). These observations suggest that the linear rheological behavior of PNIPAM microgel glasses observed at T = 20°C is similar to that of repulsive colloidal glasses reported in the literature [24,36].

Upon heating these microgel glasses to 30° C, G' is found to be lesser than G'' for both the samples (Fig. 3.1(a) and 3.1(b)) suggesting they have tuned liquid-like. This implies that microgel glasses undergo glass to liquid transition (melting of microgel glass) beyond a certain temperature. In order to identify the glass transition temperature, T_g , (the temperature

at which a colloidal glass melts into a colloidal liquid upon heating or liquid solidifies into a glassy state upon cooling), we determined the damping factor, as defined above, at γ_0 = 10% as a function of temperature and is depicted in Fig. 3.2. As expected, the change in slope at a specific value of T is a strong indication of change in state from glassy to liquid-like and denoted as the glass transition temperature T_g . It can be seen from Fig. 3.2 that both CS-PNIPAM and HC-PNIPAM dense microgel glasses exhibit a change in slope, at temperatures 26°C and 25.5°C respectively, suggesting the occurrence of glass transition at temperatures 26°C and 25.5°C, in dense microgel glasses of CS-PNIPAM and HC-PNIPAM samples with volume fractions listed in Table 3.1.

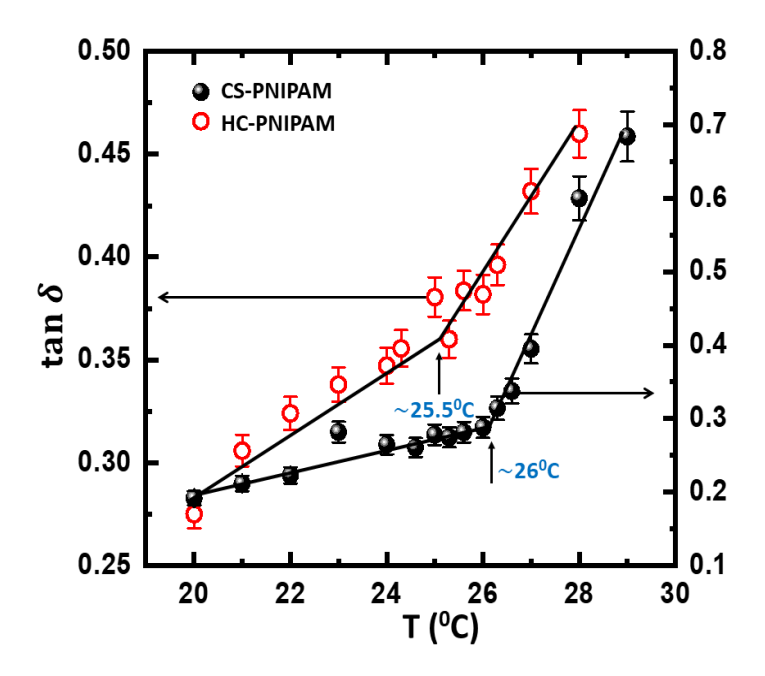


Fig. 3.2. $\tan \delta$ versus T for a fixed strain, $\gamma_0 = 10\%$ for dense glass samples of CS-PNIPAM (closed circle) and HC-PNIPAM (open circle) microgel particles. Left and right arrows indicate $\tan \delta$ (Y-axis) for HC-PNIPAM and CS-PNIPAM respectively.

3.3.2. Dynamical Strain sweep studies on dense PNIPAM microgel glasses across glass transition

Having characterized the dense samples of CS-PNIPAM and HC-PNIPAM suspensions for their glassy behavior at 20°C and for their glass transition temperatures upon heating, we further subjected these dense suspensions to dynamical strain sweep (DSS) measurements

with an aim to understand their yielding behavior. Experimental results reported in the manuscript have been repeated a minimum of three times. The results reported are completely reproducible. The error bars are not shown in some figures as they are smaller than the size of the symbols used in the figures. The strain amplitude, γ_0 is varied over a wide range from 1% to 1000% while keeping ω fixed at 10 rad/sec and temperature at 20°C. The variation of G' and G'' as function of G' as shown in Fig. 3.3. Note that G' is higher than G'' for both glassy samples up to $\gamma_0 = 20\%$ and exhibit yielding beyond this value of γ_0 . Further, notice from Fig. 3.3, in addition to monotonic decrease of G' with increase in γ_0 beyond 20%, the loss

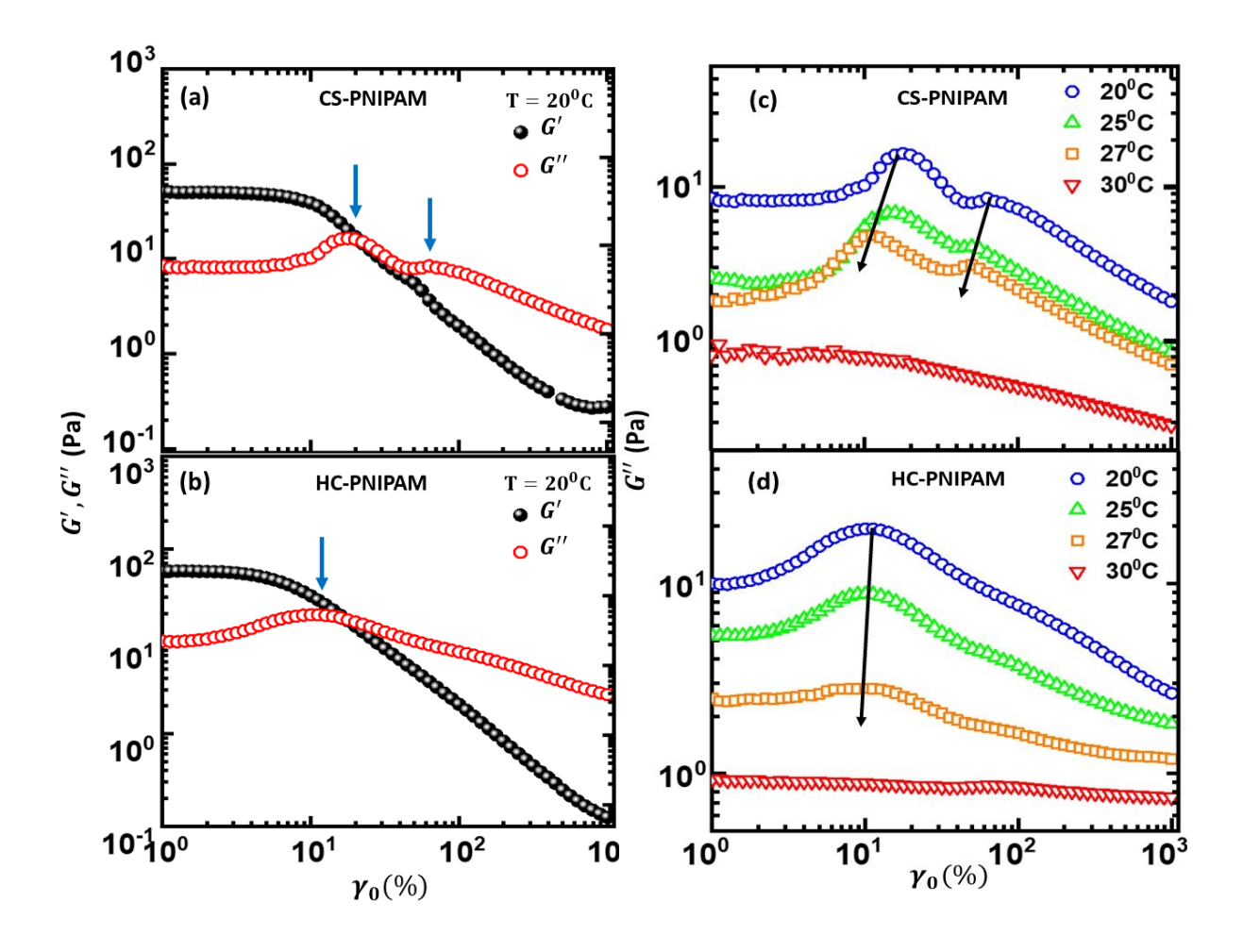


Fig. 3.3. Yielding behavior of samples CS-PNIPAM and HC-PNIPAM in their glassy state. (a) Two peaks (marked with arrows) in $G''(\omega)$ indicate two-step yielding in sample CS-PNIPAM at $T=20^{0}$ C. (b) Single peak in $G''(\omega)$ indicated yielding in single step in HC-PNIPAM sample at $T=20^{0}$ C. Variation of G'' as a function of γ_{0} with increasing temperature, T for samples (c) CS-PNIPAM and (d) HC-PNIPAM in their glassy state at $\omega=10$ rad/sec. Arrows indicate the evolution of peak(s) in G'' with increasing temperature.

modulus *G*" for sample CS-PNIPAM exhibited two-peak yielding (*i.e.* two peaks in *G*", Fig. 3.3(a)), referred to as two-step yielding. This observation is consistent with reported by Joshi *et al.* [14]. Whereas HC-PNIPAM glassy samples showed a single peak, referred to as single step yielding (Fig. 3.3(b)) similar that observed in hard-sphere repulsive glasses.

During yielding, the cages are assumed to break beyond a particular strain called yield strain and reform at zero instantaneous shear rate. G_{cage} along with the G' and G'' as a function of strain amplitude, γ_0 is shown in Fig. 3.4. In the linear regime, both overlap and in the non-linear regime, G_{cage} sustains. This indicates G_{cage} dominates the suspension rheology.

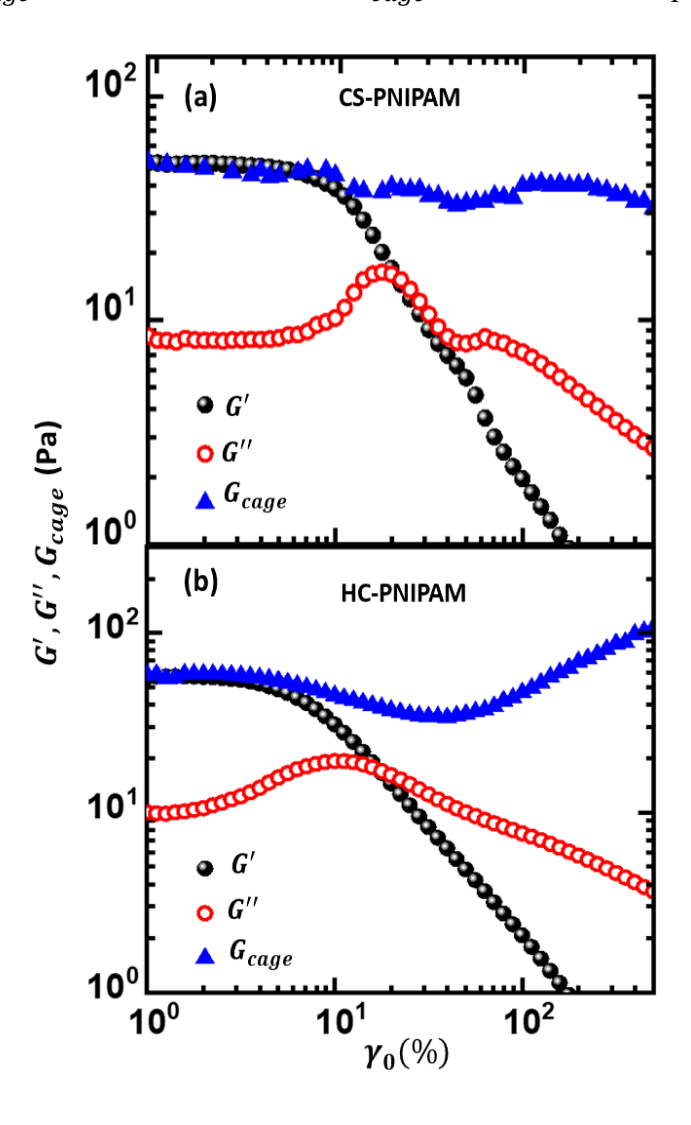


Fig. 3.4. The apparent cage modulus (G_{cage}) as a function of strain amplitude, γ_0 overlaid on the shear moduli $(G', G^{"})$ data of Fig. 3.3 for (a) CS-PNIPAM and (b) HC-PNIPAM. In the linear regime, G_{cage} coincides with G' whereas, it sustains for larger values of γ_0 .

The schematic illustrations of two-step yielding in CS-PNIPAM and single step yielding in HC-PNIPAM samples are shown in Fig 3.5.

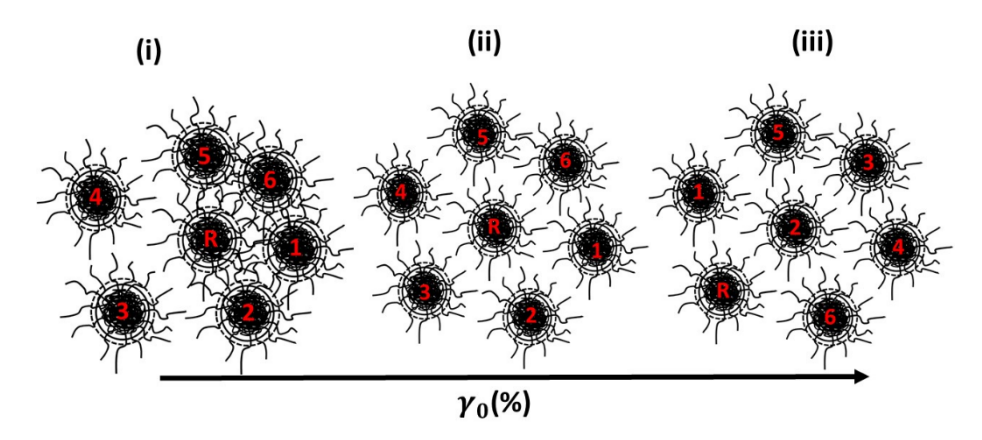


Fig. 3.5(a). State (i) represents the unreformed state configuration of CS-PNIPAM microgel glass with R as reference particle having entangled neighbors 1, 2, 5 and 6 and topological neighbors 1–6. State (ii) shows that, upon application of lower yield strain, entanglements with 1, 2, 5 and 6 are broken leading to first peak in G''. State (iii) shows that, upon application of higher yield strain, topological neighbors of R changes due to cage breaking, which leads to second peak in G''. Arrow indicates the increasing direction of strain.

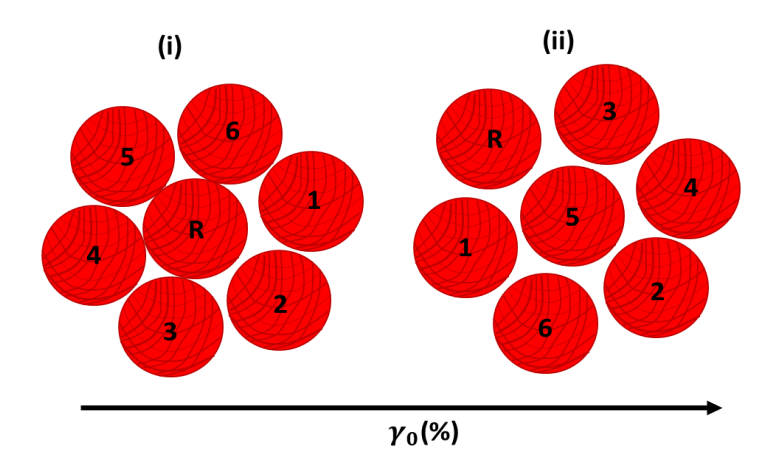


Fig. 3.5(b). State (i) represents the unreformed state configuration of HC-PNIPAM microgel glass with R as reference particle having topological neighbors 1-6. State (ii) shows that, upon application of yield strain, topological neighbors of R changes due to cage breaking, which leads to a peak in G''. Arrow indicates the increasing direction of strain.

Well prior to the study of yielding in soft PNIPAM microgel glass, Pham *et al.* [37] reported two-step yielding in the case of attractive colloidal glass (AG) with volume fraction $\phi = 0.60$, formed by sterically stabilized poly(methyl methacrylate) (PMMA) microspheres dispersed in cis-decalin with added non-adsorbing polystyrene polymer (See Fig. 1.9(chapter 1, section 1.1.8). Addition of non-adsorbing polymer is responsible for the depletion attraction

between PMMA spheres. Suspensions of PMMA spheres serve as a repulsive hard sphere system without the addition of non-adsorbing polymer. Pham $et\ al$. reported single step (*i.e.* single peak in G'') yielding in hard sphere glass (RG), which is shown in Fig. 1.7 (chapter 1, section 1.1.7). Despite interaction potential between CS-PNIPAM microgel particles being repulsive [38], the suspension in its glassy state exhibits two–step yielding similar to that of attractive glass. We believe this is due to the entanglement of dangling polymer chains between shells of the neighboring PNIPAM microgel particles which are known to have a core-shell structure [39]. In order to confirm that the entanglement of dangling polymer chains between shells of the neighboring CS-PNIPAM particles occurs under dense conditions, we performed 3D DLS measurements (as described in section 3.1.1) on the glassy sample at $q = 2.54 \times 10^5$ cm⁻¹ and keeping $T = 20^{\circ}$ C. MSD obtained from the measured field correlation function as function of delay time t is shown in Fig. 3.6(a).

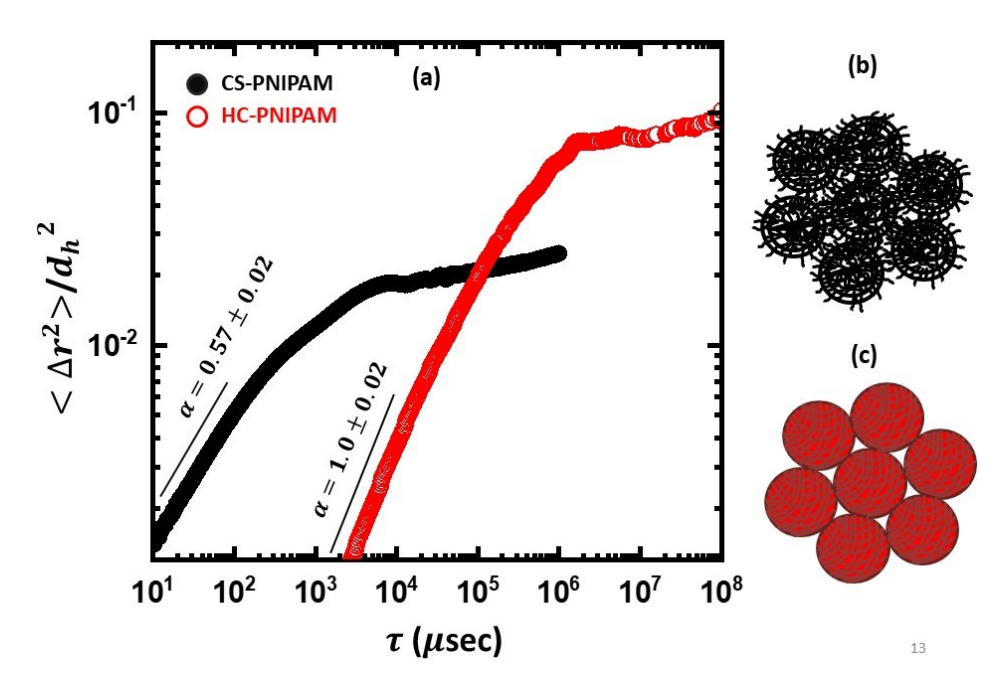


Fig. 3.6(a). Mean square displacement, $<\Delta r^2(t)>$ in units of average hydrodynamic diameter, d_h versus delay time, τ showing particle dynamics in CS-PNIPAM (closed circle) and HC-PNIPAM (open circle) in their colloidal glassy state ($T=20~^{\circ}\text{C}$). Lines represent the fit to Eq. 1.11 at the short time regime. Up and down arrows indicate the time-scale (x-axis) for microgel glasses of CS-PNIPAM and HC-PNIPAM particles respectively. Schematic (b) represents the cage of CS-PNIPAM particles with entanglements of dangling chains between nearest neighbor particles in the glassy state and schematic (c) represents the cage of HC-PNIPAM particles in its glassy state without the entanglements as there are no dangling polymer chains.

We notice that at short times the particle motion is sub-diffusive clearly providing evidence for the existence of entanglements of dangling polymer chains between nearest neighbors (see the schematic shown in Fig. 3.6(b)) of CS-PNIPAM particles under overpacked ($\phi > 0.68$) conditions. It may be mentioned here that Joshi *et al.* also have reported similar observations (two-step yielding and sub-diffusive behavior at small times) in PNIPAM microgel glasses under dense conditions [14]. Rheological measurements on same samples by Joshi *et al.* have showed two-step yielding [14] despite particle interactions being repulsive.

Unlike CS-PNIPAM microgel particles, HC-PNIPAM particles are known to be homogeneous in its polymer network and free from dangling chains on the surface, hence in the over-packed colloidal glassy state rheological measurements are expected to show only single step and diffusive behavior at small time-scales in the MSD versus delay time obtained from 3D DLS measurements. We confirm this by synthesizing HC-PNIPAM microgel particles with homogeneous core by adopting the synthesis procedure reported by Kwok et al. [40]. The synthesis procedure is discussed in experimental methods section in detail [40]. It can be seen from Fig. 3.3(b) that microgel particles with homogeneous core showed only single step yielding and MSD obtained from 3D DLS measurements carried out at q = 1.01 $\times 10^5$ cm⁻¹ and T = 20°C, showed diffusive behavior at short times (see Fig. 3.6(a), time exponent $\alpha \sim 1.0$), clearly providing evidence that under over-packed conditions the glassy state of HC-PNIPAM particles differ from the glassy state of CS-PNIPAM microgel particles in their rheological behavior (i.e. one step-yielding versus two-step yielding) as well as in their MSD behavior at short times i.e. diffusive versus sub-diffusive behavior of particle dynamics. Thus, rheological measurements together with 3D DLS measurements on the glassy state of HC-PNIPAM and CS-PNIPAM microgel particles clearly reveal that dangling polymer chains that exist in CS-PNIPAM microgel particles undergo entanglements with its

nearest neighbors and are responsible for the observed two–step yielding which otherwise was reported only in attractive colloidal glasses [37].

Since both CS-PNIPAM and HC-PNIPAM are thermo-responsive and undergo reduction in its size upon increasing the temperature, the volume occupied by the particles comes down at elevated temperatures leading to the melting of over-packed microgel glass into relatively less dense colloidal liquid. Fig. 3.3(c) and (d) describe the G'' versus γ_0 behavior of CS-PNIPAM and HC-PNIPAM microgel glasses upon increasing the temperature beyond their glass transition temperature. The deswelling of CS-PNIPAM particles and the resulting reduction volume fraction leads to the disappearance of entanglements between the nearest-neighbor particles hence disappearance of two-peak structure in G'' in the colloidal liquid-state which can be seen in Fig. 3.3(c). Similarly, the single peak in G'' also disappears (see Fig. 3.3(d)) once the microgel glass of HC-PNIPAM particles melts into its colloidal liquid state when temperature is raised beyond their glass transition temperature. Thus, the rheological behavior of dense suspensions of CS-PNIPAM and HC-PNIPAM particles in their liquid-like state appears similar, but behave quite differently in their microgel glass state.

3.3.3. LAOS behavior and Lissajous curves

To gain detailed insight into the yielding behavior and energy associated with the yielding of dense PNIPAM microgel suspensions, we investigated the raw data of stress versus strain acquired at an angular frequency of 10 rad/s during an oscillatory cycle at a given strain amplitude. The raw stress and strain data exported from the rheometer software was smoothened by MATLAB® using a freely available LAOS data analysis package, MITlaos (McKinley's group; http://web.mit.edu/nnf/). The stress versus strain thus obtained for dense CS-PNIPAM and HC-PNIPAM suspensions with parameters listed in Table 3.1 are represented in the form of Lissajous-Bowditch (LB) curves and are shown in Fig. 3.7. Figure 3.7(a) to (c) show results for CS-PNIPAM glass sample, and Fig. 3.7(d) to (f) depict results

for HC-PNIPAM glass, with increasing strain amplitude from left to right. In both cases, at small strain amplitude LB curve is an ellipse(Fig. 3.7(a) and (d)) indicating linear stress response of the samples. As strain amplitude increases beyond the linear regime ($i.e.\gamma_0 > 5\%$), the LB curves for both CS-PNIPAM and HC-PNIPAM become distorted from the elliptical nature (see Fig. 3.7(b) to (c) and (e) to (f)). These distorted LB curves indicate the presence of higher harmonics of the moduli (G', G'') and represent the non-linear stress response of PNIPAM dense suspensions. Since the area enclosed by the LB curve gives the dissipation in the viscoelastic system, it can be inferred from Fig. 3.7 that, both the samples dissipate more in the non-linear regime than in the linear regime. For the further investigation of the non-linear viscoelastic behavior of dense PNIPAM microgel suspensions, we adopted the analysis proposed by Rogers *et al.* [18]. This approach provides a framework to analyse the intracycle

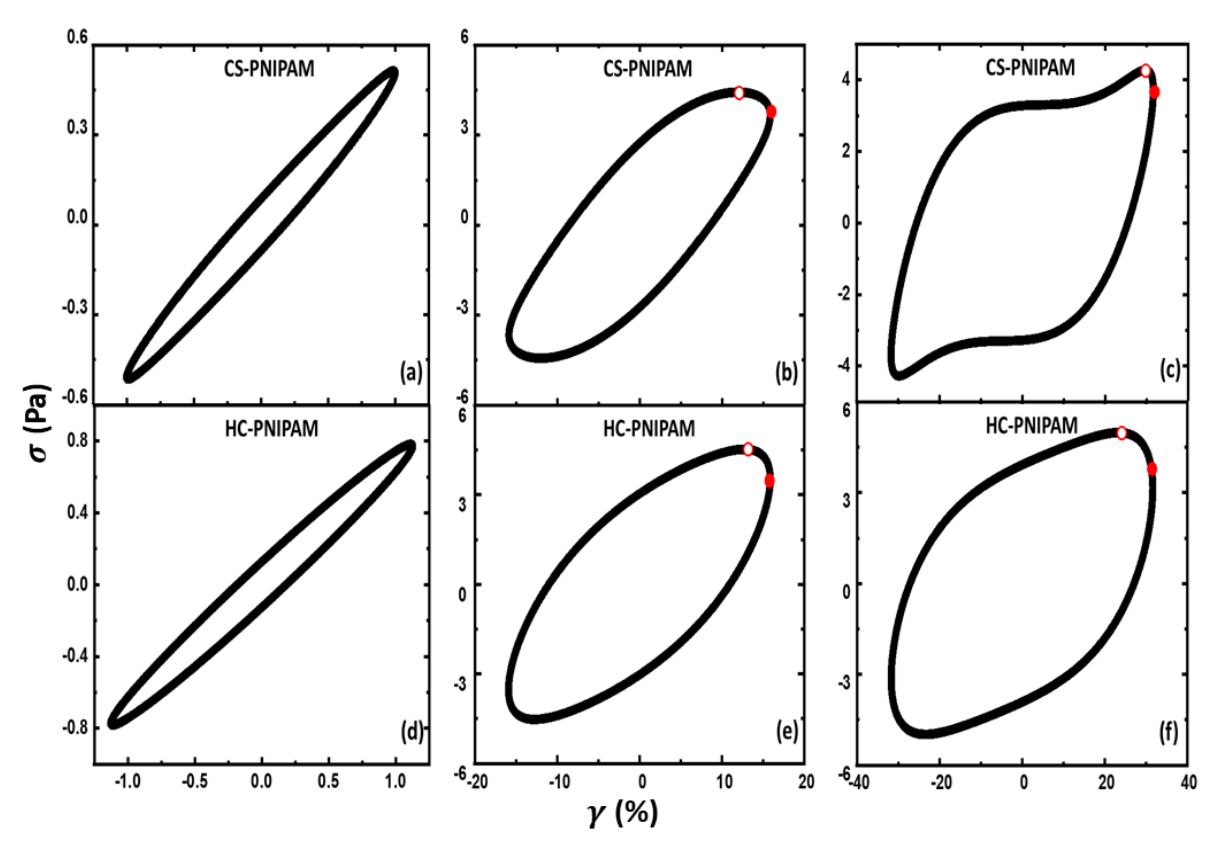


Fig. 3.7. LB curves for the CS-PNIPAM sample (a-c) with $\phi = 0.80$ and HC-PNIPAM sample (d-f) with $\phi = 0.89$. (a) and (d) are in the linear regime of the samples ($\gamma_0 < 5\%$) and (b), (c), (e) and (f) are in the non-linear regime of the samples ($\gamma_0 > 5\%$) with strain amplitude increasing from left to right. Open circle and closed circle represent static yield stress as the maximum stress overshoot, and the dynamic yield stress at the point of zero instantaneous shear rate respectively. Figures (a) to (f) correspond to $T = 20^{\circ}$ C.

response of the elastic LB curves by decomposing it into the sequence of physical processes such as elastic straining, yielding and flow behavior.

Yielding behavior of the dense microgel glass of CS-PNIPAM and HC-PNIPAM particles is shown in Fig. 3.3(a) and 3.3(b), respectively. Upon application of shear beyond a certain value of $\gamma_0 > 16\%$ the suspension yield via breaking of entanglement ($\gamma_0 \sim 20\%$) as well as breaking of cage ($\gamma_0 \sim 60\%$) (referred to as two-step yielding which is shown in Fig. 3.3(a)). Meanwhile, HC-PNIPAM shows yielding by single step which is attributed to the cage breaking at the yield point $\gamma_0 \sim 20\%$ (Fig. 3.3(b)). To gain further insight to the process of yielding, we determined the static yield stress (σ_{ys}) as the maximum stress overshoot, and the dynamic yield stress (σ_{yd}) at the point of zero instantaneous shear rate as defined by Rogers *et al.* [18] and applied by K. van der Vaart to soft and hard sphere suspensions [32]. Static yield stress, σ_{ys} (shown as closed circles in Fig. 3.8) and dynamic yield stress, σ_{yd} (shown as open circles in Fig. 3.8) obtained from LB curves for CS-PNIPAM and HC-PNIPAM dense microgel glasses are shown in Fig. 3.8(a) and (b) respectively. Notice from the insets shown in Fig. 3.8(a) & (b) that for small values of strain amplitude $\gamma_0 < 10\%$, the difference between the two yield stresses is too small, hence are expected to show overlap and also signifies no yielding of the microgel system.

Only for strain amplitudes beyond $\gamma_0 > 10\%$ the two stresses become different, indicating that yielding has occurred. These apparent yield stresses are generally associated with cage breaking and cage reformation [18]. Notice that a clear difference between σ_{ys} and σ_{yd} is observed for strains higher than $\gamma_0 > 50\%$ (see Fig. 3.8(a) for CS-PNIPAM glass and $\gamma_0 > 10\%$ for HC-PNIPAM glass indicating breaking and reformation of the nearest neighbor cage, in agreement with earlier reported work [32]. However, notice an important feature only in the case of CS-PNIPAM microgel glass that the difference between σ_{ys} and σ_{yd} do exist with some non-montonic variation for γ_0 values between 20% to 50%. This feature being present

in the case of CS-PNIPAM glass but not in HC-PNIPAM glass indicates that there exists a yielding mechanism before the usual yielding that occurs due to cage breaking and reformation. We attribute the yielding that is observed for γ_0 values between 20% to 50% in the case of CS-PNIPAM (Fig. 3.8(a)) in dense microgel glass to breaking and reformation of entanglements between dangling polymer chains that exists between near-neighbors of CS-PNIPAM microgel particles. Thus, dense suspensions of CS-PNIPAM microgel suspensions yield in two steps (*i.e.*, referred to as two-step yielding) one due to breaking and reformation of entanglements between dangling polymer chains and the second one is due to the cage breaking and reformation.

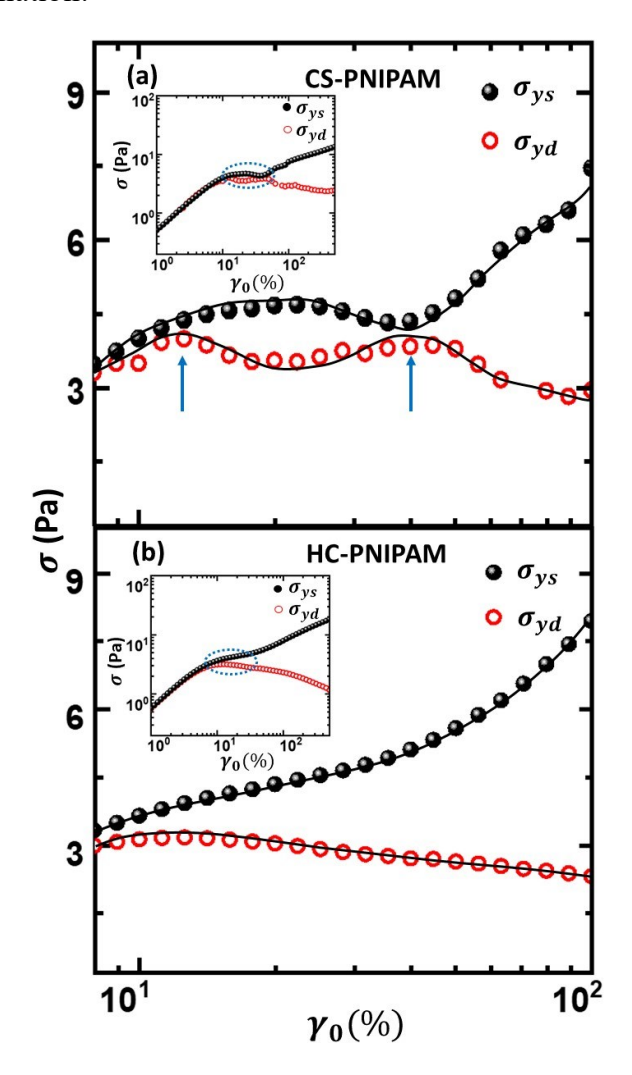


Fig. 3.8. Static yield stress at maximum elastic stress (closed circle) and dynamic yield stress at instantaneous zero shear rate (open circle) for (a) CS-PNIPAM and (b) HC-PNIPAM. Arrows represent the strain regime for CS-PNIPAM sample where gradual difference between static and dynamic yield stresses can be observed. Inset: static and dynamic yield stress determined in the entire deformation regime (a) for CS-PNIPAM and (b) for HC-PNIPAM. Dotted circles represent the region of interest where σ_{vs} and σ_{vd} becomes distinct and indicates yielding. The lines drawn are guide to the eye.

3.3.4. Energy of yielding and dissipation

Adopting the analysis of K. van der Vaart $et\,al.$ [32] and that reported earlier by Rogers $et\,al.$ [18], we calculated the dissipation energy, E_D from Eq. 3.2 and Eq. 3.3. This E_D is then compared with the dissipated energy reported by Donely $et\,al.$ [41] (see Fig. 3.9). It has been seen that dissipation energy graph takes the same form of that reported by K. van der Vaart $et\,al.$ [32]. Further, the energy dissipated during yielding, E_Y has been determined from the LAOS parameters using Eq. 3.3 and Eq. 3.4 for dense microgel glasses of CS-PNIPAM and HC-PNIPA M particles. In the case of CS-PNIPAM glass, it is expected that the entanglements between the microgel particles reflect in the yielding energy.

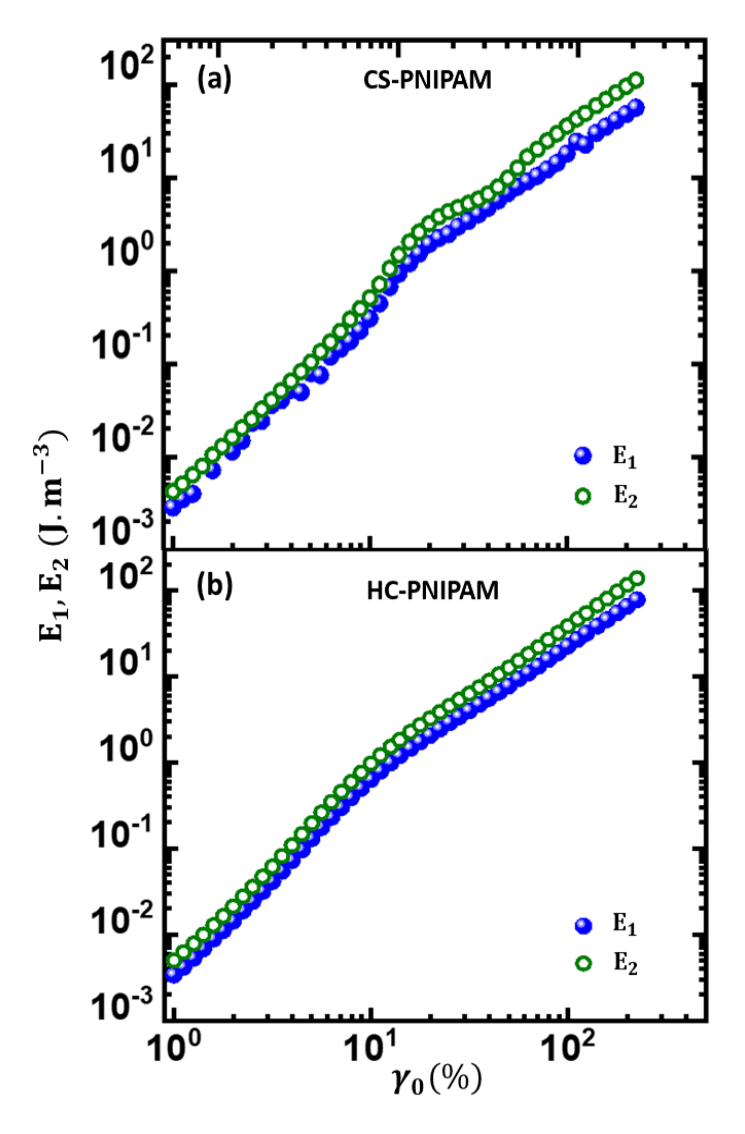


Fig. 3.9. Dissipated energy calculated (a) for CS-PNIPAM and (b) for HC-PNIPAM from the LB curve using the equations 3.2 and 3.3 (E_1) and dissipated energy calculated according to Donely *et al.* (2020) [41] (E_2) .

With an aim to compare the energy dissipated during yielding, E_Y has been plotted against the strain amplitude, γ_0 and is shown in Fig. 3.10. It is evident from Fig. 3.10 that CS-PNIPAM requires relatively higher energy for yielding as compared to microgel glass of HC-PNIPAM spheres. Arrows in Fig. 3.10 for CS-PNIPAM represent the peaks in the yielding energy, E_Y corresponding to two γ_0 values at which yielding occurs (Fig. 3.3(a)). Also notice from Fig. 3.10 that the height of first peak is higher than that of second peak. This implies that the energy utilized for breaking the entanglements (peak at $\gamma_0 \sim 20\%$) is relatively higher than the energy associated with cage breaking observed at $\gamma_0 \sim 60\%$.

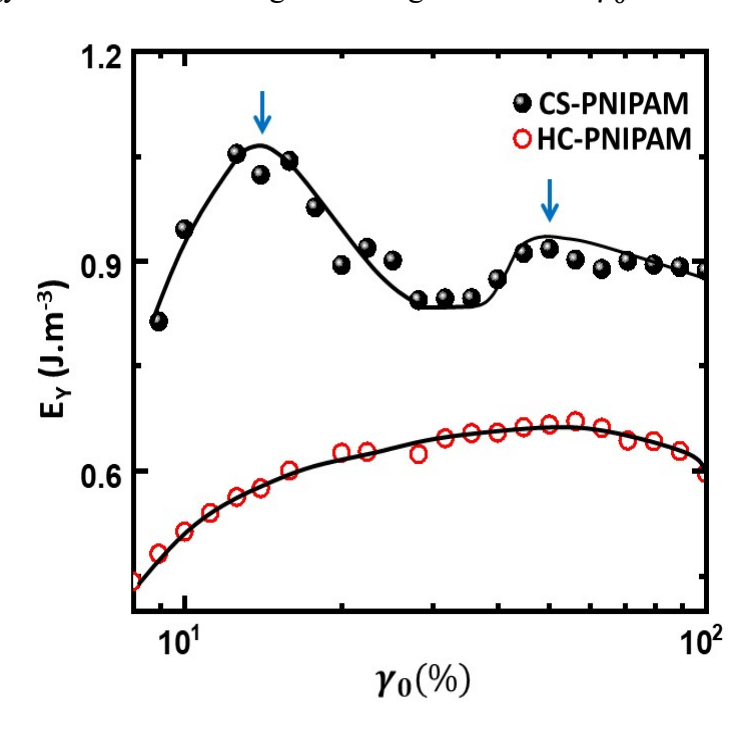


Fig. 3.10. Strain amplitude, γ_0 dependence of yielding energy, E_Y for CS-PNIPAM (closed circle) and HC-PNIPAM (open circle) at $T = 20^{0}$ C. Peaks in yielding energy (represented by arrows) of CS-PNIPAM are identified due to entanglement breaking and cage breaking. The lines drawn are guide to the eye.

3.4. Summary

We synthesized two types of PNIPAM microgel particles, one with a core-shell (CS) structure and the other with a homogeneous core (HC). By performing linear and non-linear rheological measurements as function of frequency and strain amplitude on the dense suspensions ($\phi > 0.64$) of both types of microgel particles, we showed at T = 20°C the dense

suspensions are in their glassy state which undergo melting in to a colloidal liquid state upon increasing the temperature beyond their glass transition temperature. Non-linear rheological measurements have shown that CS-PNIPAM glass exhibits two-step-yielding and HC-PNIPAM glass shows single step yielding. Observation of two-step yielding along with sub-diffusive behavior at small time scales in the glassy state of CS-PNIPAM particles and only single step yielding and absence of sub-diffusive behavior in the glassy state of HC-PNIPAM particles, provide unambiguous evidence for the existence of entanglements between dangling polymer chains in the shell of near neighbor CS-Particles under dense conditions. LAOS measurements on these dense microgel glasses also showed two-step yielding in the CS-PNIPAM sample and single step yielding in the HC-PNIPAM sample. Further the yielding energy estimated by analysing the LB curves recorded on CS-PNIPAM and HC-PNIPAM microgel glasses provided insight on the energy scales associated with breaking and reformation of entanglements that exist between dangling polymer chains and cage breaking and re-formation responsible for observed two-step yielding and usual single step yielding in the respective dense microgel glasses.

References

- 1. G. H. Fredrickson, Annu. Rev. Phys. Chem. **39**,149 (1988).
- 2. M. D. Ediger, C.A. Angell and S. R. Nagel, J. Phys. Chem. 100, 13200 (1996).
- 3. B.V.R. Tata, in Statistical physics of complex fluids, edt. S. Maruyama and M.Tokuyama,
 Tohoku University Press, Sendai, Japan
- 4. B. V. R. Tata, P. S. Mohanty, M. C. Valsakumar, Phys. Rev. Lett 88, 018302 (2001)
- 5. R.G. Larson, The structure and rheology of complex fluids. Oxford university press, New York (1999)
- 6. H. H. Winter, Macromolecules **46**, 2425 (2013)

- 7. T. G. Mason, D. A. Weitz, Phys. Rev. Lett **75**, 2770 (1995)
- 8. P. N. Pusey, W. Van Megen, Phys. Rev. Lett **59**, 2083 (1987)
- 9. W. Van Megen, P. N. Pusey, Phys. Rev. A 43, 5429 (1991)
- 10. W. Van Megen and S. M. Underwood, Phys. Rev. E 49, 4206 (1994).
- J. Mattsson, H. M. Wyss, A. Fernandez-Nieves, K. Miyazaki, Z. Hu, D. R. Reichman and D. A. Weitz, Nature 462, 83 (2009).
- 12. R. G. Joshi, B. V. R. Tata, and J. Brijitta, AIP Conf. Proc. 1349, 208 (2011)
- 13. C. Urban, P. Schurtenberger, J. Colloid Interface Sci. 207, 150 (1998)
- 14. R. G. Joshi, and B. V. R. Tata, J. Colloid Polym. Sci. 295, 1671 (2017)
- 15. V. Carrier, and G. Petekidis, J. Rheol **53**, 245 (2009)
- 16. K. K. Jathavedan, F. Kanheerampockil, S. Bhat, J. Appl. Polym. Sci 137, 48625 (2020)
- 17. M. J. Bergman, N. Gnan, M. Obiols-Rabasa, J.M. Meijer, L. Rovigatti, E. Zaccarelli, P. Schurtenberger, Nat. Commun. 9, 5039 (2018).
- 18. S. A. Rogers, B. M. Erwin, D. Vlassopoulos, M. Cloitre, J. Rheol **55**, 435 (2011)
- 19. R. H. Pelton, and P. Chibante, J. Colloids and surfaces 20, 247 (1986)
- 20. D. Karthickeyan, R. G. Joshi, and B. V. R. Tata, J. Chem. Phys **146**, 224503 (2017)
- 21. P. N. Pusey, and W. Van Megen, Physica A: Statistical Mechanics and its Applications 157, 705 (1989)
- 22. H. Furukawa, and S. Hirotsu, J. Phys. Soc. Jpn 71, 2873 (2002)
- 23. P. N. Segre, and P. N. Pusey, Phys. Rev. Lett 77, 771 (1996)
- 24. K. Miyazaki, H. M. Wyss, D. A. Weitz, and D. R. Reichman, Europhys. Lett 75, 915 (2006)
- 25. P. Sollich, F. Lequeux, P. Hébraud, M. E. Cates (1997), Phys. Rev. Lett **78**, 2020 (1997)
- 26. K. N. Pham, G. Petekidis, D. Vlassopoulos, S. U. Egelhaaf, P. N. Pusey, and W. C. K. Poon, Europhys. Lett **75**, 624 (2006)
- 27. R. H. Ewoldt, A. E. Hosoi, G. H. McKinley, J. Rheol 52, 1427 (2008)

- 28. S. Tariq, A. J. Giacomin, and S. Gunasekaran, J. Biorheology, 35, 171 (1998)
- 29. P. R. de Souza Mendes, R. L. Thompson, A. A. Alicke, and R. T. Leite, J. Rheol 58, 537 (2014)
- 30. M. Wilhelm, Macromol. Mater. Eng 287, 83 (2002)
- 31. M. Wilhelm, D. Maring, H. W. Spiess, Rheol. Acta 37, 399 (1998)
- 32. K. van der Vaart, Y. Rahmani, R. Zargar, Z. Hu, D. Bonn, and P. Schall, J. Rheol 57, 1195 (2013)
- 33. J. Mattsson, H. M. Wyss, A. Fernandez-Nieves, K. Miyazaki, Z. Hu, D. R. Reichman, and D. A. Weitz, Nature **462**, 83 (2009)
- 34. W. Van Megen, and S. M. Underwood, Phys. Rev. E 49, 4206 (1994)
- 35. A. Shukla, S. Arnipally, M. Dagaonkar, and Y. M. Joshi, Rheol. Acta 54, 353 (2015)
- 36. G. Petekidis, D. Vlassopoulos, and P. N. Pusey, Faraday discussions 123,287 (2003)
- 37. K. N. Pham, G. Petekidis, D. Vlassopoulos, S. U. Egelhaaf, W. C. K. Poon, and P. N. Pusey, J. Rheol 52, 649 (2008)
- 38. M. J. Bergman, N. Gnan, M. Obiols-Rabasa, J. M. Meijer, L. Rovigatti, E. Zaccarelli, P. Schurtenberger, Nature communications 9, 1 (2018)
- 39. B. R. Saunders, Langmuir 20, 3925 (2004)
- 40. M. H. Kwok, Z. Li, and T. Ngai, Langmuir 29, 9581 (2013)
- 41. G. J. Donley, P. K. Singh, A. Shetty, S. A. Rogers, PNAS 117, 21945 (2020)

SHEAR-INDUCED FLOW BEHAVIOR OF LYOTROPIC CHROMONIC LIQUID CRYSTALS

This chapter describes the shear-induced flow and dynamics of the nematic phase of Sunset Yellow lyotropic chromonic liquid crystal. The flow curves (stress (σ)-strain rate ($\dot{\gamma}$) curves) has been determined at different temperatures, exhibit unusual near plateau regime at intermediate shear rates. The dynamic stress fluctuations in the near-plateau regime are studied, and further, the non-monotonic flow curves and the stress dynamics are corroborated using in-situ rheo-microscopy.

4.1 Introduction

hear induced flow behavior of soft-matter systems driven out of equilibrium by external shear is a fascinating domain of rheology. The soft matter systems of worm-like micells have been extensively investigated over the past few decades to understand their shear induced responses. It has been reported that micellar systems under external shear show various responses such as structural changes [1], phase transitions [2], rheochaos [3,4], birefringence [2], stress dynamics [3,4], etc. In which the stress dynamics constitute the primary feature shown by worm-like micellar solutions under shear. The stress dynamics in worm-like micellar solutions are deeply studied by Ganaphy *et al.* [3] and Sood *et al.* [4]. These authors report that the instability due to flow-concentration coupling in the shear flow for a particular range of shear rates is responsible for the observed stress dynamics [3,4].

Although shear-induced microstructures and flow dynamics of micellar systems have been well-studied, they were relatively underexplored in the case of liquid crystal systems. Very recently, Praveen Kumar *et al.* has reported shear induced flow and dynamics in thermotropic LC [5]. The authors reported non-monotonic flow behavior with three dynamic stress regimes (a non-Newtonian flow regime at low shear rate, a near plateau regime at intermediate shear rate and a Newtonian regime at high shear rate) in certain temperature and shear-rate range. The near plateau and stress oscillations observed in the intermediate shear rate regime resembles with that reported in worm-like micells. However, no visual evidence was provided in confirming the observations.

Unlike thermotropic LCs, lyotropic LCs were poorly investigated for their rheological responses. Very recently, Baza *et al.* have studied the rheological properties of disodium cromoglycate (DSCG) chromonic liquid crystal in detail [6]. Using polarizing optical microscope and wide-angle X-ray scattering techniques they correlated the director orientation and shear-induced microstructure. The study provided insightful information on the director dynamics such as the formation of logrolling state in region I ($\dot{\gamma} < 1 \ s^{-1}$), occurrence of singular disclination loops in region II ($1 \ s^{-1} < \dot{\gamma} < 10 \ s^{-1}$) and evolution of periodic stripe-like textures in region III ($1 \ s^{-1} < 1 \ s^{-1}$). Although several experiments on SSY and salt added systems have been reported [7-13] the microstructures, director dynamics and correlations to the flow properties of pristine SSY are unknown. With this motivation, we have chosen SSY to study rheological properties.

In this work, we systematically investigate the rheological properties of the nematic phase of SSY liquid crystal, focusing mainly on the shear-induced microstructures and dynamics. We obtain three distinct flow regimes R1, R2 and R3 at different shear rates. It exhibits Newtonian flow behavior at low and high shear rates (R1, R3). In the intermediate

shear rate (R2) it shows a non-Newtonian response with temporal stress fluctuations under steady shear.

4.2 Experimental Details

SSY purchased from Sigma Aldrich was purified using a precipitation method [14, 15]. The chemical structure of the compound in the azo as well as in the hydrazone form is shown in Fig. 1.11 (see chapter 1, section 1.2.2). The liquid crystalline state was obtained by dissolving the requisite amount of SSY in a known amount of Milli-Q water (resistivity greater than 18M Ω .cm). The sample container was immediately sealed and sonicated until the solution appeared homogeneous. All the measurements performed in this study have been carried out on 32 wt% aqueous solution of SSY which exhibits the nematic phase at room temperature [12]. A schematic arrangement of the disc-shaped molecules in the nematic phase is shown in Fig. 1 (c). The texture of the sample was observed using a polarizing optical microscope (Olympus BX51) at room temperature (T=24 0 C). For this purpose, the sample cells were prepared by sandwiching a drop of SSY liquid crystal between two glass slides (1 mm thickness) separated by 5 μ m spacers. The edges of the cell were sealed using epoxy glue to prevent evaporation of water. A typical texture of the nematic phase is shown in Fig. 1.12(b) (see chapter 1, section 1.2.2)

A strain-controlled rheometer (MCR 501, Anton Paar) equipped with a rheo-microscope (RM) module was used to simultaneously perform rheological measurements and for *in-situ* imaging of the sample (Fig. 4.1). The RM module consists of a monochrome CCD camera (model: Lumenera), a microscope tube with a polarizer, an analyzer and a long working distance objective (NA = 0.4, 20X, Nikon). Two parallel glass plates of thickness 6 mm and diameter 43 mm separated by a gap of 0.075 mm were used for the flow curve measurements and rheo-microscopy. Each measurement took about 30 minutes to complete. A visible light

source (Edmund MI-150) was used to illuminate the sample through the microscope objective from the bottom. An analyzer oriented at 90° with respect to the polarizer axis was kept in the microscope tube and the images were captured by the CCD camera in the reflection mode. The sample temperature was controlled by a Peltier-based temperature controller. The uniformity of the sample temperature was maintained by covering the measuring system with a thermally insulated hood. A fresh sample was mounted in each experiment to eliminate the sample history effect. A thin layer of silicone oil (viscosity ≈ 99 mPa s) was applied around the exposed area of the sample to prevent evaporation of water and maintain concentration during the measurements. All the measurements were performed within 30 minutes of sample preparation to minimise any concentration change.

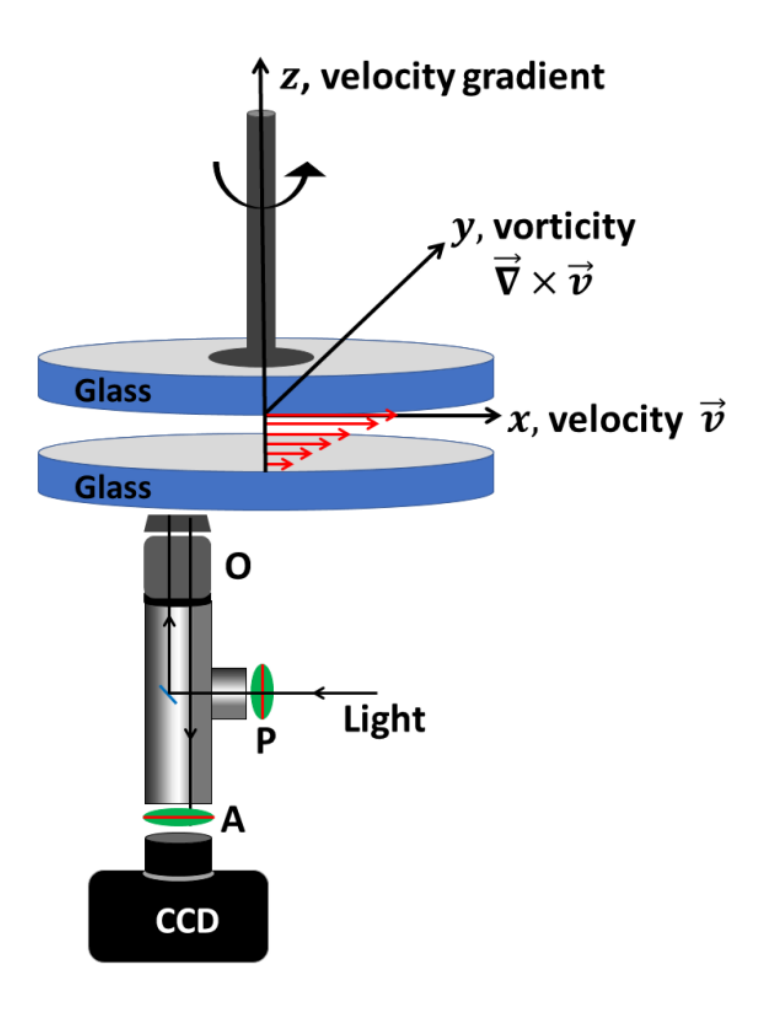


Fig. 4.1. Experimental setup for performing *in-situ* rheo-microscopy. Letters O, P and A indicate microscope objective, polarizer and analyzer, respectively. The microscope module is mounted on a xy stage (not shown).

4.3 Results and Discussions

4.3.1 Flow curves

Figure 4.2(a) shows the flow curves obtained in the nematic phase at various temperatures (21° C to 35° C). Initially, stress σ increases with the shear rate $\dot{\gamma}$. Above a critical shear rate $\dot{\gamma}_{cl}$, σ saturates as reported in nematic twistbend (N_{TB}) liquid crystal [5], in surfactant solutions of cetylpyridinium chloride-sodiumsalicylate (CPyCl-NaSal) [16-19] and in concentrated cetyl trimethylammonium tosylate (CTAT) solutions [20]. Above an upper shear rate $\dot{\gamma}_{cu}$ the stress abruptly jumps to a higher value and further increases with increasing shear rate. Thus, the flow curves clearly exhibit three regimes which are marked as R1 ($\dot{\gamma} < \dot{\gamma}_{cl}$), R2 ($\dot{\gamma}_{cl} < \dot{\gamma} < \dot{\gamma}_{cu}$) and R3 ($\dot{\gamma} < \dot{\gamma}_{cu}$).

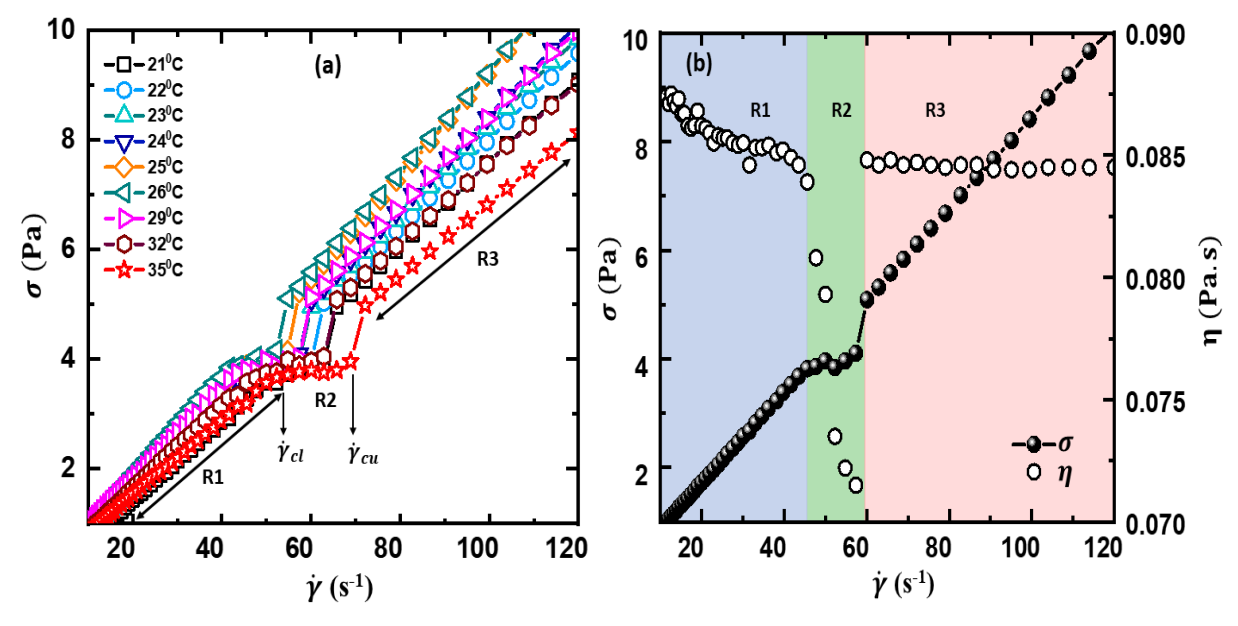


Fig. 4.2(a). Flow curves (σ versus $\dot{\gamma}$) at different temperatures in the nematic phase of SSY LC (32 wt%). Different regimes are labelled as R1, R2 and R3 which are separated by the lower and upper critical shear rates ($\dot{\gamma}_{cl}$ and $\dot{\gamma}_{cu}$), respectively. (b) Shear-rate dependence of shear stress σ and shear viscosity η of the sample at $T=24^{\circ}$ C.

Figure 4.2(b) shows a representative variation of shear stress and corresponding shear viscosity (η) measured at room temperature ($T=24^{\circ}$ C). The viscosities are almost equal in regimes R1 and R3 whereas, it drops down abruptly in regime R2. Figure 4.3 shows the variation of critical shear rates ($\dot{\gamma}_{cl}$ and $\dot{\gamma}_{cu}$) with temperature. It shows a non-monotonic

behavior with temperature. The regime R2 emerges within a narrow range of shear rate ($\Delta \dot{\gamma} = \dot{\gamma}_{cu} - \dot{\gamma}_{cl} \approx 15 \ s^{-1}$).

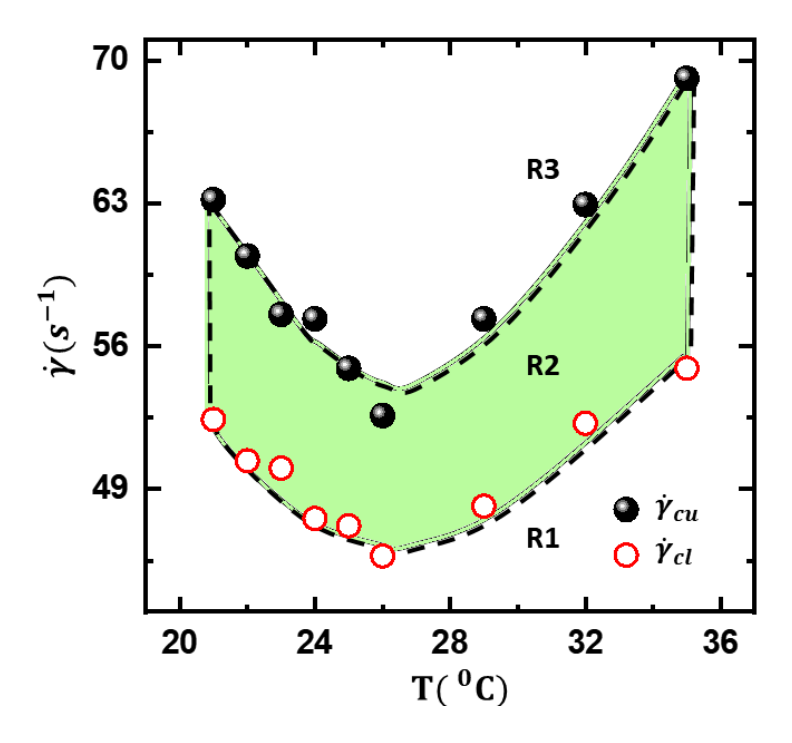


Fig. 4.3. Temperature dependence of $\dot{\gamma}_{cl}$ (open circles) and $\dot{\gamma}_{cu}$ (closed circles).

We fit shear rate-dependent stress $\sigma(\dot{\gamma})$ with appropriate relations. In regime R1, $\sigma = K_1 \dot{\gamma}$ (Fig. 4.4(a)), hence the flow is Newtonian. Here the proportionality constant $K_1 = \sigma_{eff}$ (effective viscosity). Similarly in regime R3, $\sigma = K_3 \dot{\gamma}$, suggesting the flow is Newtonian with K_3 being the effective viscosity (Fig. 4.4(b)). In regime R2, σ is fitted to a power-law: $\sigma \sim \dot{\gamma}^{\beta}$ with the exponent $\beta \approx 0.36$ -0.54 (± 0.06) (Fig. 4.5). Qualitatively similar stress plateau was reported in micellar aqueous solutions of surfactant cetyltrimethylammonium tosylate (CTAT) as a function of salt concentration [21]. Such stress plateaus indicate coexisting bands of differing viscosities due to the coupling of flow and concentration, where the shear flow causes the inhomogeneous spatial distribution of the components (concentration gradient) in the micellar systems [4,16-18,21-27]. In worm-like micellar systems very near the nematic to

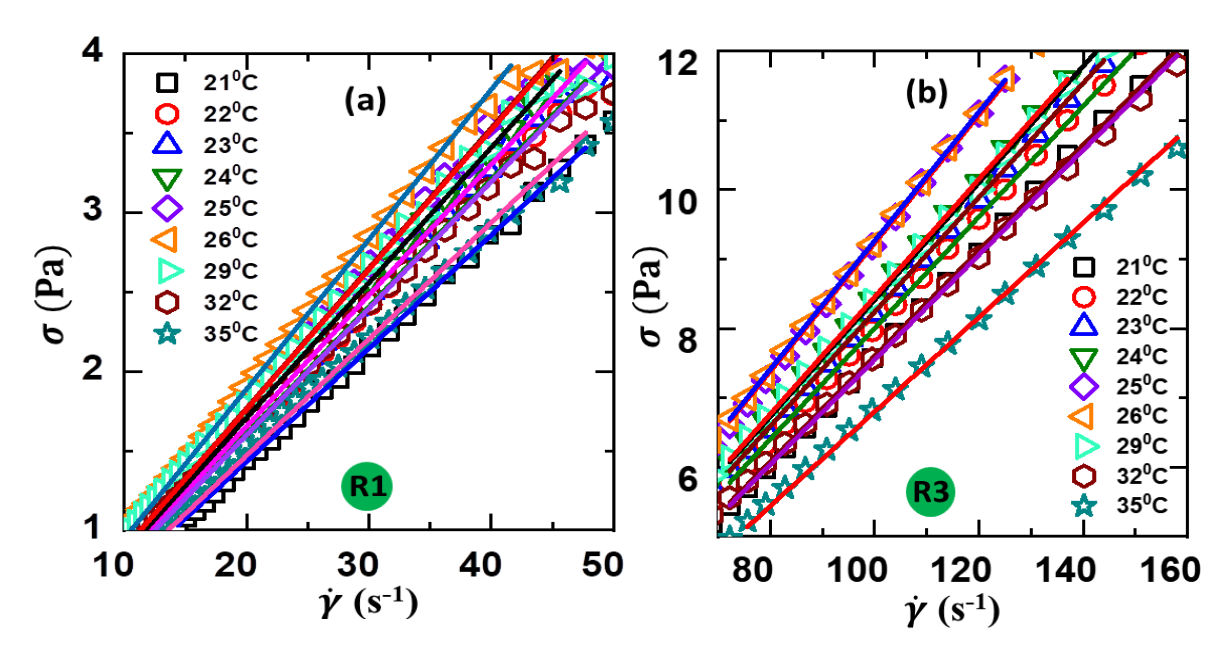


Fig. 4.4. Linear fit to (a) regime R1 and (b) regime R3 with $\sigma = K_i \dot{\gamma}$, where K_i is constant and i = 1, 3.

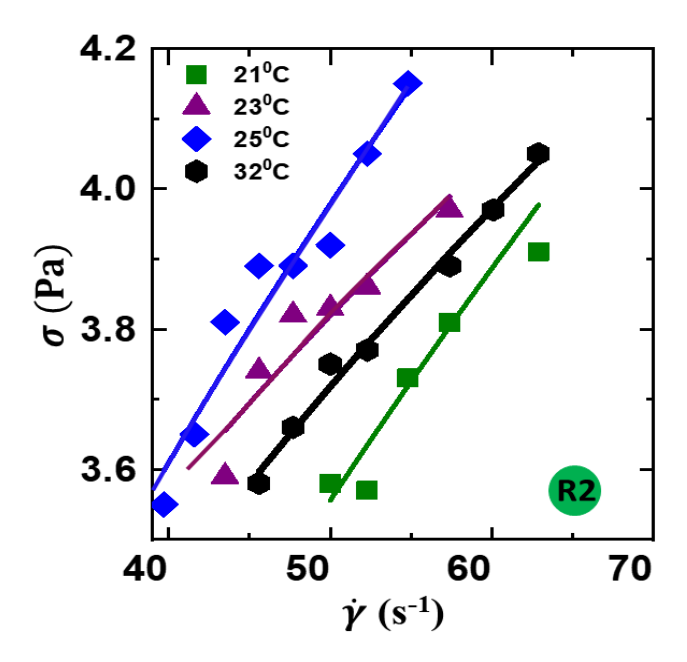


Fig. 4. 5. Regime R2 is fitted to $\sigma \sim \dot{\gamma}^{\beta}$ with $\beta \approx 0.36$ - 0.54. Solid lines are the best fits.

isotropic phase transition, a similar stress plateau was reported. It occurred due to the separation of low (isotropic) and high viscous (nematic) regions, forming shear bands [16,17]. We work far below the nematic to isotropic transition temperature hence shear banding effects can be ruled out. We conjecture that the shear-induced mechanical instability is responsible for the observed plateau regime (see later).

4.3.2 Rheo-microscopy: Defect structure

We performed *in-situ* rheo-microscopy experiments to understand the origin of different flow regimes. In this setup, the sample was observed under crossed polarizer and analyzer system with the polarizer axis being perpendicular to the flow direction as shown in Fig. 4.1. We sheared the sample before any measurement to avoid loading history. Figure 4.6 shows representative rheo-microscopy images obtained at room temperature ($T = 24^{\circ}$ C). In the low shear rate regime R1 the sample shows a polydomain texture with a few randomly oriented disclination defect lines (Fig. 4.6(a)). This suggests that the director is predominantly orientated along the vorticity direction similar to what was reported in DSCG chromonic LC [6]. In the medium shear rate regime R2 (near-plateau) the texture is highly distorted and the number density of the disclination defects is increased and they are oriented nearly parallel to the flow direction (Fig. 4.6(b)). It is also noted that the brightness of the texture in regime R2 decreases considerably compared to that of regime R1. This is perhaps due to the effect of highly distorted director (see later) and enhanced defect density in the sample. No defects are seen in regime R3 (Fig. 4.6(c)) and the texture is rather uniform and brighter than that in R1 and R2. This indicates that the director is uniform throughout the sample due to the high shear rate and also tilted with respect to the axis of the polarizer or analyzer. In the case of DSCG, the sample in a thinner shear cell ($\sim 10 \, \mu \text{m}$) in regime III exhibited stripe texture in which on average the director was parallel to the flow direction, with left and right tilts to the vorticity direction [6]. Apart from this, high shear rate can also influence the scalar order parameter by dissociating into smaller or associating into longer columnar units as the aggregation forces in LCLCs are relatively weak.

The flow properties of SSY may be compared with that of DSCG chromonic liquid crystal. The shear rate-dependent viscosity of DSCG chromonic nematic liquid crystal with 14 wt% dispersion in water has been measured by Baza *et al.* [6]. They have segmented the

entire flow curve ($\dot{\gamma}=0.1$ to $1000~s^{-1}$) into three regimes I, II and III, depending on the slope of the viscosity vs shear-rate curve. It shows shear-thinning behavior with two shear-thinning regimes (I: $\dot{\gamma} < 1~s^{-1}$ and III: $\dot{\gamma} > 10~s^{-1}$) separated by a pseudo-Newtonian regime (II: $1~s^{-1} < \dot{\gamma} < 10~s^{-1}$). The viscosity of the sample (entire flow curve) decreases from 0.13 to 0.04 Pa s with increasing shear rate. In our experiment, we mostly work in the shear rate range from $10~s^{-1}$ to $120~s^{-1}$. In contrast to DSCG, SSY chromonic system shows two Newtonian flow regimes separated by a non-Newtonian flow regime. For example, at room temperature two Newtonian regimes R1 ($\dot{\gamma} < 45~s^{-1}$) and R3 ($\dot{\gamma} > 60~s^{-1}$) are separated by a narrow non-Newtonian regime R2 ($45~s^{-1} < \dot{\gamma} < 60~s^{-1}$) (see Fig. 4.2(b)). The viscosity in R2 goes down to about 0.07 Pa s. In DSCG system, regime I shows a log-roll type director structure, regime III shows a stripe pattern parallel to the flow direction and regime II is dominated by defects. The overall director structure and defects in regimes I and II appear to be very similar in both liquid crystals. However, regime III appears to be more uniform in SSY and the stripe patterns reported in the case of DSCG could not be observed perhaps due to the higher shear rates in our experiments.

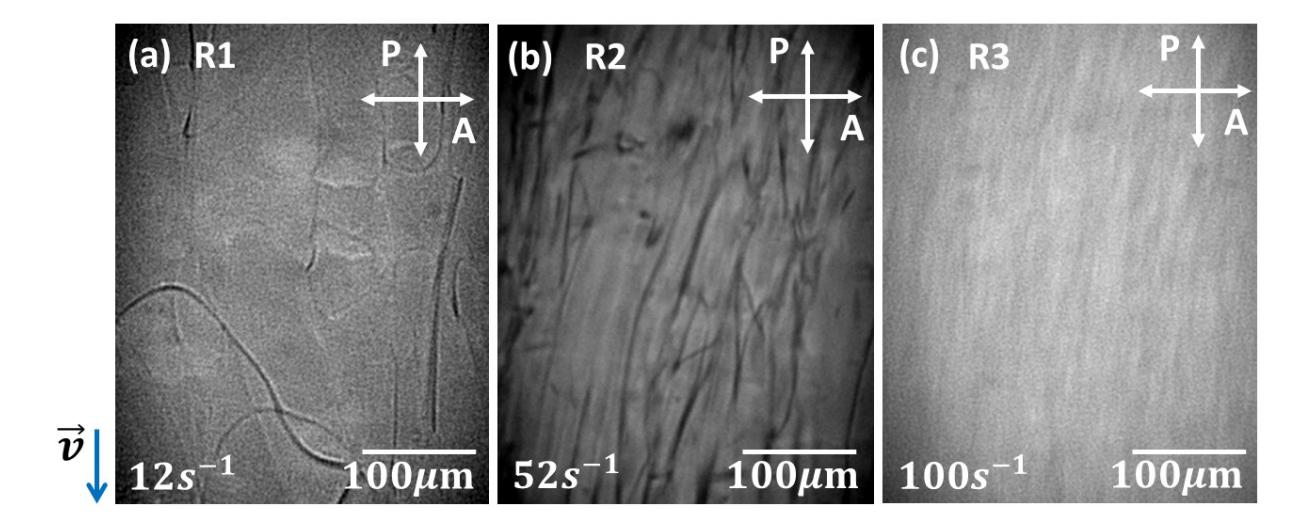


Fig. 4.6. Representative rheo-microscopy images from three regimes R1, R2 and R3 at different shear rates at room temperature ($T = 24^{\circ}$ C). The shear rate value on each image is marked on the top. The flow direction is shown with a blue arrow at the left corner.

4.3.3 Stress oscillations

The stress plateau is often considered a signature of shear-banded inhomogeneous stationary flows resulting in mechanical instability [25] and stress oscillations [3-5,21,22]. To see the response in our system we measured time-dependent stress at a fixed shear rate. A cone-plate measuring system of diameter 50 mm is employed to keep the shear rate uniform throughout the sample. Figure 4.7 shows that the flow curve is similar to that of the parallel-plate system (see data for $T=24^{\circ}$ C in Fig. 4.2(b)) except that the critical shear rates, $\dot{\gamma}_{cl}$ and $\dot{\gamma}_{cu}$ in cone-plate (26 s^{-1} and 38 s^{-1}) are smaller than the values measured in the parallel plate system (46 s^{-1} and 60 s^{-1}). It may be noted that the effective viscosity ($\sigma/\dot{\gamma}$, see regime R3 in Fig. 4.7) at room temperature, measured using the plate-cone is 0.06 Pa s, which is somewhat lower than that measured using the parallel-plate (0.085 Pa s) system (see Fig. 4.2(b). This difference arises due to the non-uniform shear rate in parallel-plate measuring system.

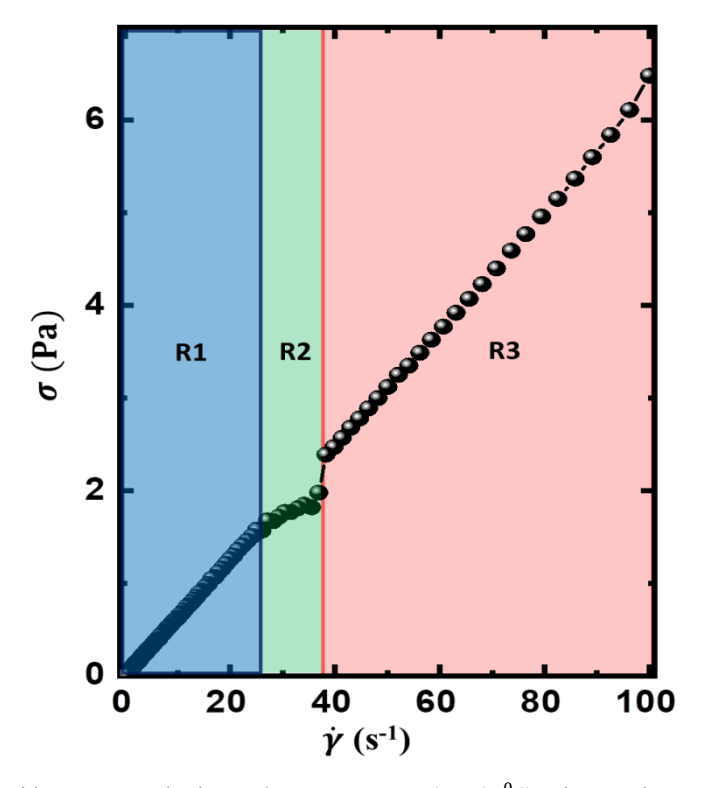


Fig. 4.7. Variation of σ with $\dot{\gamma}$ measured using a plate-cone system ($T = 24^{\circ}$ C). Three regimes are shaded with different colours.

Figure 4.8(a) shows the time-dependent stress at room temperature ($T = 24^{\circ}$ C) at three different shear rates, $\dot{\gamma} = 5$, 33 and $100 \, s^{-1}$ in regimes R1, R2 and R3, respectively. The stress response in regime R1 and R3 is observed to be independent of time whereas in regime R2 the stress exhibits temporal fluctuations. Figure 4.8(b) shows the corresponding Fourier power spectrum. It shows a periodic signal with fundamental mode (ω) and its higher harmonics. The value of the fundamental linear frequency of the power spectrum $f = 0.044 \, s^{-1}$ corresponding to $\omega = 2\pi f = 0.28 \, \text{rad/s}$ (Fig. 4.8(b)). The angular frequency of rotation of the plate and the corresponding shear rate is related to the cone angle (φ) and can be expressed

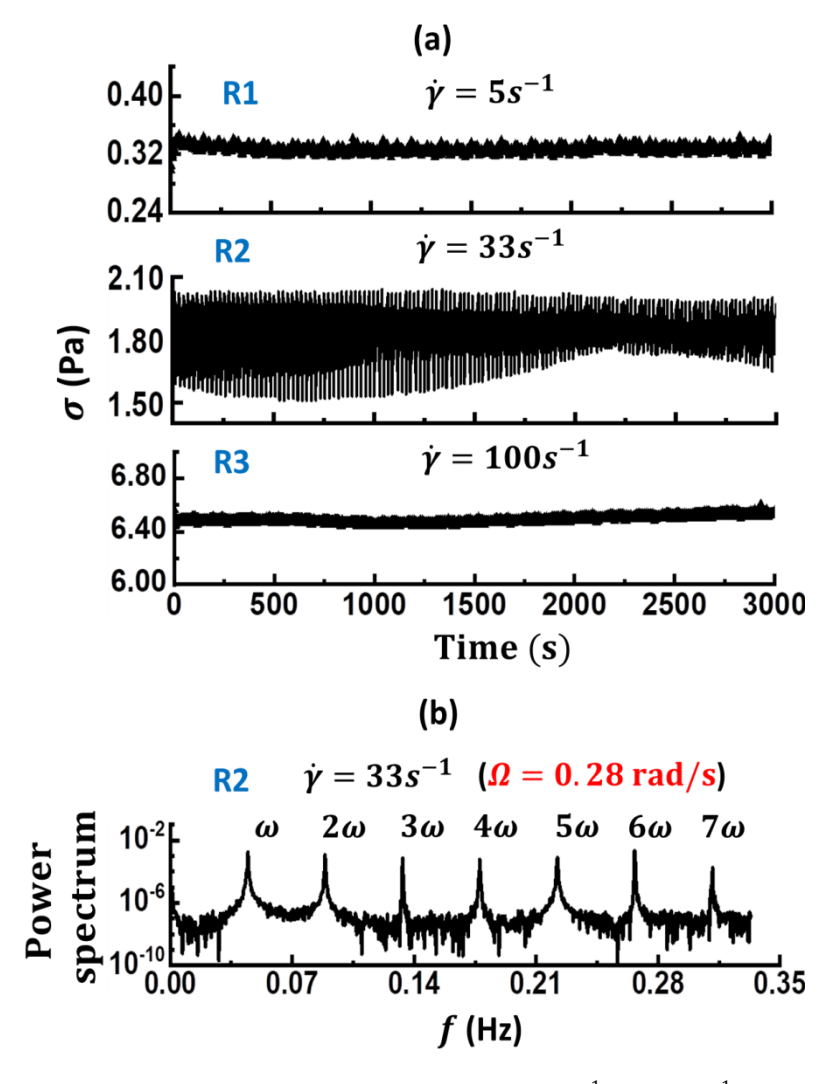


Fig. 4.8.(a) Time dependent stress for the selected shear rates $\dot{\gamma}=5~s^{-1}$ (R1), 33 s^{-1} (R2) and 100 s^{-1} (R3). (b) Fourier power spectrum corresponds to the stress fluctuations at $\dot{\gamma}=33~s^{-1}$ in regime R2. Fundamental frequency $\omega=2\pi f=0.28~{\rm rad/s}$ and a few harmonics are labelled. The angular frequency corresponding to the shear rate $\dot{\gamma}=33~s^{-1}$ is $\Omega=\dot{\gamma}\tan(\phi)=0.28~{\rm rad/s}$.

as $\Omega = \dot{\gamma} \tan(\varphi)$. In our setup $\varphi = 0.5^0$ hence $\Omega = 0.28$ rad/s and $\omega = \Omega$. It clearly shows that the periodic stress fluctuations are driven by the rotational shear force. Similar periodic stress oscillations including aperiodic and chaotic oscillations (rheo-chaos) were reported in worm-like micellar systems [21] and in thermotropic twist-bend nematic liquid crystals [5].

4.4 Summary

We explored the rheological properties of Sunset Yellow lyotropic chromonic nematic liquid crystal in the shear rate-range of 10 - 100 s^{-1} . At a fixed temperature the flow curves show three regimes; a near-plateau regime is surrounded by two Newtonian regimes. The transition from the first Newtonian regime (low shear rate-range) to the near-plateau regime is continuous whereas the transition is discontinuous from the near-plateau to the second Newtonian regime (high shear rate-range). In the first Newtonian regime the director is orientated along the vorticity direction and in the second Newtonian regime the director is predominantly aligned along the flow direction and in the plateau regime, it is highly distorted with plenty of disclination defects. The results suggest that SSY is a tumbling nematic. The driving shear force in the plateau regime gives rise to periodic stress oscillations similar to that was observed in the worm-like micellar system and recently in twist-bend nematic liquid crystals. In the case of the twist-bend nematic LCs, the stress oscillations were theoretically explained to originate from the change of the pseudolayer orientation with respect to the shear direction [28]. For the micellar systems, it occurs due to the flow-concentration and floworder (orientational) coupling that leads to the dynamic instability of shear bands [29]. Considering the similarities between micellar systems and studied chromonic systems (both are lyotropic nematics), we conjecture that the flow-order coupling effects are responsible for the mechanical instability and the resulting stress dynamics in the near plateau regime. We believe that theoretical modelling of the non-monotonic flow behaviour in lyotropic

chromonic liquid crystals is expected to provide deep understanding of the observations reported in this chapter.

References

- 1. W. Richtering, Current opinion in colloid & interface science, 6, 446 (2001).
- 2. H. Hoffmann, S. Hofmann, A. Rauscher, and J. Kalus, Progr Colloid Polym Sci. 84, 24
- 3. R. Ganapathy and A. K. Sood, Phys. Rev. Lett. 96, 108301(2006).
- 4. A. K. Sood and R. Ganapathy, Pramana, 67, 33 (2006).
- 5. M. P. Kumar, J. Karcz, P. Kula and S. Dhara, Phys. Rev. Materials., 5, 115605 (2021).
- 6. H. Baza, T. Turiv, B. X. Li, R. Li, B. M. Yavitt, M. Fukuto and O. D. Lavrentovich, Soft Matter, 16, 8565 (2020).
- 7. J. Lydon, Liquid Crystals, **38**, 1663 (2011).
- 8. M. P. Renshaw and I. J. Day, J. Phys. Chem. B, 114, 10032 (2010).
- 9. P. J. Collings, J. N. Goldstein, E. J. Hamilton, B. R. Mercado, K. J. Nieser, K. M. H. Regan, Liquid Crystals Reviews, 3, 1 (2015).
- V. R. Horowitz, L. A. Janowitz, A. L. Modic, P. A. Heiney and P. J. Collings, Phys. Rev. E, 72, 041710 (2005).
- 11. F. Chami and M. R. Wilson, J. AM. CHEM. SOC. 132, 7794 (2010).
- 12. A. Yamaguchi, Self-assembly of lyotropic chromonic liquid crystal mixtures, Condensed Matter Physics Commons. (2015).
- 13. S. K. Prasad, G. G. Nair, G. Hegde and V. Jayalakshmi, J. Phys. Chem B, 111, 9741 (2007).
- H. S. Park, S. W. Kang, L. Tortora, Y. Nastishin, D. Finotello, S. Kumar and O. D. Lavrentovich, J. Phys. Chem. B, 112, 16307 (2008).
- D. J. Edwards, J. W. Jones, O. Lozman, A. P. Ormerod, M. Sintyureva and G. J. T. Tiddy,
 J. Phys. Chem. B, 112, 14628 (2008).

- 16. J. F. Berret, D. C. Roux and G. Porte, J. Phys. II France, 4, 1261 (1994).
- 17. J. F. Berret, Langmuir, 13, 2227 (1997).
- 18. G. Porte, J. F. Berret and J. L. Harden, J. Phys. II France, 7, 459 (1997).
- 19. C. Grand, J. Arrault, M. E. Cates, J. Phys. II France, 7, 1071 (1997).
- 20. J. F. A. Soltero, F. Bautista, J. E. Puig and O. Manero, Langmuir, 15, 1604 (1999).
- 21. R. Bandyopadhyay, G. Basappa and A. K. Sood, Phys. Rev. Lett., 84, 2022 (2000).
- 22. R. Ganapathy and A. K. Sood, Langmuir, 22, 11016 (2006).
- 23. O. Diat, D. Roux and F. Nallet, J. Phys. II France, 3, 1427 (1993).
- 24. D. Roux, F. Nallet and O. Diat, Europhys. Lett., 24, 53 (1993).
- 25. P. Panizza, P. Archambault, D. Roux, J. Phys. II France, 5, 303 (1995).
- 26. S. M. Fielding and P. D. Olmsted, Eur. Phys. J. E, 11, 65 (2003).
- 27. S. M. Fielding and P. D. Olmsted, Phys. Rev.Lett., 92, 084502 (2004).
- 28. E. I. Kats, JETP Lett., 116, 254 (2022).
- 29. B. Chakrabarti, M. Das, C. Dasgupta, S. Ramaswamy, and A. K. Sood, Phys. Rev. Lett. 92, 055501 (2004).

SUMMARY AND FUTURE WORK

This chapter provides summary and conclusions of the investigations made towards the thesis using isotropic dense suspension of PNIPAM microgel particles and anisotropic lyotropic chromonic liquid crystal systems of SSY. The experimental techniques employed in these investigations include dynamic light scattering techniques, 3D dynamic light scattering techniques, UV-Visible spectroscopy, rheology and rheo-microscopy.

5.1 Summary and conclusions

t the initial part of the chapter 1, a concise overview of the literature pertaining to colloids, stimuli-responsive microgels, structure and dynamics of PNIPAM microgel particles, a short comparison on the yielding behavior of dense suspension of PNIPAM microgels with respect to the hard sphere and attractive glass is presented. In the dense glassy phase, the dangling polymer chains on the surface of PNIPAM microgel particles are expected to influence the dynamics and yielding behavior. Previous reports of two step yielding in PNIPAM suspension, that was attributed to the dangling polymer chains. However, we have given unambiguous evidence that dangling polymer chains are responsible for two-step yielding in repulsive PNIPAM suspensions.

The later part of the chapter 1 provide a brief introduction to liquid crystals, lyotropic chromonic liquid crystals and previous studies on the liquid crystal mesophases of aqueous solutions of sunset yellow chromonics. Unlike colloidal suspensions, lyotropic chromonic liquid crystals are known to be anisotropic. Shear response of thermotropic liquid crystals and

surfactant based worm-like micellar suspensions are well studied, however, chromonic LCs are not much tested to their shear response. This thesis presents detailed investigations on the shear induced flow and dynamics of SSY chromonic LC.

Towards the studies on the stimuli-responsive microgels, monodisperse PNIPAM microgel particles with two different morphologies *viz.*, i) homogeneous core, ii) core-shell, have been synthesized using free radical precipitation polymerization. The synthesis and purification procedure is described in chapter 2. These PNIPAM microgel particles were tested for their temperature response by measuring the hydrodynamic diameter as a function of temperature. The preparation of dense PNIPAM microgel glass samples were discussed in chapter 2. Theory of experimental techniques (DLS and 3D dynamic light scattering techniques, UV-Vis spectroscopy, rheology) used for probing the PNIPAM microgel suspensions is described in chapter 2. Towards the studies on lyotropic chromonic liquid crystals, 32 wt% SSY solution is prepared in aqueous medium. Nematic phase is confirmed for the SSY LC sample at room temperature using polarizing optical microscope. Theory of rheo-microscopy technique used for the characterization of SSY LC sample is discussed in chapter 2.

In chapter 3, the light scattering studies and rheological characteristics of dense HC-PNIPAM and CS-PNIPAM glass samples are investigated using 3D-DLS and rheometer respectively, are reported. The short time dynamics observed for HC-PNIPAM and CS-PNIPAM samples were different. HC-PNIPAM sample showed diffusive dynamics (α = 1) whereas, CS-PNIPAM sample showed sub-diffusive dynamics (α < 1) at short time. This is the first observation reported on PNIPAM microgel glass that, morphological difference leads to different particle dynamics. The sub-diffusive dynamics exhibited by CS-PNIPAM glass is interpreted in light of entanglements of dangling polymer chains. However, dangling polymer chains and entanglements are absent in HC-PNIPAM glass hence it showed diffusive

dynamics. Apart from the dynamics, the role of entanglements on the yielding behavior is also discussed in chapter 3.

LAOS measurements on dense HC-PNIPAM microgel glasses showed single step yielding by exhibiting a single peak in loss modulus, G'', whereas, two-step yielding (two peaks in G'') was observed in dense CS-PNIPAM microgel glasses. The two-step yielding of CS-PNIPAM microgel glass shows similarity with that of attractive glass (AG). We understood that the attractive interaction in the case of AG mimic by the dangling chains entanglements in the case of CS-PNIPAM glass. Hence, the two-step yielding in CS-PNIPAM microgel glasses is attributed to: i) disentanglement of the dangling polymer chains giving a first peak in G'' at lower strain and ii) rupturing of nearest neighbor cages giving a second peak in G'' at large stain. Upon increasing the temperature, the colloidal glass (G' > G'') of CS-PNIPAM is observed to melt in to colloidal liquid (G'' > G'). The yielding beyond shear induced glass transition temperature is observed to be single step. The change of yielding from two-step at low temperature to single step at higher temperature is understood to be due to the disentanglement of the dangling polymer chains between the shells of neighboring PNIPAM microgel particles. Though two-step yielding has been reported in dense core-shell PNIPAM glasses, our observations provide the unambiguous evidence for the role of entanglements on the dynamics and yielding in soft repulsive PNIPAM glasses. Further, the energy associated with the yielding has been determined by analysing the stress-strain lissajous figures.

In Chapter 4 of the thesis, results on the flow and dynamics on the nematic phase of SSY liquid crystal are presented. The flow curve determined for a fixed temperature showed non-monotonic behavior with increasing shear rate. We observed a near-plateau regime at intermediate shear rates which is surrounded by two Newtonian regimes at lower and higher shear rates. Though there are reports of near plateau regime in surfactant based worm-like

micellar systems, our experiments provided the first observation of the existence of a near plateau regime in lyotropic chromonic liquid crystals. The flow curve is explained using *insitu* rheo-microscopy images taken during the shear flow. We observed subtle visual differences in various rheo-microscopic images taken at different flow regimes. This difference is explained in light of shear induced director orientation at different flow regimes. In the first Newtonian regime the director is orientated along the vorticity direction and in the second Newtonian regime the director is predominantly aligned along the flow direction and in the plateau regime, it is highly distorted with plenty of disclination defects.

We observed periodic stress oscillations in the near plateau regime. These are believed to be driven by the applied shear force. Though similar stress oscillations have been reported in the worm-like micellar system and recently in twist-bend nematic liquid crystals, our observations constitute the first evidence of stress oscillations in a lyotropic chromonic LC. Considering the similarities between micellar systems and studied chromonic systems (both are lyotropic nematics), we conjecture that the flow-order coupling effects are responsible for the mechanical instability and the resulting stress dynamics in the near plateau regime.

5.2 Key findings of the thesis

- Glass transition temperature was identified for HC-PNIPAM and CS-PNIPAM glass samples from the frequency sweep measurements by systematically varying temperature for a small fixed deformation ($\gamma_0 = 10\%$).
- 2 LAOS studies on dense PNIPAM microgel glasses have shown that the glassy state formed from dense suspensions of homogeneous core (HC) PNIPAM particles yield in a single step by exhibiting a single peak in G". Whereas, dense suspensions of core-shell (CS) PNIPAM particles yield in two steps by exhibiting two peaks in G". The yielding behavior of HC-PNIPAM glass and CS-PNIPAM glass are quite similar to that reported in the case

- of HS glass and attractive glass respectively. Thus, dangling polymer chains that existing in the surface of CS-PNIPAM spheres under dense conditions mimic the role of attractive interaction in attractive colloidal glasses.
- 3 Single step yielding observed in dense HC-PNIPAM microgel glass is attributed to the breaking of topological cages formed by neighboring particles. Whereas, two-step yielding of dense CS-PNIPAM microgel glass is attributed to i) breaking of entanglements of dangling polymer chains between neighboring particles and ii) rupturing of topological cages formed by neighboring particles.
- 4 SSY LC at the nematic phase is observed to show non-monotonic flow curves (stress (σ)strain rate ($\dot{\gamma}$) curves) by exhibiting three flow regimes upon varying the shear rates.
- 5 Shear induced director changes have been reported in SSY LC in the nematic phase, which is similar to those observed in the case of DSCG LC.
- 6 Dynamic stress fluctuations are reported in the near-plateau region of SSY LC for the first time.
- 7 Dynamic stress fluctuations are similar to those observed in worm-like micellar systems and very recently in twist-bend nematic liquid crystals.

5.3 Scope for the future work

- 1. Investigation of phase behavior of binary mixture of PNIPAM microgel suspensions using confocal microscopy.
- 2. Studying the glass transition in binary mixture of dense PNIPAM microgel suspensions.
- 3. Investigation of colloidal alloy structure in binary PNIPAM suspensions under dense conditions.
- 4. Studying the shear response of PNIPAM added lyotropic liquid crystals.
- 5. Determining the shear induced flow behavior of mixture of DSCG and SSY liquid crystals.

Publications related to thesis

- 1. Large amplitude oscillatory shear studies on dense PNIPAM microgel colloidal glasses
 - M. V. Saisavadas, Surajit Dhara, R. G. Joshi, and B. V. R. Tata
 - J. Colloid and Polym Sci., 301(6), 599 (2023)

DOI: 10.1007/s00396-023-05096-z

- Rheological studies on homogeneous and inhomogeneous core dense colloidal PNIPAM microgels
 - M. V. Saisavadas, R. G. Joshi, M. P. Kumar, S. Dhara, and B. V. R. Tata AIP Conference Proceedings, 2269, 060001 (2020)

DOI:10.1063/5.0019582

- 3. Shear-induced flow and dynamics of the nematic phase of Sunset Yellow lyotropic chromonic liquid crystal
 - M.V. Saisavadas, M. P. Kumar, B.V.R. Tata, and Surajit Dhara (Submitted to J. Liquid crystal)

Workshops/Conferences attended

- Presented a poster entitled "Rheology of Lyotropic Chromonic Liquid Crystals (LCLCs)" in the conference Frontiers in Physics (FIP-23), University of Hyderabad, India, March 3-4, 2023 and received Best poster Award.
- Presented a poster entitled "Rheology of Lyotropic Chromonic Liquid Crystals (LCLCs)" in the conference International Conference on Frontier Areas of Science and Technology (ICFAST-2022), 12th India-Japan Science and Technology Conclave, Hyderabad, India, September 09-10, 2022.
- 3. Delivered an **oral talk** on the topic "Large Amplitude Oscillatory Shear behaviour of Homogeneous and Core Shell Dense Colloidal PNIPAM Microgels", Virtual conference

- on Soft Matter (eCoSoM-2020), Sathyabama Institute of Science and Technology, July 15-17, 2020.
- 4. Presented a **poster** entitled "Rheological studies on homogeneous and inhomogeneous core dense colloidal PNIPAM microgels", International Conference on Multifunctional Materials (ICMM-2019), Hyderabad, India, December 19-21, 2019.
- 5. Attended a conference "STATPHYS-XI" (ONLINE), IISER Kolkata, March 21-25, 2022.
- 6. Attended one-day workshop on "Short Course on Applied Rheology" conducted by Anton Paar at Osmania University, Hyderabad on 5 February, 2019.
- 7. Attended "Soft and Active matter" workshop conducted by School of Physics, University of Hyderabad on 11-17 February, 2018.

Plagiarism-free statement

Microgel Suspensions and Lyotropic Liquid Crystals" submitted by Mr. Saisavadas M V (Reg. No. 17PHPH24) has been screened by the Turnitin software at the Indira Gandhi Memorial Library of the University of Hyderabad. The software shows a 22% similarity index out of which 12% came from the candidate's own two research articles related to this thesis, which are already published and available online. From the detailed similarity index report, it is obvious that the remaining 10% of the similarity index is due to the resemblance caused by the frequent use of the well-known standard terms such as Poly(N-isopropylacrylamide), PNIPAM microgel suspensions, solid phase, liquid phase, glassy state, polymer chains, synthesis, core-shell, cross linking, structural ordering, soft sphere, hard sphere, polymer density, interaction potential, relaxation, cages, peaks, yielding, Xray diffraction, scattering, polarizing optical microscopy, nematic phase, Sunset Yellow. The use of such terms is rampant in the literature and hence it is not surprising that the similarity index is artificially inflated. It should be noted that the use of such standard terms cannot be avoided.

Prof. Surajit Dhara

Co-supervisor

School of Physics

University of Hyderabad

Dr. Surajit Dhara
Professor
School of Physics
University of Hyderabad
Hyderabad-500 046, INDIA.

Date: 2-11-2023

Rheological Behaviour of Dense Thermo-responsive Microgel Suspensions and Lyotropic Liquid Crystals

by Saisavadas M V

Submission date: 01-Nov-2023 04:17PM (UTC+0530)

Submission ID: 2214062589

File name: Saisavadas_M_V.pdf (5.33M)

Word count: 27409 Character count: 151613

Rheological Behaviour of Dense Thermo-responsive Microgel Suspensions and Lyotropic Liquid Crystals

ORIGINA	ALITY REPORT				•
2 SIMILA	2% ARITY INDEX	8% INTERNET SOURCES	20% PUBLICATIONS	1% STUDENT PA	PERS
PRIMAR	Y SOURCES				
1	V. R. Tata studies o	isavadas, Suraji a. "Large amplit on dense PNIPA , Colloid and Po	cude oscillator M microgel co	y shear olloidal e, 2023 or. surajit Dr Professor	ics
2	www.hb			School of Phys University of Hyde Hyderabad-500 046	srabad 5, IND 3%
3	smartec Internet Source	h.gatech.edu			1 %
4	dynamic thermo-	hi, B. V. R. Tata s and two-step responsive mic mer Science, 2	yielding in de rogel glasses"	nse	1%
5	Kula, Su twist-be	een Kumar, Jaku rajit Dhara. "Dy nd nematic liqu Materials, 2021	namics of a sl	neared	<1%

6	M. V. Saisavadas, B. V. R. Tata, R. G. Joshi, M. Praveen Kumar, Surajit Dhara. "Rheological studies on homogeneous and inhomogeneous core dense colloidal PNIPAM microgels", AIP Publishing, 2020	<1%
7	arxiv.org Internet Source	<1%
8	fdocuments.in Internet Source	<1%
9	pure.uva.nl Internet Source	<1%
10	www.kent.edu Internet Source	<1%
11	Badri Vishal, Pallab Ghosh. "Nonlinear viscoelastic behavior of aqueous foam under large amplitude oscillatory shear flow", Korea-Australia Rheology Journal, 2018	<1%
12	Mathieu Destribats, Mayalen Eyharts, Véronique Lapeyre, Elisabeth Sellier, Imre Varga, Valérie Ravaine, Véronique Schmitt. "Impact of pNIPAM Microgel Size on Its Ability To Stabilize Pickering Emulsions", Langmuir, 2014	<1%

13	Janne-Mieke Meijer. "Colloidal Crystals of Spheres and Cubes in Real and Reciprocal Space", Springer Nature, 2015 Publication	<1%
14	www.researchgate.net Internet Source	<1%
15	Marco Hildebrandt, Sergey Lazarev, Javier Pérez, Ivan A. Vartanyants, Janne-Mieke Meijer, Matthias Karg. "SAXS Investigation of Core-Shell Microgels with High Scattering Contrast Cores: Access to Structure Factor and Volume Fraction", Macromolecules, 2022 Publication	<1%
16	D. Karthickeyan, R. G. Joshi, B. V. R. Tata. "FCC-HCP coexistence in dense thermo- responsive microgel crystals", The Journal of Chemical Physics, 2017	<1%
17	www.osti.gov Internet Source	<1%
18	Shuang Zhou. "Lyotropic Chromonic Liquid Crystals", Springer Science and Business Media LLC, 2017 Publication	<1%
19	Kiran Kaithakkal Jathavedan, Fayis Kanheerampockil, Suresh Bhat. "Role of particle morphology in the yielding behavior	< 1 %

of dense thermosensitive microgel suspensions", Journal of Applied Polymer Science, 2019 Publication

20	"Microgel Suspensions", Wiley, 2011	<1%
21	iopscience.iop.org Internet Source	<1%
22	M. Friederike Schulte, Andrea Scotti, Monia Brugnoni, Steffen Bochenek, Ahmed Mourran, Walter Richtering. "Tuning the Structure and Properties of Ultra-Low Cross- Linked Temperature-Sensitive Microgels at Interfaces via the Adsorption Pathway", Langmuir, 2019	<1%
23	M. Anandha Rao. "Rheology of Fluid, Semisolid, and Solid Foods", Springer Science and Business Media LLC, 2014	<1%
24	Leela Joshi, Shin-Woong Kang, Dena Mae Agra-Kooijman, Satyendra Kumar. " Concentration, temperature, and dependence of sunset-yellow aggregates in aqueous solutions: An x-ray investigation ", Physical Review E, 2009 Publication	< 1 %



"Organization of Microgels at the Air–Water Interface under Compression: Role of Electrostatics and Cross-Linking Density", Langmuir, 2017

Publication

E. B. Sirota. "Complete phase diagram of a charged colloidal system: A synchro- tron x-ray scattering study", Physical Review Letters, 03/1989

Publication

Herzhaft Benjamin. "Influence of Temperature and Clays/Emulsion Microstructure on Oil-Based Mud Low Shear Rate Rheology", Proceedings of SPE Annual Technical Conference and Exhibition ATCE, 09/2002

Publication

Jonghee Eun, Jiyong Cheon, Sung-Jo Kim, Tae Joo Shin, Joonwoo Jeong. "Lyotropic Chromonic Liquid Crystals and Their Impurities Reveal the Importance of the Position of Functional Groups in Self-Assembly", The Journal of Physical Chemistry B, 2020

Publication

Submitted to Korea Advanced Institute of Science and Technology

Student Paper

<1%

<1%

<1%

<1%

36	Min Feng, Xiang Kong, Yange Feng, Xiaojuan Li, Ning Luo, Liqiang Zhang, Changhe Du, Daoai Wang. "A New Reversible Thermosensitive Liquid–Solid TENG Based on a P(NIPAM-MMA) Copolymer for Triboelectricity Regulation and Temperature Monitoring", Small, 2022 Publication	<1%
37	Sunilkumar Khandavalli, Jonathan P. Rothstein. "Large amplitude oscillatory shear rheology of three different shear-thickening particle dispersions", Rheologica Acta, 2015 Publication	<1%
38	etd.ohiolink.edu Internet Source	<1%
39	link.springer.com Internet Source	<1%
40	Ying Li, Linbing Wang. "Computer-aided procedure for determination of asphalt content in asphalt mixture using discrete element method", International Journal of Pavement Engineering, 2015	<1%
41	ialimentoslem1.files.wordpress.com Internet Source	<1%
42	Barbara J. Frisken. "Revisiting the Method of Cumulants for the Analysis of Dynamic Light-	<1%

Scattering Data", Applied Optics, 2001 Publication

43	dspace.ncl.res.in:8080 Internet Source	<1%
44	B.V.R. Tata, P.S. Mohanty, J. Yamanaka, T. Kawakami. "Dynamic Light Scattering Studies in Silica/Ethylene Glycol Charged Colloidal System", Molecular Simulation, 2006	<1%
45	Jukka P. Jokisaari, Geoffrey R. Luckhurst, Bakir A. Timimi, Jianfeng Zhu, Herbert Zimmermann. "Twist-bend nematic phase of the liquid crystal dimer CB7CB: orientational order and conical angle determined by Xe and H NMR spectroscopy ", Liquid Crystals, 2015	<1%
46	www.barc.gov.in Internet Source	<1%
47	Gareth H. Mckinley. "Self-similar spiral instabilities in elastic flows between a cone and a plate", Journal of Fluid Mechanics, 02/1995 Publication	<1%
48	Submitted to Indian School of Mines Student Paper	<1%
49	Gerhard Nägele. "Tracer-diffusion in colloidal mixtures: A mode-coupling scheme with	<1%

hydrodynamic interactions", The Journal of Chemical Physics, 1998 Publication

Exclude quotes

On

Exclude matches

< 14 words

Exclude bibliography On